DEPLOYABLE SPACE TELESCOPE:

Optimal Boom Design for High Precision Deployment of the Secondary Mirror

MSc Thesis

J.W. Lopes Barreto

Faculty of Aerospace Engineering

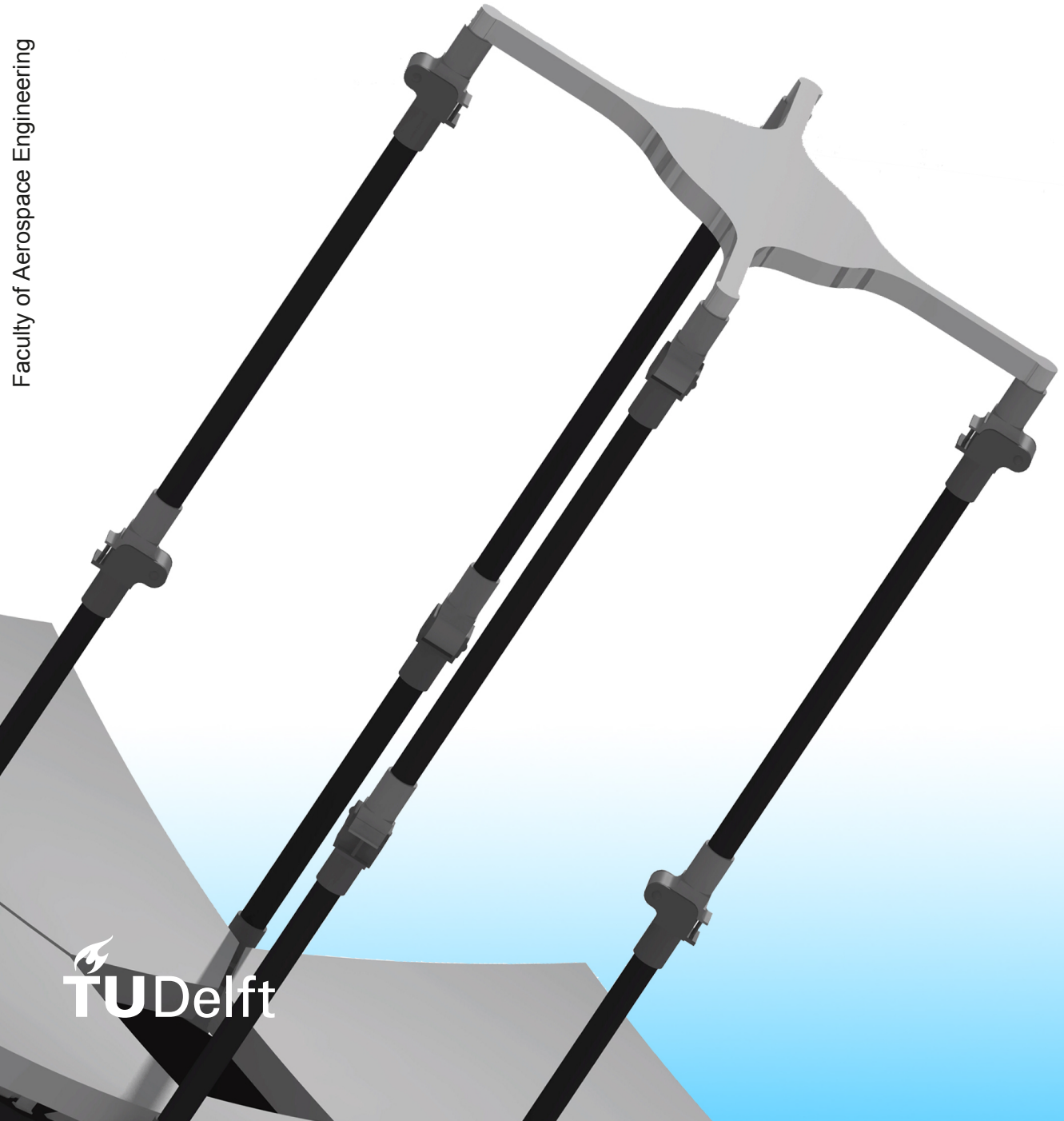

TU Delft

Deployable Space Telescope:
Optimal Boom Design for High Precision Deployment of the Secondary Mirror

MSc Thesis

by

J.W. Lopes Barreto

to obtain the degree of Master of Science
at the Delft University of Technology,
to be defended publicly on Friday May 19, 2017 at 1:00 PM.

Date:	May 12, 2017	
Student number:	4162595	
Thesis committee:	prof. dr. E.K.A. Gill,	TU Delft, SSE
	dr. ir. J.M. Kuiper,	TU Delft, SSE
	ir. D. Dolkens,	TU Delft, SSE
	dr. D.M. Stam,	TU Delft, AS
	ir. H. Cruijssen,	Airbus Defence & Space

TU Delft

Summary

The use of deployable structures for space telescopes has the advantage of enabling options to improve their performance and reducing the launch volume. The Deployable Space Telescope (DST), which is currently developed by the Space Systems Engineering (SSE) department of the Faculty of Aerospace Engineering at Delft University of Technology, will make use of a high precision deployable structure to extend the secondary mirror 1.3 m from the primary mirror. In the initial design of the telescope, three articulated booms were chosen to extend the secondary mirror from the primary mirror. The benefit of such a deployable structure is that it can achieve a high positioning accuracy and provide the required post-deployment stability. Nevertheless, the Invar articulated booms had a high mass and a low deployment ratio. In order to reduce the mass and increase the deployment ratio of the mechanism, while maintaining the required deployment accuracy, this thesis has focused on investigating alternative deployable structures and materials, including mechanical and thermal performances.

Common deployable structures used in space, were divided into six main types: articulated booms, coilable booms, shape memory composite (SMC) booms, telescopic booms, inflatable booms, and deployable truss structures. From a preliminary trade-off it could be concluded that for this specific mission, the best options were the articulated boom and the coilable tubular mast (CTM), which is a type of SMC booms. Next to the technology trade-off, a material trade-off was performed, including materials as stainless steel, titanium, aluminum, Invar and carbon fiber reinforced polymers (CFRP). This trade-off showed that CFRP would be the best main material for both types of booms.

To compare these booms with each other, both booms were designed for a downscaled version of the DST, which is designed for a demonstration mission, that only requires a single boom as the deployment mechanism for the secondary optical element. This was chosen, as the loads acting on the boom in the downscaled version could be considered as the worst-case scenario, compared to the full design. Both booms were designed according to a demanding alignment budget, in order to meet the optical performance of the DST. The designed articulated boom consisted of three segments, a root hinge, and two hinges in the middle. This resulted in a total mass of 2.46 kg, including a contingency factor. Furthermore, the articulated boom had a deployment ratio of 2.7, with a stowage volume of 6111 cm^3. The CTM boom, was expected to have less mass than the articulated boom, however the designed HDRM took up about 60% of the total mass of the system, leading to a total mass of the CTM boom mechanism of 3.33 kg. The CTM boom itself was found to be 145 g. However, the CTM boom did have a higher deployment ratio of 4.2 and a smaller stowage volume of 5425 cm^3.

The FEM software ANSYS was used to perform static, harmonic, modal, and thermal analyses on both of the boom designs. Both booms have shown to have sub-micrometer deflections due to (quasi-)static micro-gravity conditions. However, if the booms vibrated at their natural frequency, the deflection limits of 10 µm and 15 µm, depending on the axis, were surpassed. Therefore, it must be ensured that no vibrations in the DST system are present at the same frequency as the natural frequencies of the boom. The thermal analyses have shown that the thermal effects are critical on both booms. The deflection limits along multiple axes were exceeded, calculated over one orbital period. To solve the thermal issue, it was proposed to use a baffle around the telescope, to apply aluminum coating on the booms, or to readjust the materials used. This have shown to have significant positive impact on the calculated deflections.

Using the boom properties, mechanical properties, thermal properties, and the risks of both boom designs, a final trade-off was made. From this trade-off, it could be concluded that the articulated boom was the optimal deployable structure for the extension of the secondary mirror of the DST project. This designed articulated boom, however, has a significant improvement in terms of mass with respect to the initial designed articulated boom. With this result, the research was concluded with a proposal for the integration of the articulated boom design with the full DST system design and the downscaled design.

Preface

Before you lies the thesis "Deployable Space Telescope: Optimal Boom Design for High Precision Deployment of Secondary Mirror", which forms the backbone of the deployment mechanism of the secondary mirror for the Deployable Space Telescope (DST) project. This project is performed by the Space Systems Engineering (SSE) department of the Faculty of Aerospace Engineering at the Delft University of Technology in cooperation with Airbus Defence & Space Netherlands.

This research has been challenging, yet highly rewarding. I have gained much knowledge on mechanisms, materials, and astrophysics missions in general. Getting the opportunity to work with a company as Airbus Defence & Space, was an informative and interesting experience. This experience taught me all the practical difficulties a design can encounter, when it is designed for a real space mission.

I would like to thank my supervisors Hans Kuiper and Dennis Dolkens for their excellent guidance and support during this process. I also wish to thank Henk Cruijssen and Guus Borst, from Airbus Defence & Space, for the very useful feedback and their extensive knowledge on deployable mechanisms. Furthermore, I would like to thank my colleagues of the DST team, Boris van Putten and Matthew Corvers, for being such great support and inspiration.

Finally, I would like to give a special thanks to my parents, sister, and girlfriend for supporting me, and keeping me motivated. Helga deserves a particular note of thanks: your motivational, kind, and wise words have, as always, served me well.

It has been a great journey; the journey of becoming a Master of Science in Aerospace Engineering. The most beautiful and most challenging five and a half years of my life, so far. This journey would not have been possible without the support of my family, friends, colleagues, and professors. Thank you all for being a part of this.

Enjoy your reading.

Jessy Lopes Barreto

's-Gravendeel, May 12, 2017

Contents

List of Figures

List of Tables

List of Symbols

Latin Alphabet

a	Deflection	[m]
A	Area	[m^2]
d	Diameter	[m]
E	Young's modulus	[m^2]
f	Frequency	[Hz]
F	Force	[N]
FF	Form factor	[-]
g	Gravitational acceleration	[m/s^2]
G	Shear modulus	[Pa]
h	Height	[m]
I	Moment of inertia	[m^4]
J	Torsional constant	[m^4]
k or K	Constant	[-]
l or L	Length	[m]
m	mass	[kg]
n	Number of coils	[-]
p	Pressure	[Pa]
P	Load	[N]
P_e	Critical buckling load	[N]
q	Distributed load	[N/m]
q	Heat flux	[W/m^2]
r	Radius	[m]
t	Thickness	[m]
w	Width	[m]

Greek Alphabet

α	Absorbtivity	[-]
α	Albedo	[-]
α_T	Coefficient of thermal expansion	[K^{-1}]
β	Flange thickness factor	[-]
β	Solar beta angle	[°]
δ	Deflection	[m]
ε	Strain	[-]
θ	Angle	[rad] or [°]
ν	Poisson's ratio	[-]
ξ	Solar zenith angle	[°]
ρ	Density	[kg/m^3]
σ	Stress	[Pa]
φ	Deflection angle	[rad] or [°]

List of Abbreviations

AAReST	Autonomous Assembly of a Reconfigurable Space Telescope
ADAM	Able Deployable Articulated Mast
ADS	Airbus Defence & Space Netherlands
AOCS	Attitude and Orbit Control System
AU	Astronomical Unit
BEP	Break Even Point
CFRP	Carbon Fiber Reinforced Plastic / Polymer
CSG	Centre Spatial Guyanais
CTE	Coefficient of Thermal Expansion
CTM	Collapsible Tube Mast
DST	Deployable Space Telescope
FAST	Folding Articulated Square Truss
FEM	Finite Element Method
GSD	Ground Sampling Distance
HDRM	Hold-Down Release Mechanism
ITAR	International Traffic in Arms Regulations
IXO	International X-ray Observatory
JWST	James Webb Space Telescope
M1	Mirror 1 of DST
M2	Mirror 2 of DST
M3	Mirror 3 of DST
MS	Multispectral
NuSTAR	Nuclear Spectroscopic Telescope Array
OEB	Optical Elements Box
PAN	Panchromatic
PRISM	Pico-satellite for Remote-sensing and Innovative Space Missions
SMC	Shape Memory Composite
SNR	Signal-to-Noise Ratio
SPS	Stackable Platform Structure
SRTM	Shuttle Radar Topographic Mission
STEM	Storable Tubular Extensible Member
TRL	Technology Readiness Level
WBS	Work Breakdown Structure

Introduction 1

The space industry is evolving fast and technology advancement makes the number of space applications even larger [1]. Whereas performance is an important factor in spacecraft design, the demand for these new space applications will also bring complications with the major constraint in spacecraft design: the dimensions of the launcher's fairing. These dimensions determine the volume of the spacecraft. Regarding astrophysics missions, this directly constraints the size of the telescope, which eventually will limit the performance of the mission [2]. In order to resolve this problem, deployable structures are used for various space applications, such as space telescopes, so that the mission requirements can still be met while keeping the stowed volume within the size of the launcher's fairing.

1.1 Background

The main problem with current space telescopes is that the space between the optical elements is principally empty. As mentioned, this space is used to achieve the required focal length. Nevertheless, this is only important once the space telescope is in operation, so the space is useless during the launch phase. If it is decided to use a deployable structure between the optical elements, this can save up to 70% of the payload volume and about 50% of the payload mass, compared to the current (non-deployable) space telescopes [3].

Furthermore, current high resolution Earth observation satellites tend to be very large and heavy, which results in high development and launch costs. The satellites also have a long revisit time and are limited available. By using a smaller telescope which can be used in micro-satellite platforms, these current drawbacks can be resolved. Dolkens started the DST project as a Master's graduation project at the Delft University of Technology in 2014, together with Dr. ir. Kuiper. The objective was to design a deployable, low mass telescope, using synthetic aperture technology to reach the same resolution as the high resolution Earth observation satellites, although with a much smaller launch volume. The instrument has an ground sampling distance (GSD) of 25 cm from an orbital altitude of 500 km, which is the same resolution as of current state-of-the-art Earth observation satellites GeoEye-2 and Worldview-3, at the same orbital altitude. To give an impression, GeoEye-2 and Worldview-3 have a mass of 2087 kg and 2800 kg, respectively, while the DST aims for a maximum mass of 50 kg, with a threshold of 100 kg for the instrument [4].

Figure 1.1 Initial design of the DST [5]

The DST project is still in the design phase. The telescope can be seen in Figure 1.1, where the deployment sequence is also shown. In short, it consists of three main mirrors, a detector and the main housing. The primary mirror was first designed to consist of three deployable articulated booms, as shown in the figure, however in a later stage of the design phase this amount was changed to four. In the initial design, the secondary mirror was positioned at 1.7 m from the primary mirror with the use of three deployable

arms. Nevertheless, this length and amount of deployable arms are considered as variables, which will be investigated and determined during this research project. The deployable arms, as shown in Figure 1.1, are based on the deployable arms of the International X-ray Observatory (IXO) mission. In chapter 3 more information of this space telescope is provided. However, the deployable arms of the IXO telescope are about 12 m at deployed state and have a positioning accuracy of 1 mm [6]. While the primary (M1) and secondary mirror (M2) are located on the outside of the main housing, the third mirror (M3) is mounted in the main housing.

As it is unrealistic to design all aspects of the telescope in a single Master's graduation project, Dolkens covered the optical and conceptual mechanical design of the instrument, the image processing techniques, and the calibration strategy. As there was no in-depth research performed on the deployable mechanism of the secondary mirror, this research project will continue with that work.

1.2 Research Questions and Objectives

The initial designed articulated booms, were made out of Invar and had a high mass. Next to the mass, the deployment ratio was relatively low, which has negative impact on the stowage volume. In order to investigate possibilities to reduce the mass and increase the deployment ratio of the mechanism, while maintaining the required deployment accuracy, the research objective of this thesis has been formulated as:

> *"The research objective is to investigate what type of deployable structure is most suitable for the extension of the secondary mirror of the DST project, in terms of positioning accuracy, mass, and deployment ratio, by analyzing the structural and deployment performances of multiple deployable structures."*

From the objective the main research question is derived as:

> *"What is the optimal deployable structure for the extension of the secondary mirror of the DST project, in terms of positioning accuracy, mass, and deployment ratio and how can this be integrated in the system design?"*

Throughout this report, the answer to this research question will be found.

1.3 Thesis Outline

This thesis is divided into five main parts. Before the start of the first part, the chapter '*Project Outline*' will elaborate on the research project, including a description of the demonstration mission of the DST project and the derived requirements for both the full design and the design for the demonstration mission. The first part '*Research*' provides background information on existing deployable structures for space applications, followed by a preliminary trade-off for the selection of two deployable structures. Furthermore, a trade-off for the material selection for the deployable structures can be found. The second part of this report '*Design Process*' starts off with the fundamentals for the boom designs, followed by the design process of an articulated boom and a CTM boom. In Part III '*Analysis, Results & Comparison*', the analyses of both boom designs are presented. First the methodologies of the analyses are described. At the end of this part, a detailed comparison is made between both boom designs, and a final trade-off is performed. Using the result of the final trade-off, a proposal is made for the integration of the boom with the system design in the fourth part '*Project Integration*'. Furthermore, an overview is given of the integration of the boom design and the downscaled version of the DTS for the demonstration mission. The fifth part '*Conclusions & Recommendations*' concludes the report and gives recommendations for future research and design of the deployable structure for the DST project. In the final part '*Bibliography & Appendices*' the bibliography and appendices can be found.

Project Outline

2

This chapter provides an overview of the research project for the deployable mechanism of the secondary mirror, including the demonstration mission, in which the concept will be validated. Next, the initial requirements of the DST project and the demonstration mission are discussed. Furthermore, the work breakdown structure (WBS) of the research project presented. Finally, the research implications are elaborated.

2.1 Demonstration Mission

In order to validate the concept of the DST, a demonstration mission is proposed in collaboration with Airbus Defence & Space Netherlands (ADS), which is planned to be launched around 2019. An agreement was made that TU Delft will provide the space telescope and ADS will provide the launch possibility on their Stackable Platform Structure (SPS). In this section a short introduction to the SPS structure is given and the impact of this demonstration mission on the design is discussed. Note that this information is considered as confidential and may not be published.

2.1.1 SPS

The SPS is as a ring structure between the payload and the launch vehicle [7]. It carries the primary payload on top and the secondary payloads on the sides. The amount of secondary payloads is dependent on which version of SPS is used. The SPS-2 module provides room from four micro-satellites with a mass from 10 to 100 kg. This module can be seen in Figure 2.1. As the DST instrument is based on a micro-satellite platform, the SPS-2 is chosen as the most suitable SPS version.

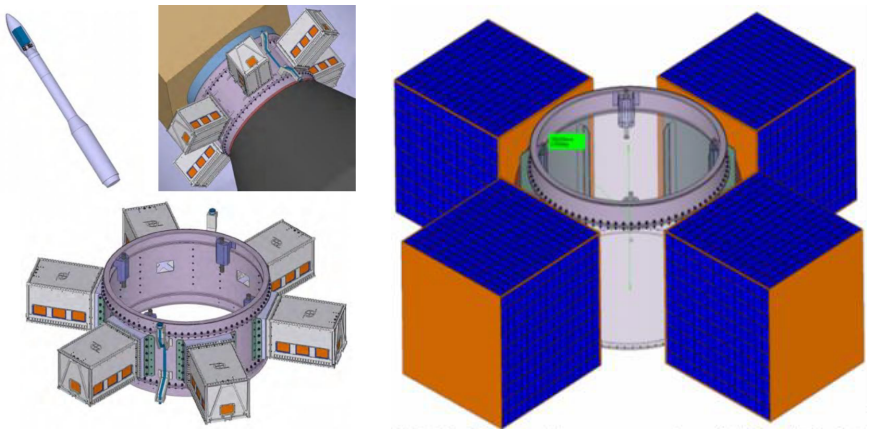

(a) Integration of SPS-2 ring on Vega launcher

(b) SPS-2 ring

Figure 2.1 SPS-2 module for micro-satellites [7]

The height of the ring can be varied from 60 cm to 100 cm. To keep the mass as low as possible, it is preferred to use the smallest ring height, thus 60 cm. This height is a crucial input requirement, as this will directly influence the maximum stowage height, which has impact on the design of the deployable structure. The effects on the design will be discussed in the next subsection.

2.1.2 Impact on Design

The SPS provides room for the DST instrument, however due to volume constraints a downscaled version of the DST is required. This downscaled version needs to be a representative of the full design, so it can validate the key design features of the telescope. The four segments of the primary mirror of the full design will not fit on the ring, since the one side of the available space is used as a connection between the ring and the instrument (see Figure 2.1). Therefore, trade-offs have been made and it was determined that only a single mirror segment was enough to provide the required optical performance for validation. Also the deployment mechanism for this mirror can be validated with this concept. An artistic impression of this concept including the ring can be seen in Figure 2.2. Note that this is not the final design yet. More information on the deployment mechanism of the primary mirror can be found in Boris van Putten's Master's thesis [8], whom was responsible for this mechanism.

Due to this downscaled version of the primary mirror, the need of an actual secondary mirror is withdrawn. In stead of using a secondary mirror, an optical elements box (OEB) is used, including a deformable mirror. In Figure 2.3 the optical architecture of this OEB is shown.

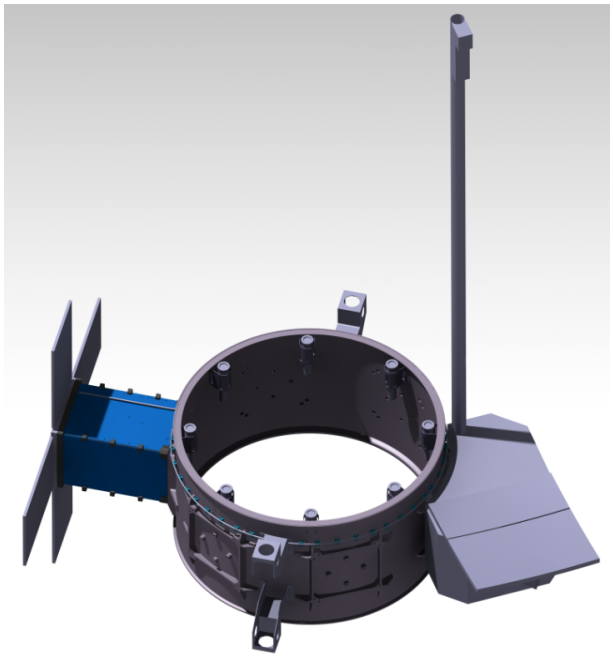

Figure 2.2 DST downscaled concept on SPS-2 module (image credits: B. van Putten)

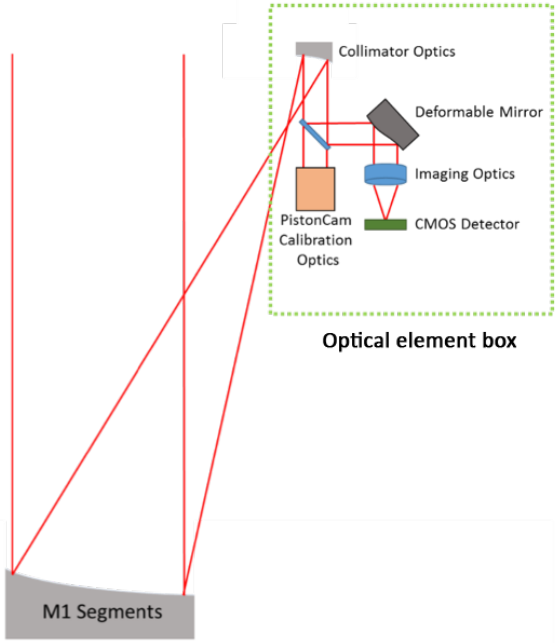

Figure 2.3 Optical architecture of the downscaled version (image credits: D. Dolkens)

To minimize the volume, it is determined that only a single arm is required to deploy the OEB. This arm requires a high deployment ratio. The deployment ratio of any deployable structure is the deployed length divided by the stowed length [9]. Based on the initial deployment length of 1.7 m and a ring height of 60 cm, the deployment ratio calculated to be about 2.8. This means that the deployed length requires to be almost three times higher than the stowed height. This will have impact on the type of deployable structures that can be used. In a later stage of this report, these technologies will be discussed including the maximum achievable deployment ratio. In Table 2.1, the main differences between the downscaled and the full version are shown. In this report, both designs will be covered.

2.2 Design Requirements

Defining proper design requirements, is an important process for this research project. These requirements set the goals and constraints of the mechanism and all further decisions made in this report are based on these requirements. Even though there will be two versions of the deployable mechanism, there

Table 2.1 Full design vs downscaled design

Parameter	Full design	Downscaled design
Mirrors	3	2
Primary mirror segments	4	1
No. deployable arms	4	1
Minimum deployment ratio	2	2.8
Secondary mirror	Yes	No
OEB	No	Yes
Satellite bus	Micro-sat	SPS-2

are still overall requirements which are applicable to both designs. The main part of this section is based on the requirements of the full design. Requirements which are based on the downscaled version are briefly elaborated.

2.2.1 Notation of Requirements

In the following subsections, codes will be used to label the individual requirements. In this report a requirement code is set up in the following way: *R-M2D-CAT-#.* Where *R* stands for requirement, *M2D* stands for the deployable mechanism of M2, *CAT* is the category of the requirement and should consist of three letters, and # indicates the number of the requirement. As there is also a downscaled version, these requirements will have a slightly different notation: *R-M2D-DS-CAT-#.*

2.2.2 General Requirements

The main objective of the deployable mechanism is to support and extend the secondary mirror with a certain distance from the primary mirror. At this point this distance still to be determined, however the final value will be provided in chapter 11. From these objectives, two requirements can be set up: *R-M2D-GEN-1* and *R-M2D-GEN-2*. Next to these requirements, the original goal of the DST project was to have a maximum mass of 50 kg. Nevertheless, in the initial design of Dolkens, the total mass was found to be 74.8 kg, of which 14.3 kg came from the folding arm structure. This subsystem had the second highest mass of the total system. Therefore a requirement has to be made that the mass of the new design shall be lower than the 14.3 kg. This requirement is stated in *R-M2D-GEN-3*. The deployment ratio of the mechanism can be categorized as a general requirement as well. As was already discussed in this chapter, the deployment ratio for the full design and downscaled design have to be minimal 2 and 2.8, respectively. From these values, the requirements for the deployment ratio are formulated. Furthermore important general requirements are that the mechanism cannot use International Traffic in Arms Regulations (ITAR) related components and must be in accordance with the Centre Spatial Guyanais (CSG) safety regulations. In Table 2.2 all general requirements are listed.

2.2.3 Structural Requirements

Before the structural requirements can be set up, the optical requirements of the secondary mirror should be explored first, as the structural requirements are derived from the optical requirements. The optical alignment tolerances, as provided by Dolkens, are stated in Table 2.3. Note that these values are different from the original design, as the optical design of the telescope has been optimized [4]. The initial tolerances were about one third lower than the current design, which make the realization of this instrument currently more feasible.

These tolerances can be classified into tilt, decenter and despace (see Figure 2.4). Tilt is defined as the

Table 2.2 General requirements

Code	Requirement
R-M2D-GEN-1	The mechanism shall extend M2 <TBD> m from M1.
R-M2D-GEN-2	The mechanism shall provide structural support for M2.
R-M2D-GEN-3	The total mass of the mechanism shall be lower than 14 kg.
R-M2D-GEN-4	The mechanism shall have a minimum deployment ratio of 2.
R-M2D-GEN-5	The mechanism shall not contain ITAR related components.
R-M2D-GEN-6	The mechanism shall comply with the CSG safety regulations.

Table 2.3 Alignment tolerances of the three mirrors of the deployable telescope

Element	Position [µm]			Tilt [µrad]			Radius [%]
	X	*Y*	*Z*	*X*	*Y*	*Z*	
Primary Mirror Segments	2	2	2	2	4	50	0.001
Secondary Mirror	15	15	10	100	100	100	0.001
Tertiary Mirror	4	4	4	10	10	50	0.001

orientation of the secondary mirror with respect to the axis of primary mirror. Tilt can be present around the x, y, and z-axis, as shown in Figure 2.4a. Decenter is the offset of the secondary mirror with respect to the primary mirror's central axis in x and y direction. Despace is the offset in distance between the secondary and primary mirror and is measured along the z-axis [9]. These alignment errors introduce aberrations in the optical system and therefore the deployable mechanism need to keep the secondary mirror within these tolerances. Referring back to Table 2.3, one can conclude that the tolerances of the DST secondary mirror are: a decenter of 15 µm in both directions, a despace of 10 µm, a tilt of 100 µrad about all axes.

These tolerances can directly be translated to the structural requirements. The decenter and despace can be considered as deflections, while the tilt can be considered as twist angles.

Moreover, the vibrations from internal and external sources of the satellite will have influence on the positioning accuracy of the secondary mirror. If the deployed mechanism will have a natural frequency close to the frequencies of these vibrations, the mechanism will start to resonate. The amplitude keeps increasing, with the risk of exceeding the optical requirements and damaging the mechanism itself. Based on input of ADS, the lower limit of the natural frequency of the deployed mechanism is set to 5 Hz. To prevent unwanted interference with the attitude and orbit control system (AOCS), the natural frequencies of the subsystems need to be spread over the frequency domain. The first natural frequencies of solar arrays are normally within the boundaries of 0.1 Hz to 0.5 Hz. For example, if vibrations are transmitted, 5 Hz is a factor 10 away from the 0.5 Hz of a solar array. Therefore, no resonant rise will not take place. It is important that the control frequency of the AOCS loop control is outside 0.5 Hz and out of 5 Hz, for example 2 Hz would be suitable. However, higher modes will have to be checked, but that is a concern for the design of the AOCS. In Table 2.4 the structural requirements are listed.

2.2.4 Launch Requirements

The final set of requirements needed for this research project, are the launch requirements. These launch requirements are based on loads acting on the mechanism during launch. In stowed configuration, the mechanism should withstand the vibrational loads during the launch. During this phase, the gravitational acceleration can go up to 4.5 times the standard gravitational acceleration. A typical longitudinal

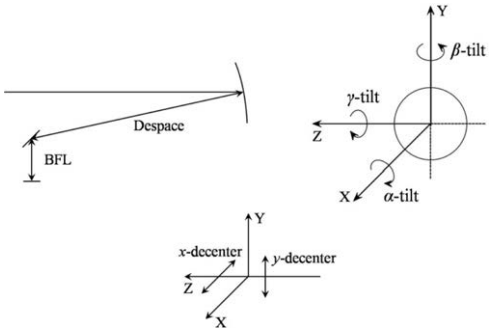

(a) Offsets and angles of optical misalignment [10]

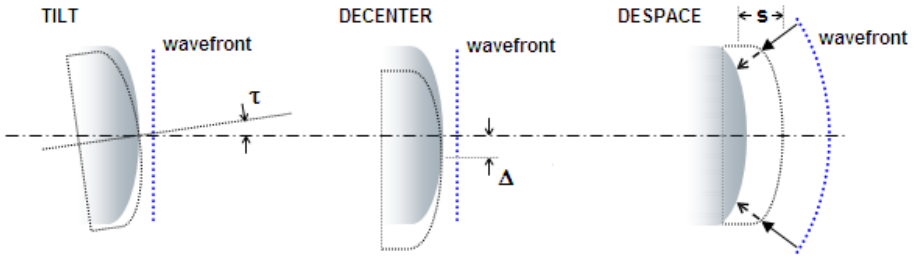

(b) Misalignment of optical surfaces [11]

Figure 2.4 Tilt, decenter, and despace

Table 2.4 Structural requirements

Code	Requirement
R-M2D-STR-1	The deployed mechanism shall have a maximum deflection of 15 µm in the *x* and *y*-direction, measured from the root.
R-M2D-STR-2	The deployed mechanism shall have a maximum deflection of 10 µm in the *z*-direction, measured from the root.
R-M2D-STR-3	The deployed mechanism shall have a maximum twist of 100 µrad about all axes, measured from the root.
R-M2D-STR-4	The deployed mechanism shall have a minimum natural frequency of 5 Hz

acceleration graph for an Ariane 5 can be seen in Figure 2.5.

The most possible launchers for the DST are the Ariane 5 and the Vega rockets. For the demonstration mission it is already determined that the Vega launcher will be used. The design of the SPS is also based on the Vega launcher. The maximum load factor in longitudinal direction is 4.55 g for the Ariane 5 launcher and 7.0 g for the Vega launcher. In lateral direction, this is 0.25 g and 0.9 g, respectively [13, 14]. In Table 2.5 the sine-equivalent vibrations are listed per frequency band for both launchers. For frequencies higher than 100 Hz, it can be observed that the sine amplitudes are the lowest.

Next to the maximum load factors and the sine-equivalent vibrations, the mechanism should withstand the shock loads which could go from 20 g up to 1000 g for the Ariane 5 and up to 2000 g for the Vega launcher. For the expected natural frequency of the mechanism, this shock load will be maximum 30 g. Based on the shock loads and Table 2.5, two requirements can be derived. These requirements can be found in Table 2.6.

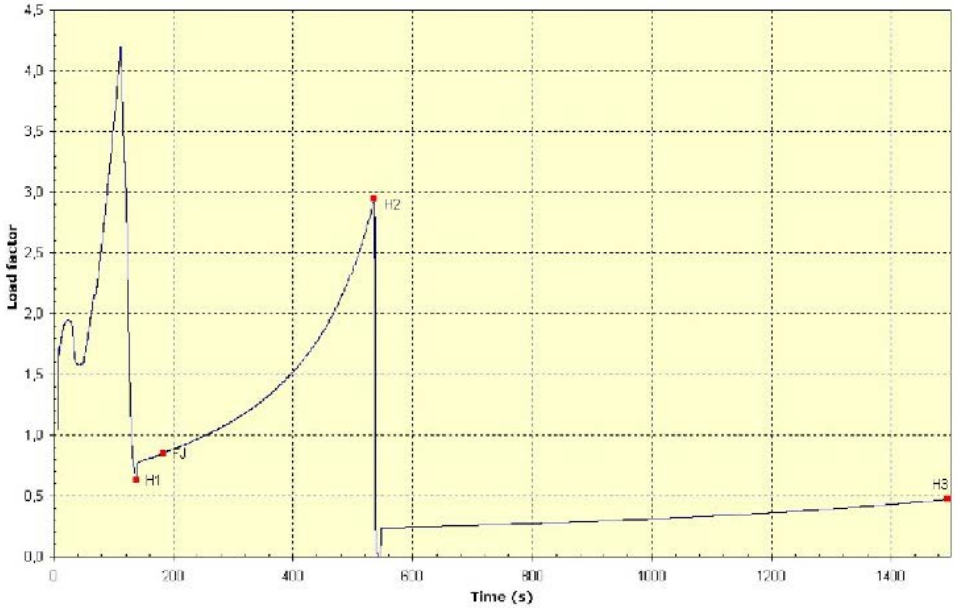

Figure 2.5 Typical longitudinal acceleration during launch with Ariane 5 [12]

Table 2.5 Sine-equivalent vibrations for Ariane 5 and Vega rockets [13, 14]

Launcher	Frequency band [Hz]	Sine amplitude [g]	
		Longitudinal	Lateral
Ariane 5	2 – 25	1.0	0.8
	25 – 50	1.0	0.6
	50 – 100	0.8	0.6
Vega	1 – 5	0.4	0.4
	5 – 45	0.8	0.5
	45 – 110	1.0	0.5
	110 – 125	0.2	0.2

Table 2.6 Launch requirements

Code	Requirement
R-M2D-LAU-1	The stowed mechanism shall be able to withstand accelerations up to 30 g.
R-M2D-LAU-2	The stowed mechanism shall have a minimum natural frequency of 100 Hz.

2.2.5 Overview of Requirements

In this section, multiple requirements are derived. In Table 2.7 an overview is presented of all initial requirements for the full scale design of DST.

2.2.6 Downscaled Requirements

As the demonstration mission is a representation of the original mission, the requirements need to be more or less identical to the requirements of the full design, with slight adjustments in some requirements. One important general requirement which is determined for the downscaled design, and not determined for the full design yet, is the launch time frame. The demonstration mission is set to launch within two years

Table 2.7 List of requirements for full design

Code	Requirement
R-M2D-GEN-1	The mechanism shall extend M2 <TBD> m from M1.
R-M2D-GEN-2	The mechanism shall provide structural support for M2.
R-M2D-GEN-3	The total mass of the mechanism shall be lower than 14 kg.
R-M2D-GEN-4	The mechanism shall have a minimum deployment ratio of 2.
R-M2D-GEN-5	The mechanism shall not contain ITAR related components.
R-M2D-GEN-6	The mechanism shall comply with the CSG safety regulations.
R-M2D-STR-1	The deployed mechanism shall have a maximum deflection of 15 µm in the x and y-direction, measured from the root.
R-M2D-STR-2	The deployed mechanism shall have a maximum deflection of 10 µm in the z-direction, measured from the root.
R-M2D-STR-3	The deployed mechanism shall have a maximum twist of 100 µrad about all axes, measured from the root.
R-M2D-STR-4	The deployed mechanism shall have a minimum natural frequency of 5 Hz
R-M2D-LAU-1	The stowed mechanism shall be able to withstand accelerations up to 30 g.
R-M2D-LAU-2	The stowed mechanism shall have a minimum natural frequency of 100 Hz.

from now. Therefore the mechanism shall be completed within these two years. The general requirements for the mass and deployment ratio have been adjusted to the values of the downscaled model. The rest of the requirements of the full design are still valid for the downscaled design. The requirements for the downscaled design can be seen in Table 2.8.

2.3 Work Breakdown Structure

In order to meet the objective and answer the research question, the work of the research project is broken down into six main work packages. These work packages can be seen in the WBS shown in Figure 2.6. The description of each work package can be found below.

1.1 Project Management
During this phase, the project proposal is written. Furthermore a WBS is made in parallel with the project planning. All the work will be delivered to the supervisor for approval.

1.2 System Requirements
From this point the thesis project starts. From the initial design of the DST, the requirements are derived and a list of all these requirements is made. The requirements are broken up into the requirements for the full design and requirements for the downscaled design.

1.3 Technology Selection
From all the information from the literature study, a preliminary trade-off will be made in order to choose two deployable mechanisms for further concept generation. Next to the trade-off of deployable mechanisms, the a trade-off for the material needs to be performed as well.

1.4 Concepts Design
In this phase the two concepts will further researched, followed by the detailed design of the mechanism. This will consist of the design of the booms and the design of the hold-down release mechanism (HDRM). Parallel to this process the design will be verified, and adjustments are made once a requirement is not fulfilled. An important delivery of this work package are the CAD drawings

Table 2.8 List of requirements for downscaled design

Code	Requirement
R-M2D-DS-GEN-1	The downscaled mechanism shall extend the OEB <TBD> m from M1.
R-M2D-DS-GEN-2	The downscaled mechanism shall provide structural support for the OEB.
R-M2D-DS-GEN-3	The total mass of the downscaled mechanism shall be lower than 4 kg.
R-M2D-DS-GEN-4	The downscaled mechanism shall have a minimum deployment ratio of 2.8.
R-M2D-DS-GEN-5	The downscaled mechanism shall be completed before 2019.
R-M2D-DS-GEN-6	The downscaled mechanism shall not contain ITAR related components.
R-M2D-DS-GEN-6	The downscaled mechanism shall comply with the CSG safety regulations.
R-M2D-DS-STR-1	The deployed downscaled mechanism shall have a maximum deflection of 15 µm in the x and y-direction, measured from the root.
R-M2D-DS-STR-2	The deployed downscaled mechanism shall have a maximum deflection of 10 µm in the z-direction , measured from the root.
R-M2D-DS-STR-3	The deployed downscaled mechanism shall have a maximum twist of 100 µrad about all axes, measured from the root.
R-M2D-DS-STR-4	The deployed downscaled mechanism shall have a minimum natural frequency of 5 Hz
R-M2D-DS-LAU-1	The stowed downscaled mechanism shall be able to withstand accelerations up to 30 g.
R-M2D-DS-LAU-2	The stowed downscaled mechanism shall have a minimum natural frequency of 100 Hz.

of the mechanisms.

1.5 Concepts Analysis
The concept analysis work package will include the analyses of both mechanisms. First one should familiarize with the finite element method (FEM) software called ANSYS. Once enough knowledge is gained, the analysis cases shall be defined and the analyses will be performed. Once all results are obtianed, a detailed comparison can be made of both mechanisms. Based on the conclusion retrieved from this comparison, the final concept can be chosen.

1.6 System Design Integration
The final work package is the system design integration. Up to this point the research has been stand-alone, however the results should be integrated in the DST design. The interface with the original mission, as well as with the demonstration mission, need to be made. Finally, a risk analysis is required to complete the research.

2.4 Research Implications

Current high accuracy deployable structures tend to be relatively heavy, while ultra-lightweight deployable structures do not have the amount of stiffness to provide a high positioning accuracy. Balancing these parameters will be one of the most challenging parts of the process.

Moreover, this research is only theoretical and no experiments will be conducted. Therefore, the results in this research can only be validated by comparing analytical results with FEM results. Also, in depth research of a single deployable mechanism is not possible, as multiple mechanisms shall be investigated and designed. The design will be performed until a certain depth, from which an analysis can be performed. More on this can be found in chapter 14.

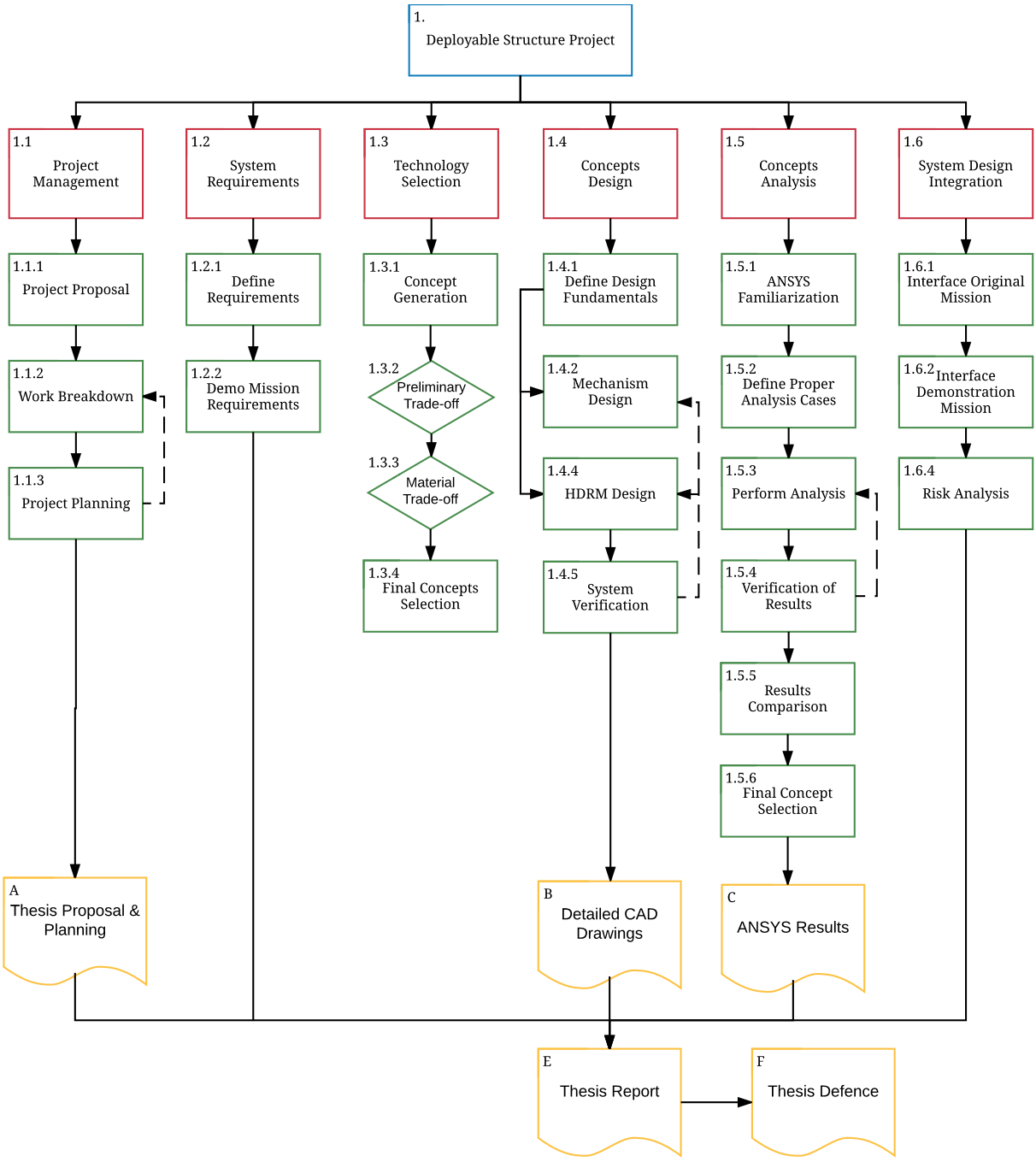

Figure 2.6 WBS of the Master's thesis project

Nevertheless, the main challenge of this research project is to come up with a design, using non-complex deployment technologies, to achieve a positioning accuracy in the order of micrometers for the secondary mirror, while keeping the mass as low as possible.

I

Research

Literature Review 3

The use of deployable structures in space has been done since the launch of the very first satellite, Sputnik 1, in 1957 [15]. In the beginning of space flight, satellites were relatively small compared to now, because they were limited by the capacity of the launchers. Although, the size of spacecraft kept increasing over time, but not at the same rate as the increasing size of the capacity of launchers. Therefore a significant amount of research has been performed in the field of deployable structures in the past decades [16]. The deployable structures used in space flight can be distinguished in three main types: solar panels, antennas, and booms and masts.

Whereas solar panels and antennas can be considered as bi-dimensional deployable structures, booms and masts are so-called uni-dimensional deployable structures [17]. Booms and masts are used for multiple space applications. The two most common applications are the separation of electronic instruments from the spacecraft to reduce the interference with the rest of the spacecraft, such as magnetometers, and for supporting other structures of a spacecraft [16].

This chapter will elaborate on the different types of deployable booms and masts, and an overview of the different booms and masts types is provided, containing the advantages and disadvantages of each specific type.[1]

3.1 Deployable Booms and Masts

Deployable booms have evolved over the years. In the beginning of space flight deployable booms and masts were mass efficient, however they were mechanically complex. Currently, there is a trend in research for advanced materials that can be used to make deployable booms which are both light and mechanically simple [18]. Deployable booms can be distinguished in six main types [2, 19]: articulated booms, coilable booms, shape memory composite (SMC) booms, telescopic booms, inflatable booms, and deployable truss structures (masts). In this section these types are further discussed.

3.1.1 Articulated Booms

Articulated booms, also called folding booms, are the most common boom type that is used for deployable space telescope designs. They are composed of multiple boom segments, which are interconnected by hinges or joints. In this way the total boom can fold into the stowed configuration, as shown in Figure 3.1. There are multiple ways of folding articulated booms, such as the accordion principle, the Z-fold, or just folding the boom along the body of spacecraft.

The advantage of this boom type is that it can result in a very compact configuration and it can be a very simplistic design. Although, this depends on what type of hinges or joints are used [19]. There are rigid and flexible hinges. When rigid hinges or joints are used, more complexity and mass are added to the system and a careful material selection should be performed to ensure thermal stability. Flexible hinges, as tape spring hinges or composite tube hinges, are very light-weight, so the risk of adding more mass is already reduced, however flexibility can conflict with the stability of the structure.

Articulated booms are already space proven, however not yet for astrophysics missions. The first astrophysics mission in which articulated booms will be space proven is the Autonomous Assembly of a Reconfigurable Space Telescope (AAReST), which was set for launch in 2016 [20], however has not been launched yet, followed by the James Webb Space Telescope (JWST) in 2018 [21].

[1] This literature review was already partially published by the author in the AE4010 Research Methodologies course.

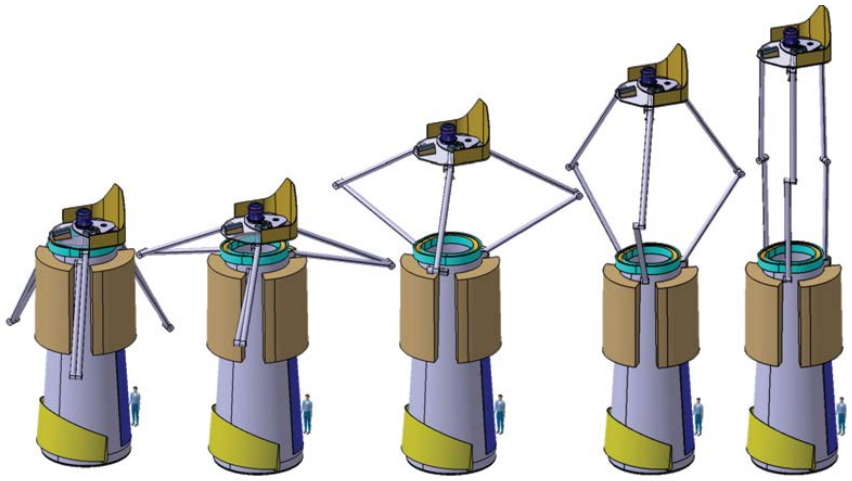

Figure 3.1 Deployment sequence of IXO's articulated arms [22]

3.1.2 Coilable Booms

In stead of only using flexible hinges, it is also possible to use complete flexible booms. If these booms are wound or coiled along a central core, these booms are called coilable booms [2, 19]. Strain-energy is stored during the stowed configuration and uses this energy to deploy after release. Due to the rotational motion which is needed to release the booms, an electric motor is often used as the deployment actuator. These booms are normally made of elastic materials.

As coilable booms can be coiled or wound, coilable booms are very compact, resulting in a high deployment ratio. To give an impression, the stored length can be even less than 2% of the deployed length. Next to its compactness, coilable booms tend to be very lightweight and do not require much power for deployment.

Unfortunately, coilable booms have big disadvantages regarding the positioning accuracy. Due to its flexibility, it is less stiff and rigid. This can cause large oscillations of the boom during the deployment phase, which can damage the booms itself and if a collision between the spacecraft's body and the boo occurs, this can be fatal for the mission. Coilable booms are also often sensitive to thermal distortions.

In contrast to articulated booms, coilable booms have been space proven for a space telescope, namely for the Pico-satellite for Remote-sensing and Innovative Space Missions (PRISM), which was successfully launched by the H-IIA rocket. Once placed in orbit, the boom was successfully deployed [23]. The coilable boom of the PRISM space telescope can be seen in Figure 3.2.

3.1.3 SMC Booms

Another boom type which is very closely related to coilable booms are SMC booms [19]. SMC booms are flattened and then can be coiled or folded. Same as coilable booms, SMC booms do not use hinges, as the boom is flexible. These booms have the same advantages as coilable booms: very compact, lightweight, and it requires low power for deployment. An advantage SMC booms have over coilable booms is that SMC booms are typically made of CFRP, which means that they have a very low CTE, meaning that SMC booms are not really sensitive to thermal distortions. The principle of SMC booms already exist for about 50 years [25]. Nevertheless, they have never been space proven for astrophysics applications. In general coiled SMC booms are flexible shells. They are flattened and coiled around a central core. The three common flexible shell concepts used in the space industry are the storable tubular extensible member (STEM), the bi-STEM and the collapsible tube mast (CTM) [26].

The STEM boom (Figure 3.3a) has the same working principle as a tape measure, however due to the angle of 50° or more it will overlap to form a circular cross section, as can be seen in Figure 3.3a. Once

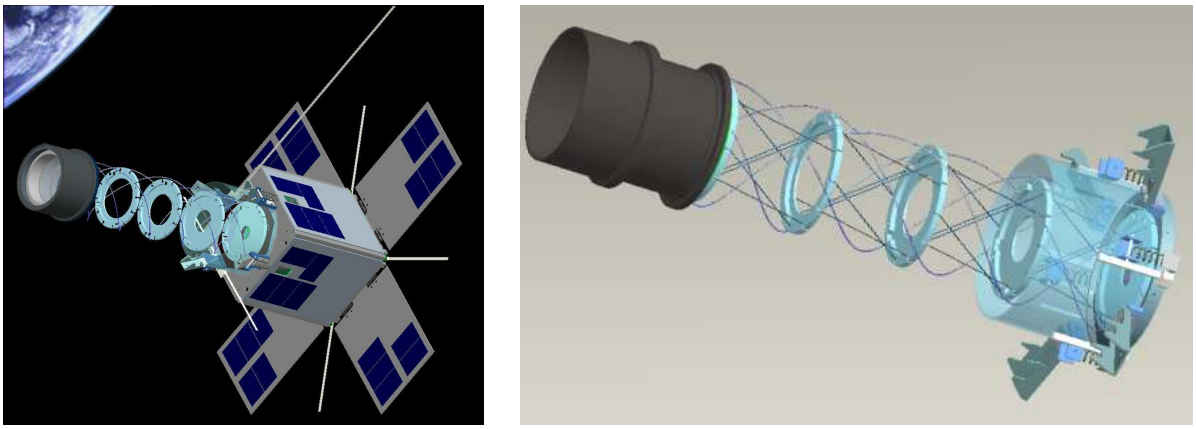

(a) Impression of the complete PRISM satellite

(b) The coilable boom of the PRISM

Figure 3.2 The PRISM satellite [24]

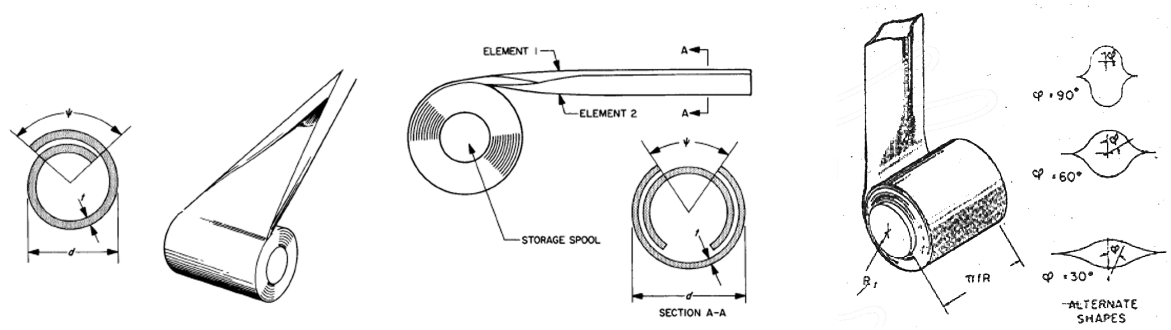

(a) The STEM principle [25]

(b) The bi-STEM principle [25]

(c) The CTM principle [26]

Figure 3.3 Flexible shell principles

the deployed it forms into a rigid member. A variation on the STEM is the bi-STEM, which can be seen in Figure 3.3b. It consist of two STEMs of which one overlaps the other one. The advantage of bi-STEM over STEM is that the rolled-up width is smaller and it is structural more stable, due to the symmetric construction [26]. Moreover, the bending and torsional stiffness of the bi-STEM is a bit higher, compared to STEM. The last flexible shell structure is the CTM (Figure 3.3c). The CTM consist of two preformed tapes, which are bonded together to form a closed cross-section. This close cross-section causes the CTM to have a much higher torsional stiffness than conventional STEM booms. This is also the main advantage of CTM booms over STEM booms. Nevertheless, this also cause the CTM booms to be more difficult to manufacture than STEM booms. Currently they are mainly used as support structures for solar sails.

Nevertheless, the stiffness is still not very high and is not suitable to deploy heavy structures. This means that an individual SMC boom could not be really useful for astrophysics missions. If it would be combined as a complete structure, as was done for PRISM, it could become suitable for an astrophysics mission. Although, single SMC booms are very suitable for solar sails or solar shields, as they do not require a high positioning accuracy.

3.1.4 Telescopic Booms

Telescopic booms are a completely different category of deployable booms [2, 19]. These booms are not folded or rolled up, but consist of segmented hollow tubes that fit into each other. Each segment has a smaller diameter than the previous segment. In stowed configuration they are all stowed in each other, while in deployed state the segments extend from each other and the length of the boom is formed by the

total length of the different segments combined. Due to this principle, telescopic booms are stiffer than the other deployable boom types and they provide good dynamic response. Moreover, telescopic booms are more stable and precise. However, telescopic booms tend to be much heavier than other boom types, are more mechanically complex, and are not very suitable for large extension capabilities. Therefore they cannot compete with the specific mass or deployment ratio with the other boom types, but they can compete when a shorter extension length with high stiffness is required [17].

Telescopic booms have been developed for multiple space space applications, however in the literature only two telescopic booms were found to be flight qualified and one of them also space proven [27, 28]. In Figure 3.4 a recently developed telescopic boom can be seen. The AstroTube is developed by Oxford Space Systems and has shown promising capabilities for future missions, in terms of mass, deployment ratio and deployment accuracy.

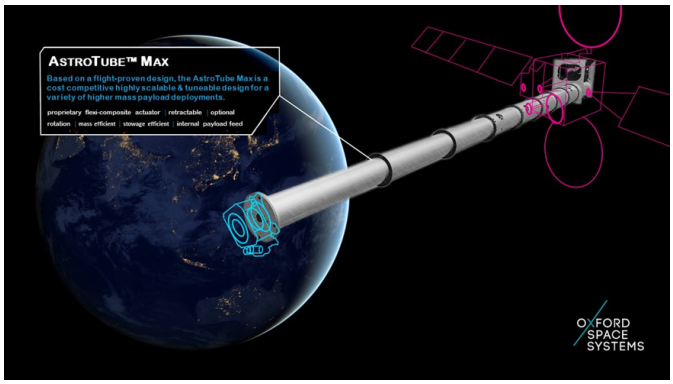

Figure 3.4 Oxford Space Systems AstroTube telescopic boom [29]

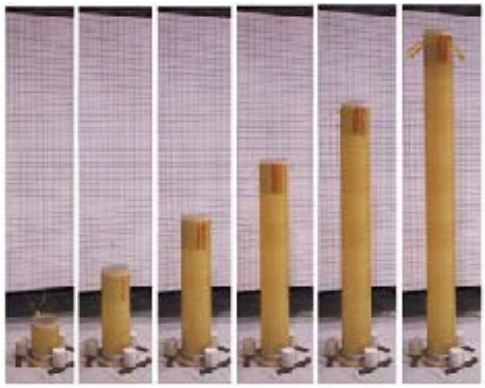

Figure 3.5 Impression of an inflatable boom [30]

3.1.5 Inflatable Booms

Whilst articulated booms, coilable booms, SMC booms, and telescopic booms are widely used for space applications, inflatable booms are not so commonly used. Even though the idea of using inflatable structures is dated back to the 60s, the TRL of inflatable booms has remained low. This could be due to the fact that the risks might outweigh the benefits of using inflatable structures. Nonetheless, inflatable booms do have major advantages. Due to the fact that the booms only consist of a skin and the internal pressurized air, these booms are extremely lightweight. Moreover, the deployment ratio of inflatable booms can go up to 45 [2]. Post-deployment rigidization is an important aspect for inflatable booms, as one wants the boom to keep its stiffness. However, this stiffness is very low and would not be suitable for carrying any type of payload which is more than 10 kg [2]. This is one of the reasons that inflatable booms have never been used for astrophysics missions. An impression of an inflatable can be seen in Figure 3.5.

3.1.6 Deployable Truss Structures

Multiple deployable masts have been used in the history of space flight [2]. Still, most of these masts are based on two masts which were designed and built in the previous century: the Folding Articulated Square Truss (FAST) Mast and the Able Deployable Articulated Mast (ADAM). Both these masts are developed by the AEC-Able Engineering Company [17].

The FASTMast (Figure 3.6) was developed in 1987, to serve as a deployment mechanism for the solar arrays of the ISS. In total eight of these masts were used to support the solar arrays [16, 26]. The FASTMast has a total deployed length of 34.75 m and a stowed (cannister) length of 2.3 m, which means that the deployment ratio of the FASTMast is about 15. This is an impressive deployment ratio for such a structure. Other benefits of this structure are that it has a high strength and has a long lifetime. The mast consists of aluminium struts and stainless steel wire ropes [31].

(a) Impression of ADAM [32] **(b)** Impression of the FASTMast [26]

Figure 3.6 Deployable Truss Structures

Twelve years after the development of the FASTMast, AEC-Able Engineering Company again developed a deployable mast, but now intended for the Shuttle Radar Topographic Mission (SRTM) [31]. ADAM had to serve as a separation mechanism of two antennas. Therefore the design was intended to be stiff, with high positioning accuracy and post-deployment stability. The deployment length of ADAM is 60 m, with a stowed (cannister) length of 2.9 m, which means that the deployment ratio is about 21. The structure consist of spherical hinges, multiple battens (horizontal), longerons (vertical), and diagonal cross-braces. These longerons and battens are made of graphite epoxy, while the cables are made of titanium.

One of the first concepts made of the FASTMast was the CoilABLE mast [33]. The difference between the CoilABLE mast and the FASTMast is that, as the name already implies, the CoilABLE mast could be coiled around a central core. The deployment mechanism for coilable masts are the same as for coilable booms. This principle is shown in Figure 3.7, however note that this is not the CoilABLE mast, but another coilable mast developed by JPL.

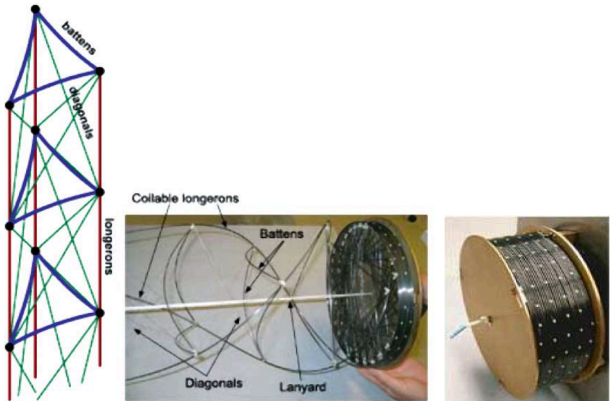

Figure 3.7 Principle of a coilable mast by JPL [34]

It can be passively deployed, such as using internal strain energy, or active deployed, using a motor. When passive deployment is chosen, only lengths less than 3 m are suitable. This is due to the fact that the stiffness during deployment is low and only full stiffness is gained after the deployment has completed. If an active deployment is chosen, a cannister will be used, such as for the FASTMast and ADAM, and longer deployment lengths can be achieved. A motor driven rotating nut is located in the cannister, which enables the mast to leave the cannister already containing its stiffness [16]. Nevertheless, using a cannister will also increase the storage volume and introduce more mass to the system.

Until now, only two astrophysics missions exist where deployable truss structures are used: the Nuclear

Spectroscopic Telescope Array (NuSTAR) and a conceptual design of the IXO, which already was introduced in this chapter.

3.2 Overview

Multiple deployable boom and mast technologies have been investigated and presented in this chapter. Each of these technologies have shown potential solutions to solve the challenge of designing the deployable structure for the secondary mirror of the DST project. In Table 3.1 a brief overview is given of all the deployable booms and masts, with their main advantages and disadvantages. These advantages and disadvantages will be used in the technology selection process, which can be found in the following chapter.

Table 3.1 Comparison of the booms and masts types

Boom/mast type	Advantages	Disadvantages
Articulated booms	High stability and positioning accuracy	Not compact
Coilable booms	Very compact, lightweight, and low power requirements	Low positioning accuracy and high CTE
SMC booms	Low CTE, very compact, and lightweight	Low TRL and low positioning accuracy
Telescopic booms	Very stable and high positioning accuracy	Mass, complexity, and small length
Inflatable booms	Extremely compact and lightweight	Low TRL and low positioning accuracy
Deployable truss structures	Flight heritage, stable, compact, and high positioning accuracy	Complexity and mass

Technology Selection 4

In the previous chapter, six different types of deployable booms and masts were discussed, including their advantages and disadvantages. This chapter will make a comparison between these different types of deployable booms and masts. Furthermore, a trade-off is made in order to choose the most suitable types for further design and analysis.

4.1 Comparison of Booms and Masts

The main purpose of this research is to investigate possibilities of replacing the originally designed articulated booms with a more compact and lightweight boom design, while maintaining the required positioning accuracy. Therefore a comparison will be made between the following crucial parameters: stiffness, which directly influences the positioning accuracy, deployment ratio, and mass.

Puig *et al.* have investigated these parameters as a function of deployable length and found multiple relations and have presented them in the article *A review on large deployable structures for astrophysics missions* [2]. These relations can be found in Figures 4.1 to 4.2. What has to be noted is that this article was published in 2010, and does not contain all the data of the recent developments, which are presented in this thesis. For this reason, the graphs might not completely agree with the findings of the previously presented literature review, but are still a very good approximation.

4.1.1 Stiffness

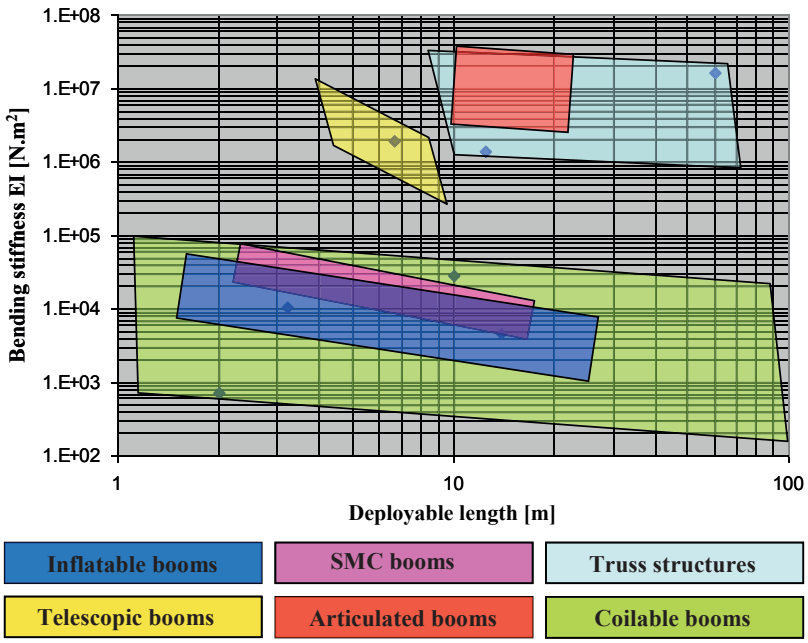

Figure 4.1 Relation between deployable length and bending stiffness [2]

From the literature review it became clear that articulated booms and deployable truss structures are the most used types of deployable structures for astrophysics missions. This is due to their high stiffness, which has positive influence on the achievable positioning accuracy. Comparing this observation to Figure 4.1, it can be concluded that the observation is indeed valid. Telescopic booms do have a high bending stiffness as well and can also be interesting for astrophysics missions. Nevertheless, telescopic

booms do have certain drawbacks regarding mass and packaging ratio. This will be discussed in the next subsections.

A type of articulated booms which is not included in Figure 4.1, is the composite tube boom, which is a flexible articulated boom. This type of boom was used for the AAReST, however its stiffness is much lower compared to the rigid articulated arms of the IXO space telescope. Therefore this region of articulated booms in Figure 4.1, should be shifted a bit more downwards.

As already assumed, coilable booms do provide the lowest bending stiffness. This is because coilable booms are mostly based on a wires which are held together by some structural elements that provide some extra stiffness to the structure. In other words, the stiffness of coilable booms is mostly based on the structural elements which keep the wire frame together. That is why the region for coilable booms is very large, as it is very dependent on this type of structural elements.

Finally, SMC booms and inflatable booms have moderate stiffness, compared to the other booms and masts. A lot of advancement has been made in the development of these types since 2010, so the region in the graph is not really reliable. Nevertheless, what can be confirmed from the graph is that SMC booms indeed provide more stiffness than current inflatable booms.

4.1.2 Deployment Ratio

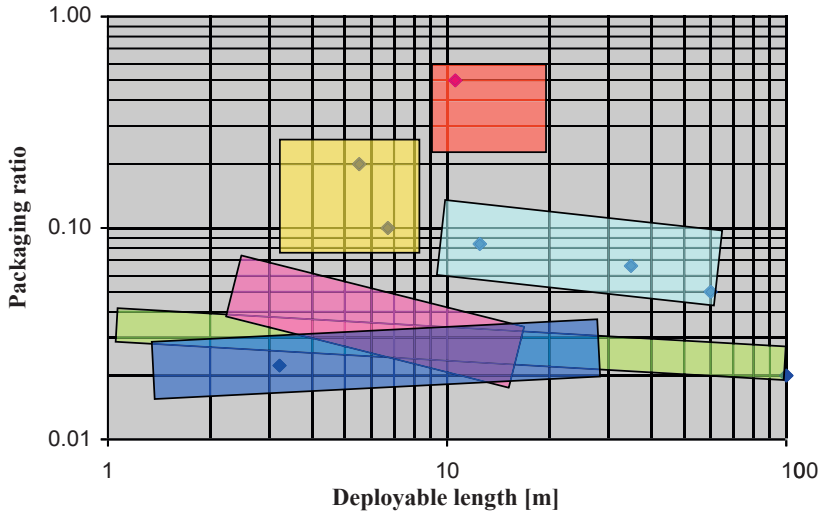

Figure 4.2 Relation between deployable length and deployment ratio [2]

Next to the stiffness, the deployment ratio plays an important role in designing a compact deployment mechanism. Note that Puig *et al.* have used an inverted form of the deployment ratio, which they call the packaging ratio, so the deployment ratios mentioned in this report are the inversion of the ones shown in Figure 4.2. So, the lower the deployment ratio is in the graph, the better.

Articulated booms have by far the worst packaging ratio. This ratio can be improved, but is rather prevented as more hinges are required to accomplish this. More hinges can introduce more deployment errors, which will reduce the overall stiffness of the structure, and increase the total mass of the system. Telescopic booms perform less worse, however these types of booms are constrained to the deployment length as this is the sum of all the lengths of the segments combined. Therefore there is a very strong relation between the deployment length and the stowed length, for these types of booms. In contrast to telescopic booms, truss structures are less sensitive to its deployment length. These masts can achieve very little stowage lengths compared to its deployment length. Most of the time the deployment ratio is more influenced by the size of the cannister, rather than the stowed length of the mast itself.

The highest packaging ratio was found during the literature review corresponded to inflatable booms. These types of booms can achieve such high ratios by applying special folding techniques, such as origami

folding. Eventually, in terms of deployment ratio, SMC booms and coilable booms act more or less the same as inflatable booms. They can achieve very high deployment lengths with a very little stowed length. They are really volume efficient types of deployable structures.

4.1.3 Mass

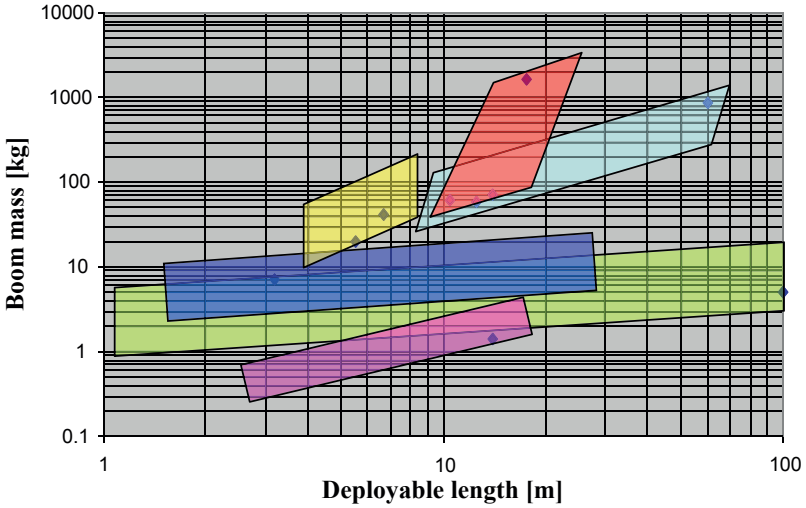

Figure 4.3 Relation between deployable length and boom mass [2]

The final important parameter is mass. Mass plays a crucial role as the DST project is based on a mission for a micro-satellite and should therefore not weigh more than 100 kg. In Figure 4.3 the relation between deployable length and boom mass is shown.

Whereas articulated booms, telescopic booms, and deployable truss structures were the best options in terms of stiffness (or positioning accuracy), in terms of mass they are the worst options. Here SMC booms, coilable booms, and inflatable booms do perform better. Especially when looking at CTM booms, these booms can be made ultra-lightweight, but still with an acceptable stiffness. Nevertheless, the author does not fully agree with Puig *et al.*, as inflatable booms can become very lightweight as well. It could be that Puig *et al.* included the pressure systems to the mass, however the region should not come so close to the mass of telescopic booms. An important observation is that the mass of the HDRM of each system is not included in the analysis by Puig *et al.*, which can have consequences on trade-offs based on this graph. More about the HDRM mass can be found in chapter 8.

Mass, however, is a parameter which can always be improved. There is an ongoing research on materials and how to increase their specific stiffness and specific strength.

4.2 Preliminary Trade-off

Using the knowledge gained from the comparison of the different deployable booms and masts, a preliminary trade-off can be performed, in order to choose the most suitable deployable boom or mast for further design and analysis. First the corresponding trade-off parameters are discussed, followed by the trade-off itself. Finally the results will be discussed.

4.2.1 Trade-off Parameters and Methodology

In the previous section, already a few important trade-off parameters were discussed: deployment accuracy (stiffness), mass, and deployment ratio. Nevertheless, for a good trade-off more trade-off parameters are needed. The trade-off parameters which were used to determine the potential deployable structures for the secondary mirror are:

1. Deployment accuracy (6)
2. Post-deployment stability (6)
3. Feasibility (6)
4. Deployment ratio (5)
5. TRL (4)
6. Mass (3)

These parameters are already ranked from most important to least important. Behind each parameter, the weight is indicated between brackets. As can be seen, deployment accuracy, post-deployment stability and feasibility are the most important parameters. The importance of deployment accuracy is already discussed in the previous section. Post-deployment stability is highly important as the positioning accuracy might be high, however if the structure becomes unstable after a certain time or due to dynamic disturbances, this will have major impact on the performance of the telescope. Feasibility is characterized as one of the most important trade-off parameters, as the boom has to be producible within the resource limits of a university project. The demonstration mission is set to be launched in 2019, so the TRL of the deployable structure used should not be too low, as verifying the technology requires lots of time.

Table 4.1 Trade-off table legend

Score	Description
0	Unacceptable
1	Acceptable deficiencies
2	Good, meets requirements
3	Excellent, exceeds requirements

Each mechanism is evaluated, based on these parameters and each parameter is rated with scores from 0 to 3. A color code is used for each score, in order to have a better graphical overview of the total score. The description of each score and their corresponding color code can be found in Table 4.1. Note that if the score is 0, which means *unacceptable*, the mechanism is directly eliminated and should therefor not be further explored. All the parameters of a certain mechanism should have a score of 1 or higher, in order to be chosen for a final design. After evaluating each parameter carefully for each specific mechanism, the final scores is calculated by the summation of all the .

Recalling from chapter 3, the deployable booms and masts and their subcategories used for this trade-off are:

1. Articulated booms
   (a) Rigid articulated booms (e.g. booms and separate hinges)
   (b) Flexible articulated booms (e.g. composite tube hinges)
2. Coilable booms
3. SMC booms
   (a) STEM and bi-STEM booms
   (b) CTM booms
4. Telescopic booms
5. Deployable truss structures
   (a) CoilABLE mast
   (b) FASTMast

(c) ADAM mast

In the following subsection, the results of the trade-off will be presented and discussed.

4.2.2 Result and Discussion

The results of the preliminary trade-off are shown in Figure 4.4.

Mechanism	Criteria / Weight (x/30)	Deployment Accuracy 6	Stability 6	Feasibilty 6	Deployment Ratio 5	TRL 4	Mass 3	Score Max. 3
Articulated Booms	Rigid	3	3	3	1	2	1	✓ 2.3
	Flexible	1	2	1	1	1	3	! 1.4
Coilable Booms		1	0	0	3	3	3	✗ 1.4
SMC Booms	(Bi-)STEM	2	0	2	3	1	3	✗ 1.7
	CTM	2	1	3	3	1	3	✓ 2.1
Telescopic Booms		3	3	1	2	1	1	✓ 2.0
Inflatable Booms		0	0	0	3	0	3	✗ 0.8
Deployable Truss Structures	CoilABLE	1	1	0	3	1	2	✗ 1.2
	FAST	3	3	0	2	3	1	✗ 2.0
	ADAM	3	3	0	2	3	1	✗ 2.0

Figure 4.4 Technology preliminary trade-off result

The results did quite meet the expectations. Most astrophysics missions choose to have articulated booms or deployable truss structures to extend a certain optical element. Comparing this to the scores of these mechanisms, it can be seen that they indeed have one of the highest scores. Even though deployable truss structures are too complex and too expensive to develop for a university project, they still have a score of 2.0 with a 0 as score for feasibility. If this score was changed to the maximum (3), the score would have been 2.6 for both the FASTMast and the ADAM concept. This also matches with the final concept of the IXO space telescope where the deployable truss structures concept was preferred over the articulated boom concept. Unfortunately, as already mentioned deployable truss structures are not feasible for this specific project.

Furthermore, telescopic booms and articulated booms have proven to be the most stiff mechanisms (see Figure 4.1), so can achieve the highest deployment accuracies. Therefore these mechanisms were expected to have one of the highest scores. Nevertheless, telescopic booms tend to be mechanically complex, therefore it is rated with a 1 for feasibility. Also the deployment ratio is not not excellent, which makes the telescopic boom have a lower score than the articulated boom.

The CTM boom, on the other hand, was quite a surprise to be in the top three. Such a boom is quite easy to manufacture, does not bring high costs, is very lightweight, and has a decent stability and deployment accuracy. However, the TRL of this boom for astrophysics missions is not that high. This project could be improving the TRL of this type of boom, if it is decided to use this as the final mechanism for the extension of the secondary mirror.

As was already discussed, coilable booms do not provide the required stability and stiffness which are required to achieve the alignment budget of the secondary mirror. The same holds for (bi-)STEM booms

and inflatable booms. Therefore, these mechanisms are eliminated. Also the complexity of the coilable booms do not make the mechanism feasible for the DST project. Inflatable booms are still in an premature phase, and cannot be used for this project.

4.2.3 Final Decision

The results of the trade-off have shown that the three best options for the extension mechanism of the secondary mirror would be the articulated boom, the CTM boom, and the telescopic boom.

During the trade-off phase, there was no knowledge about the costs of developing these types of mechanisms. After consulting senior engineers at Airbus Defence & Space, it became clear that the development of a telescopic boom would bring too high costs and, more important, possible alignment errors in each segment could cause too large overall alignment errors in the mechanism. This was based on the experience of previous Airbus Defence & Space projects. Using this advice, it was determined to withdraw the telescopic boom from the list and it was decided to only continue with the articulated boom and the CTM boom.

One might notice that the original design already contained articulated booms. However, this design had a high mass compared to the rest of the system. Therefore, alternative options have to be investigated to redesign the articulated booms, so they will meet the mass budget.

In the following chapters these two boom types are (re)designed and analyses are performed to make a final comparison of the booms in a later stage of the report.

Material Selection 5

Next to the technology selection, a proper material selection is required prior to the design process of both the articulated boom and the CTM boom. This to ensure a lightweight design, while maintaining the required positioning accuracy. The material has influence on the total performance of the structure: the mechanical properties, physical properties, and chemical properties. While the chemical properties determine the durability of the structure, the mechanical and physical properties directly influence the mass and positioning accuracy of the structure. In this chapter these properties will be further explained and a trade-off between various materials is made.

5.1 Materials for Deployable Structures

Since the beginning of space flight, the common material used for deployable booms and masts was metal. However, in the ’90s research began on using lighter materials, such as composites. The challenge was, and still is, that the behaviour of composites is hard to predict, due to its non-linear behaviour [35].

5.1.1 Material Properties

When selecting a suitable material for a deployable structure, one has to take into account the advantages and limitations of different material properties. This is based on the general rules for material selection. According to the books *Spacecraft Systems Engineering* (2011) [36] and *The International Handbook of Space Technology* (2014) [17], the following properties should be taken into account:

1. Mechanical properties:
   (a) Specific strength and stiffness;
   (b) Fracture and fatigue resistance;
   (c) Creep.
2. Physical properties:
   (a) Coefficient of thermal expansion (CTE);
   (b) Thermo-optical properties;
   (c) Thermal conductivity.
3. Chemical properties:
   (a) Corrosion;
   (b) Stress corrosion resistance;

Next to these material properties, also specific environment properties need to be taken into account, looking at the temperature, thermo-cycling, vacuum (out-gassing), and radiation [17].

Mechanical properties The two most important mechanical properties for material selection of a deployable structure are specific strength and specific stiffness. If one wants to have a fair comparison between different materials with respect to strength and stiffness, one should compare the specific strength and specific stiffness of the materials. The specific strength or stiffness is the strength or stiffness of the material divided by its density. This is also known as the strength-to-weight or stiffness-to-weight ratio. Strength is an important parameter when looking at joints or areas of local load concentration. Although, looking at other parts of a deployable structure, stiffness more important than strength. The strength in those parts is determined by the buckling strengths, which is determined by the stiffness [36]. Note that

deployable structures should not only be designed for the loads it will encounter in space, but they must also withstand the loads it will encounter during stowage, transportation, and launch [37].

For single deployment mechanisms, fracture and fatigue resistance and creep are less important. Fracture resistance, or also known as fracture toughness, is the maximum stress-intensity factor that will cause failure in a material which contains a crack [38]. The fatigue resistance, or fatigue strength, is the amount of stress at which failure occurs after a certain number of cycles [39].

Physical properties The CTE is a very important property in the design of deployable structures. It is the factor that determines how much the material will elongate or shrink (also known as strain) per degree Celsius or Kelvin [39]. In satellites there is a lot of thermo-cycling, which means that the temperature of the satellite often varies between two extremes, depending on the location in its orbit. This can cause a lot of extra stresses in the structure, which can cause certain failures. As the positioning accuracy is a key element for space telescopes, one does want to have an as low as possible thermal expansion coefficient for the positioning structures, as this can affect the performance of the telescope drastically.

Subsequently, thermo-optical properties, such as the absorptivity and emissivity, and the thermal conductivity determine the temperature of the structure. In case of a mechanically good material, while its physical properties are not well suited, coating can be a solution. The most important part in choosing a material with respect to physical properties, is that the amount of deformation that can occur due to temperature, should be minimized.

Chemical properties Chemical properties are the least important trade-off parameters as they mostly focus on corrosion. One might discuss that corrosion is not important, as there is no atmosphere present in space, or at least such a low amount that it will not cause any corrosion. Nevertheless, the deployable structure is still developed, tested, and stored in a terrestrial environment. Stresses can occur due to its own weight, residual stresses, or the preloading of joints. This is mostly related to metal deployable structures. As a consequence of corrosion the structure is weakened and will fail below the normal stress the material can support. Therefore one should still take the stress corrosion resistance of the material into account. Nevertheless, in this report the chemical properties are not considered in the trade-off. This can be done in further phase of the DST project, for the detailed material analysis.

5.1.2 Comparison of Materials

The main metals used in deployable structures are aluminum alloys, stainless steel, nickel alloys, and titanium alloys [17]. These metals are found to be most suitable, based on the material selection factors, as presented in the previous subsection. As there is a continuous research and development of lighter, more reliable and stable materials in the aerospace industry, CFRP has become an important type of material of which structures are currently made of. The use of metals over the years have shown a lot of advantages, as certain types like stainless steel are very strong and stiff, or types as aluminum have a good specific stiffness and is relatively cheap to produce and manufacture. Nevertheless, CFRP has proven that it has even many advantages over the use of metals, even though it is more expensive.

The mechanical and physical properties of stainless steel, titanium, aluminum and CFRP are shown in Table 5.1, where ρ is the density, E or E_x is the Young's modulus,G or G_{yx} is the shear modulus, and α_T is the CTE. This table is copied from the *Spacecraft Systems Engineering* book [36] and adjustments have been made using other references [40]. The different types of CFRP are different lay-up configurations. Unidirectional laminates, which are specified with [0°], are normally used for strut tubes, while the multi-angle configurations are used when quasi-isotropic behaviour is needed, such as for plate elements [37].

Looking at the density column in Table 5.1, one can directly see that the density of CFRP is about two times lower than aluminum, three times lighter than titanium, and more than 5 times lighter than stainless steel. Nevertheless, as was already mentioned in the previous subsection, the best comparison can be made when looking at the specific stiffness (which is $(E, E_x)/\rho$ in Table 5.1). As for deployable booms,

Table 5.1 Mechanical properties and costs of metals and CFRP in different lay-up configurations [36, 40–42]

Material	Specification	Cost	ρ	E, E_x	G, G_{yx}	$(E, E_x)/\rho$	α_T
		[$/kg]	[g/cm^3]	[GPa]	[GPa]	[GPa/(g/cm^3)]	[μm/m K^{-1}]
Stainless steel	304L	2.70	7.8	193	78	25	17.2
Titanium	TI-6A1-4V	16.25	4.4	110	44	25	9.0
Aluminum	7075.T6	1.80	2.8	71	27	26	23.4
Invar	36	13.00	8.1	144	26	18	1.0
CFRP-L1*	[0˚]	110.00	1.5	154	8	101	0.3
CFRP-L2*	[±45˚]		1.5	11	39	7	
CFRP-L3*	$[\pm 45˚/0˚]_s$		1.5	84	22	55	
CFRP-L4*	[±45˚/90˚/0˚]		1.5	56	21	37	
* intermediate modulus carbon fiber/epoxy resin, 60% fibers by volume							

unidirectional laminates are most interesting, the L1 of the CFRP types will be considered. The specific stiffness of CFRP-L1, is about four times higher than all the metals shown in the table. This makes CFRP an ideal material for stiff and lightweight structures. Especially for space telescopes, where the stiffness is an important factor to keep the alignment of the optics stable at different conditions during the post-deployment phase [37].

5.2 Trade-off

From the values of Table 5.1, a trade-off can be made, to determine the most suitable material for the design process. In this section the trade-off parameters are discussed, followed by the trade-off itself and the discussion of the results.

5.2.1 Trade-off Parameters and Methodology

For this trade-off, it is chosen to use the most important mechanical properties, physical property and cost of the relevant material as trade-off parameters. Below a list is provided of the trade-off parameters in descending order:

1. Density (4)
2. Young's Modulus (3)
3. CTE (3)
4. Cost (2)
5. Shear Modulus (1)

As mass is one of the key parameters of the design, the density will have the highest weight. As already discussed, the positioning accuracy is determined by the stiffness and deformation due to thermal effects. Therefore it is chosen to give the Young's Modulus and the CTE a weight of 3. Furthermore the cost per kg is also of importance, as the design has to stay within a predefined cost budget. However, the total cost can be minimized by minimizing the mass of the material. Finally, the shear modulus plays a role in this trade-off as well. The shear modulus plays an important role in twisting resistance of the material. As the possibility for twisting to occur in the booms is minimal the shear modulus gets the lowest weight.

The main difference between the trade-off in this chapter and the trade-off in chapter 4, is that real values are used to determine the individual scores, which will make the trade-off more objective. As there are

five materials, a score is given from 1 to 5. 1 indicates the worst value of the specific trade-off parameter and 5 indicates the best value. For example, the lowest density from Table 5.1 is 1.5 g/cm^3 (CFRP) and the highest value is 8.1 g/cm^3 (Invar). In this case 1 is assigned to 8.1 g/cm^3 and 5 is assigned to 1.5 g/cm^3. Using these scores and values, a linear relation can be written to determine the scores of the other density values. These scores are rounded to the nearest integer. This is done for each trade-off parameter. Note for density and cost, the lower the value, the higher the score, and for the other parameters this is the other way around.

5.2.2 Results and Discussion

In Figure 5.1 the results of the trade-off is shown.

Criteria / Material	Density	Young's Modulus	CTE	Cost	Shear Modulus	Score
	4	3	3	2	1	Max. 5
Stainless Steel	1	5	2	5	5	! 3.1
Titanium	3	2	3	4	3	✗ 2.3
Aluminum	4	1	1	5	2	✗ 1.8
Invar	1	3	5	5	2	✗ 2.3
CFRP	5	4	5	1	1	✓ 3.7

Figure 5.1 Material trade-off result

From Table 5.1 it could almost already be concluded that CFRP would be the best option for the main material of the booms. This is also proven in Figure 5.1. In the original design of the DST telescope, Dolkens had chosen for Invar as main material for the articulated booms, as it had an extremely low CTE. Nevertheless, when comparing the mechanical properties it shows that CFRP would be a much better option. The second best scoring material is stainless steel: it is relatively cheap and strong. Nevertheless, stainless steel has a high density, so it would introduce a lot of mass to the system if the whole boom would be made out of stainless steel. Therefore stainless steel can be considered for certain parts of the deployable structure, such as hinges of parts of the HDRM.

With this trade-off result, the preliminary research process can be concluded. From the technology selection process (chapter 4) it was determined that CTM booms and articulated booms are the best options for further analysis and this chapter has shown that CFRP would be the most suitable material for the arms of the booms. In the following part, the design process of both booms will take place.

II

Design Process

Design Fundamentals 6

In this chapter the fundamentals for the design of the deployable booms are presented. Next to the earlier given design requirements in chapter 2, this information is required to perform a correct design process of the booms. First the load cases are discussed. Multiple equations will be given and derived, which will be needed in the following chapters. Furthermore the optimal boom length is determined by comparing the optical and mechanical performances. Finally, an elaborate CFRP material analysis is done, which needs to be taken into account during the design process of both booms.

6.1 Load Cases

The design of the booms should be done according to properly defined load cases. For each load case the boom shall have to withstand the predefined loads and while still performing within the alignment budget. In this section the load cases are divided in quasi-static loads and dynamic loads. The thermal loads will be treated separately later in the report in section 9.2. Each of the load cases will be discussed and relevant equations will be given, which will be used during the design phase. An important note is that in this section the assumption is made that the booms are fully clamped at the root. The effects of root clamping will be discussed later in this report.

6.1.1 Worst Case Scenario

Before the load cases can be described, it has to be specified for which design this preliminary design and analysis will be performed. Therefore, the both designs need to be compared to determine which can be considered as a worst case scenario. The full design consists of four booms, which carry a secondary mirror and interface plate with a total mass of about 5 kg. Assuming an even distribution of the loads, each boom will carry 12 N at 1-g. Comparing this to the downscaled design, it can already be seen that the downscaled version has a larger load to carry, as the OEB is assumed to be 3 kg and only a single boom is used to support this element. Therefore it can be concluded that the downscaled version is the worst case scenario between the two in terms of load cases. The rest of the design process, analysis and comparison in this part of the report are therefore based on the downscaled model.

6.1.2 Quasi-static Loads

Once the boom is deployed, gravity will have influence on the achievable positioning accuracy of the boom. Even though this gravity is so called micro-gravity, it is enough to deflect the boom in the micrometer range. Decentering of the optical element will occur if the gravity acts perpendicular to the lateral axis of the boom, while despacing will occur if the gravity acts in the longitudinal direction. Both cases will be discussed.

Lateral If the boom is oriented such that the gravity is pointed perpendicular to the longitudinal axes, the boom will experience a deflection in the same direction as the gravitational acceleration. In Figure 6.1 the load cases are sketched for both boom types.

The following assumptions are made:

- The booms are treated as cantilever beams;
- Both booms have a uniformal mass distribution along the total length;
- The segments of the articulated boom are treated as a continuous boom, to simplify the theoretical calculations. This simplification is valid since the mass of the hinges will have a significantly larger impact on the total deflection of the boom, than the mass of the individual segments;

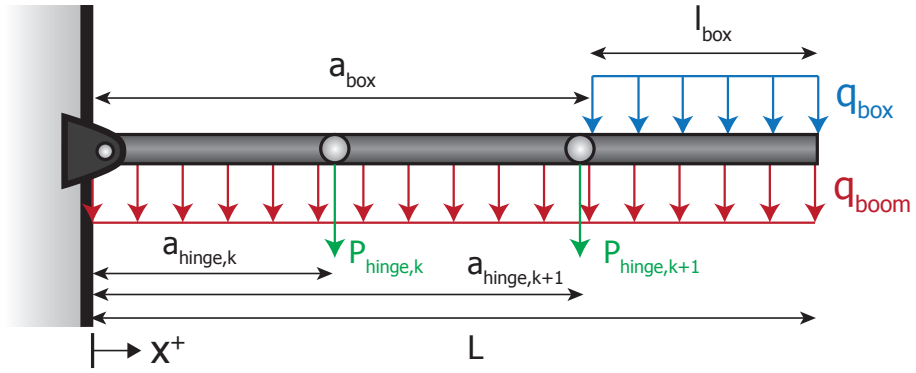

(a) Articulated boom

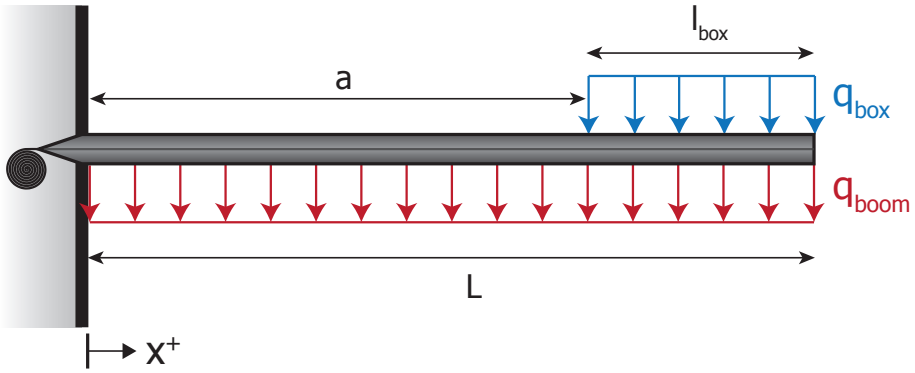

(b) CTM boom

Figure 6.1 Lateral quasi-static load cases

- The hinges are point masses;
- The optical element box is an evenly distributed load with a variable length;

From Figure 6.1, the maximum (tip) deflection can be expressed. Each boom has a combination of different load cases. Adding the maximum deflection of each individual case will result in a total maximum deflection of the boom. The maximum deflection due to a continuous distributed load over the total length, such as the own weight of the boom, is expressed as [43]:

$$\delta_{max} = \frac{qL^4}{8EI} \tag{6.1}$$

Where δ_{max} is the maximum tip deflection in [m], q is the distributed load in [N/m], L is the total length of the boom in [m], E is the Young's Modulus of the material in [Pa], and I is the moment of inertia in [m^4].

As was already stated, the hinges of Figure 6.1a are treated as point loads, so the deflection due to a single point load is stated as [43]:

$$\delta_{max} = \frac{Pa^2}{6EI}(3L - a) \tag{6.2}$$

Where P is the point load in [N] and a is the distance from the root of the boom to the point load in [m].

The final load which is shown in both load cases in Figure 6.1, is the distributed load of the optical element box. The maximum deflection of this distributed tip load is expressed as [43]:

$$\delta_{max} = \frac{q}{24EI}\left(3L^4 - 4a^3L + a^4\right) \tag{6.3}$$

Where a is the distance from the root of the boom to the left boundary of the distributed load in [m].

The total deflection of the booms, can be derived taking the sum of the individual load cases. The total deflection of the articulated boom (Figure 6.1a) is formulated as:

$$\delta_{max} = \left(\delta_{max}\right)_{boom} + \left(\delta_{max}\right)_{box} + \sum_{k=1}^{n} \left(\delta_{max}\right)_{hinge_k} \tag{6.4}$$

$$\delta_{max} = \frac{q_{boom} L^4}{8EI} + \frac{q_{box}}{24EI}\left(3L^4 - 4a_{box}^3 L + a_{box}^4\right) + \sum_{k=1}^{n} \frac{P_{hinge_k} a_{hinge_k}^2}{6EI}\left(3L - a_{hinge_k}\right)$$

Where k is the number of the hinge, starting at 1, and n is the total number of hinges.

The total deflection of the CTM boom (Figure 6.1b) only consists of the first two parts of Equation 6.4:

$$\begin{aligned} \delta_{max} &= \left(\delta_{max}\right)_{boom} + \left(\delta_{max}\right)_{box} \\ &= \frac{q_{boom} L^4}{8EI} + \frac{q_{box}}{24EI}\left(3L^4 - 4a^3 L + a^4\right) \end{aligned} \tag{6.5}$$

Equations 6.4 and 6.5, will be used for the design of the booms in chapters 7 and 8.

Longitudinal If the gravity is pointed in the longitudinal direction of the boom, the design should withstand significant elongation or contraction due to tensional or compressive loads, depending on the direction of the gravity, and should not buckle. Nevertheless, as the booms are operating in a micro-gravity environment, it is not expected that longitudinal loads will have significant impact on the decentering of the optical element. Still the design should be checked on these cases.

The elongation or contraction can be derived from the stress (Equation 6.6), strain (Equation 6.7), and Young's Modulus (Equation 6.8) equations :

$$\sigma = \frac{F}{A} \tag{6.6}$$

$$\varepsilon = \frac{L' - L}{L} = \frac{\delta}{L} \tag{6.7}$$

$$E = \frac{\delta}{\varepsilon} = \frac{FL}{A\delta} \tag{6.8}$$

Where σ is the stress in [Pa], ε is the strain, F is the load in longitudinal direction in [N] (e.g. the weight of the optical element box or secondary mirror), L' is the new length of the boom in [m], L is the original length of the boom in [m], and A is the cross-sectional area of the boom in [m^2].

From these equations the maximum deflection in longitudinal direction can be calculated as:

$$\delta_{max} = \frac{EA}{FL} \tag{6.9}$$

Note that the sign convention of F will determine whether the boom is elongated or contracted.

The buckling of the boom can be checked by using Euler's buckling equation:

$$P_{cr} = \frac{\pi^2 EI}{L_{eff}^2} \tag{6.10}$$

Where, P_{cr} is the critical buckling load in [N], and L_{eff} is the effective length of the boom in [m].

This effective length, however, is dependent on the boundary conditions of the situation, as can be seen in Figure 6.2. For the demonstration mission, the fourth case (from left) is the most representative case with an effective length of $2L$, while for the original mission, the most right case would be most representative

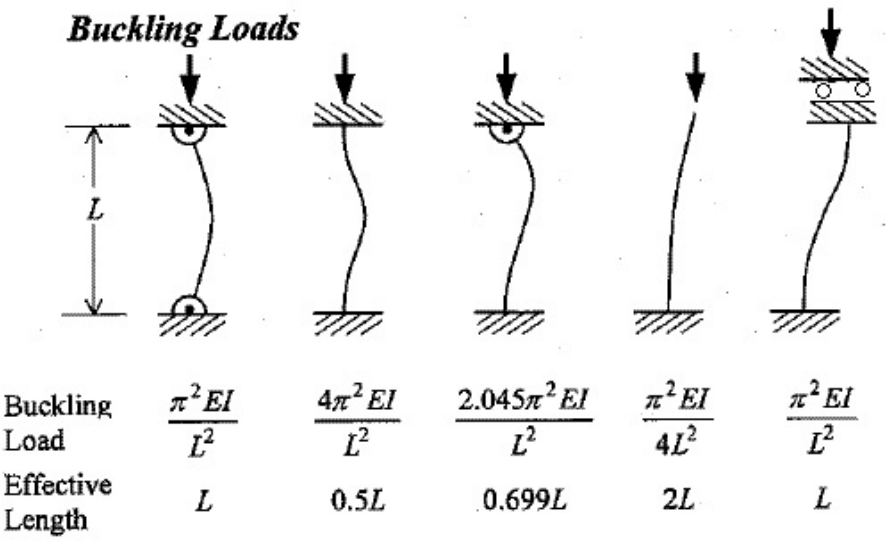

Figure 6.2 Buckling load cases [44]

with an effective length of L. Since the design has to be designed for worst case, the fourth case will be used as reference, as this will result in a lower critical buckling load. Using the boom properties, the critical buckling load can be calculated. The load due to the mass of the optical element box or secondary mirror should be less then the critical buckling load.

6.1.3 Dynamic Loads

Next to the quasi-static loads, the boom will be subjected to dynamic loads, such as vibrational loads, by other components of the satellite and disturbance forces acting on the satellite itself, while operating in orbit. If these loads vibrate in the same frequency as the natural frequency of the boom, the boom will start to resonate which will have catastrophic effects on the performance of the space telescope. In chapter 2, the frequency requirements already have been determined. In this subsection the equations needed to calculate the natural frequencies of the boom are presented.

Two situations need to be considered: the natural frequency of the boom itself and the natural frequency with a tip mass e.g. the optical element box. The situation is sketched below.

(a) Vibration without tip mass **(b)** Vibration with tip mass m

Figure 6.3 Beam vibration situations

For the situation shown in Figure 6.3a, the natural frequencies can be calculated using the following equation [45]:

$$f = \frac{K_n}{2\pi L^2}\sqrt{\frac{EI}{m}} \tag{6.11}$$

Where K_n is a constant which is dependent on the mode of vibration n, L is the total length of the boom in [m], and m is the mass of the boom in [kg]. In order to calculate the modes of natural frequencies, K

will vary per mode. In Table 6.1 the values of K_n per mode are shown.

Table 6.1 Values of K_n for different modes n [45]

Mode	1	2	3	4	5
K_n	3.52	22.0	61.7	121	200

The second case, Figure 6.3b, assumes that the tip mass is significantly greater than the boom mass. Using this assumption, the natural frequency is calculated using Equation 6.12 [45]:

$$f = \frac{1}{2\pi}\sqrt{\frac{3EI}{m_{tip}L^3}} \tag{6.12}$$

Where m_{tip} is the tip mass in [kg] and L is the total length of the boom in [m], so not including the length of the tip mass.

Equation 6.11 and Equation 6.12 will be used in a later part of this report to analytically check if the design meets the frequency requirements.

6.2 Boom Length

As could be seen in the previous section, the boom length has significant impact on the deflection and natural frequencies, which in their case will have impact on the positioning accuracy of the boom. From a mechanical perspective, a shorter boom would be more optimal. However, this is not beneficial from an optical perspective. The system will become more sensitive for misalignment, so a tighter alignment budget is needed, which will have impact on the mechanical design as well. As the boom length can have negative and positive effects on the performance of the system, an optimal design point should be found, looking on both the optical and mechanical performance. In this section, the optimal design point will be determined.

6.2.1 Optical Performance

In order to measure the optical performance as a function of the boom length, the Strehl ratio is used. The Strehl ratio can be defined as the quality of optical image formation in terms of aberrations, measured by using the ratio of peak diffraction intensities of an aberrated and perfect wavefront [46]. In Figure 6.4 the constraints of the design by Dolkens are shown.

The Maréchal criterion defines that a minimum Strehl ratio of 0.8 would mean that the focal spot is diffraction limited, which means that it can be considered as aberration-free. If the Strehl ratio is lower than 0.8, the smallest details of the focal spot cannot be resolved as the image would be too blurry [47].

The Strehl ratios of different boom lengths were obtained through simulation, using a conic mirror design and a freeform mirror design (Figure 6.4) for M3. A freeform mirror is a mirror with a surface that has no axis of rotational invariance. In other words they have an arbitrary shape and can have irregular or regular surface structures [48]. The results of the simulations are shown in Figure 6.5.

From each design the mean Strehl, the worst Strehl, and the Strehl ratio at a field of view (FOV) of 90% are plotted. The panchromatic (PAN) channels often relate to the mean Strehl ratio, while the multispectral (MS) channels relate to the worst Strehl ratio. In Figure 6.5 two horizontal lines are plotted, which relate to the Strehl ratios 0.7 and 0.8. As was already stated, a diffraction-limited Strehl ratio would be 0.8 and higher. From this line, it can be derived that the boom length should be higher than about 1.43 m (based on the worst Strehl ratio of both designs). Note that the Strehl ratio drops from about 1.6 m, however this is not relevant for this analysis, as the maximum boom length would be 1.6 m.

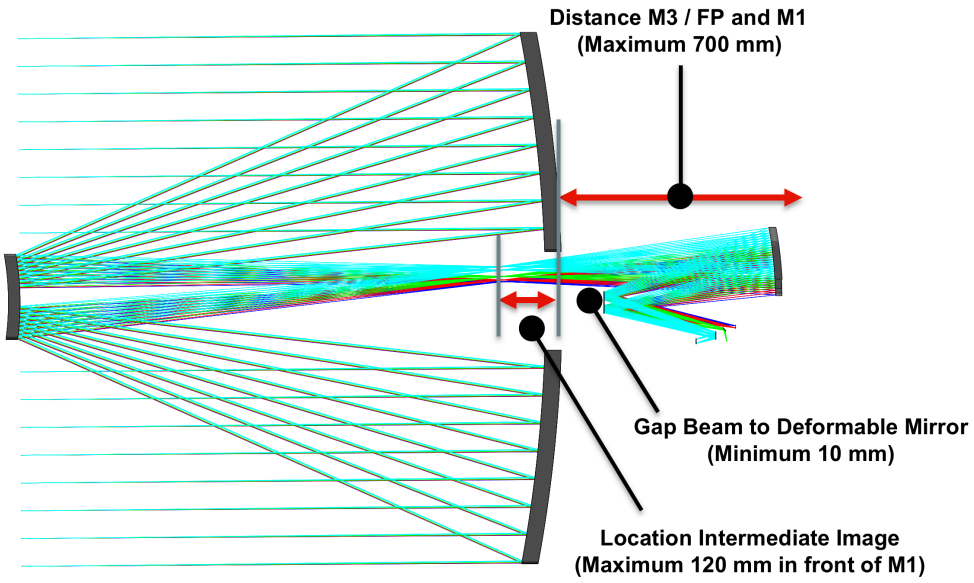

Figure 6.4 Optical constraints of original design (image credit: D. Dolkens)

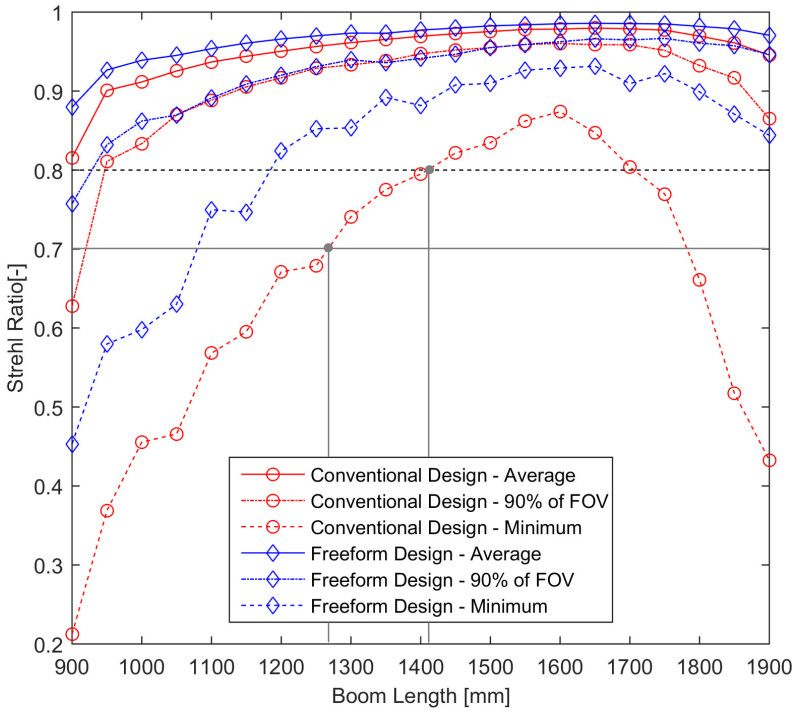

Figure 6.5 Optical performance (image credit: D. Dolkens)

Dolkens determined that a Strehl ratio of 0.7 would still be feasible, as the images could be corrected using image processing techniques. Reducing this limit, results in a lower boom length. From the figure it can be seen that the boom length would drop from 1.41 to about 1.27 m, which means that this can have a significant impact on the deflection in the lateral load cases (subsection 6.1.2), as this is dependent on L^3 or even L^4. However, due to the effect of the boom length on the tolerances of M1, the length of boom cannot be lower than 1.3 m.

When comparing the conic design and freeform design it can be seen that a freeform mirror has a better performance in terms of Strehl ratio. This means that the length of the boom could even further be reduced if a freeform mirror is chosen. Nevertheless, this design option is still not finally determined yet, and therefore the worst case scenario should be chosen in the boom design. In conclusion for the

best optical performance, the boom length shall be greater than 1.3 m, which is an improvement of 19% compared to the original design. Note that the values in Figure 6.5 are conservative. The values are currently being optimized, with the expectation of leading to a better performance.

6.2.2 Mechanical Performance

In order to achieve the desired optical performance, the mechanical performance should comply with the alignment budget. This analysis is performed with the demonstration mission set-up. The box containing the optical elements for the downscaled design, has not been designed yet. As this parameter will have influence on the deflection, it has been chosen to use three different values for the length of the box: 10 cm, 20 cm and 30 cm. This is also used to investigate the effect of the size of the box on the mechanical performance. As was already seen in the previous section, the boom is more sensitive for lateral deflection than longitudinal deflection. Therefore it is chosen to only investigate the lateral deflection as a function of boom length. The most simple case of Figure 6.1, is the CTM boom load case which can be treated as a cantilever boom with two distributed masses. As the cross-section of a CTM boom is dependent on various parameters, a hollow tube is chosen in stead of a CTM boom, to simplify the analysis. In order to find the normalized deflection, Equation 6.5 is rewritten as:

$$\delta_{max_{norm}} = \frac{\delta_{max}(a, L)}{\delta_{max}(a_{max}, L_{max})} = \frac{q_{box}\left(3L^4 - 4a^3L + a^4\right) + q_{boom}L^4}{q_{box}\left(3L_{max}^4 - 4a_{max}^3L_{max} + a_{max}^4\right) + q_{boom}L_{max}^4} \tag{6.13}$$

As Equation 6.13 is both a function of the gravitational acceleration g in the numerator as in the denominator, g gets canceled and Equation 6.13 is thus independent of g. The assumption is made that the box has a mass of 3 kg and the boom has an outer diameter of 5 cm and a thickness of 0.3 mm. Note that these values are only used for this trade-off and do not illustrate the final design. The normalized deflection as a function of the boom length is calculated and plotted, which is shown in Figure 6.6.

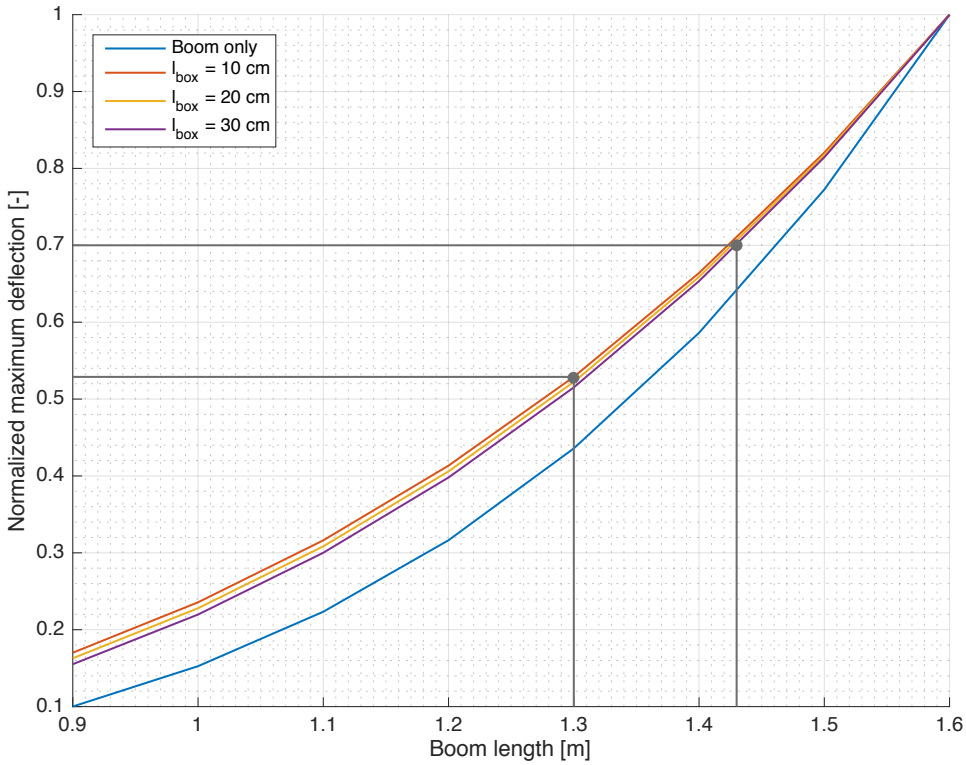

Figure 6.6 Mechanical performance

What can be noticed from Figure 6.6, is that the length of the box has minimal impact on the normalized maximum deflection, however when no tip mass is used on the boom, the boom is more sensitive for deflections depending on the boom length. A reduction of 70 cm in boom length, results in deflection of 16% (or 0.16) of the maximum deflection.

Using the boom lengths of 1.3 m and 1.43 m, which were determined in the optical performance analysis, the normalized maximum deflection can be obtained from Figure 6.6. As the boom with a box is more representative for the final design, the average of these graphs is taken and the corresponding normalized deflection is retrieved. The values are 0.53 and 0.70 for the lengths of 1.3 and 1.43 m, respectively. This is a significant drop in deflection.

6.2.3 Optimal Boom Length

From Figure 6.5 it was determined that a minimum boom length of 1.43 m is required to have a diffraction-limited system. However, using image post-processing techniques, a Strehl ratio of 0.7 would be satisfactory, which would mean that boom length would drop to about 1.3 m. This post-processing is considered as extra effort and is only valuable if the drop in boom length would have significant impact on the mechanical performance as well. As could be seen in Figure 6.6, the drop from 1.43 m to 1.3 m did have significant impact on the normalized maximum deflection. Therefore, it can be concluded that the optimal boom length would be 1.3 m.

6.3 CFRP Laminate Design

In chapter 5 it was found that CFRP is the most suitable material for the booms. CFRP consists of a polymer matrix and is reinforced with carbon fibers. These fibers have a very high tensile strength. The global mechanical and physical properties of a CFRP laminate is highly dependent on the orientation of the fibers in each individual ply. This could already be noticed in the bottom part of Table 5.1. These properties are required for determining the stiffness, deflections in various load cases, as well as the CTE in all directions of the booms. In this section, the derivations of individual to global properties are shown and the effect of the orientation and the layer sequence on the material properties are discussed.

6.3.1 Classical Lamination Theory

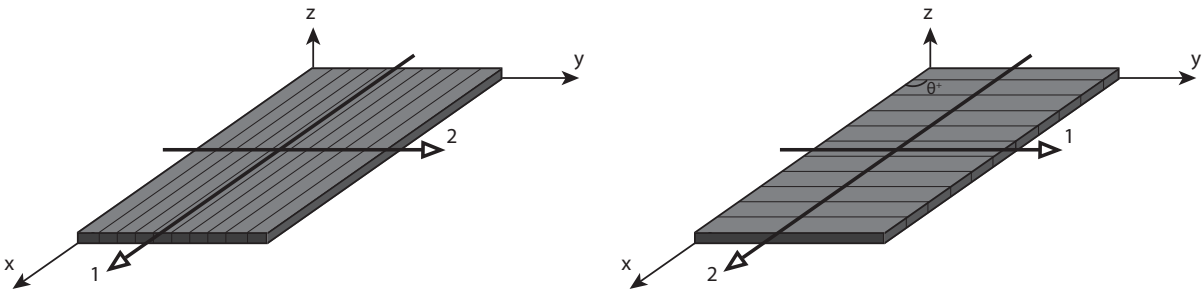

(a) Fibers at 0° from x-axis **(b)** Fibers at 90° from x-axis

Figure 6.7 Principal axes of orthotropy for plies

To derive the global CFRP properties from the individual ply properties, the classical lamination theory is used [49–51]. The individual ply properties are based on a [0˚] ply, in which the longitudinal axis (direction 1) is parallel to the *x*-axis of the plate and the transverse axis (direction 2) is parallel to the *y*-axis of the plate, which can be seen in Figure 6.7a. The stress-strain relation in this case can be calculated

with the following equations:

$$\sigma_1 = \frac{E_1}{1 - \nu_{12}\nu_{21}} \left(\varepsilon_1 + \nu_{21}\varepsilon_2\right) \tag{6.14}$$

$$\sigma_2 = \frac{E_2}{1 - \nu_{12}\nu_{21}} \left(\nu_{12}\varepsilon_1 + \varepsilon_2\right) \tag{6.15}$$

$$\tau_{12} = G_{12}\gamma_{12} \tag{6.16}$$

Where σ_1 and σ_2 are the principal stresses in longitudinal and transverse direction in [Pa], E_1 and E_2 are the Young's moduli in longitudinal and transverse direction in [Pa], ε_1 and ε_1 are the strain in longitudinal and transverse direction, ν_{12} and ν_{21} are the Poisson ratios in longitudinal and transverse direction, τ_{12} is the in-plane shear stress in [Pa], G_{12} is the shear modulus in [Pa], and γ_{12} is the shear strain.

Equations 6.14 to 6.16 can be written in a matrix form $\hat{\sigma} = [Q]\hat{\varepsilon}$:

$$\begin{Bmatrix} \sigma_1 \\ \sigma_2 \\ \tau_{12} \end{Bmatrix} = \begin{bmatrix} Q_{11} & Q_{12} & 0 \\ Q_{21} & Q_{22} & 0 \\ 0 & 0 & Q_{66} \end{bmatrix} \begin{Bmatrix} \varepsilon_1 \\ \varepsilon_2 \\ \gamma_{12} \end{Bmatrix} \tag{6.17}$$

Where:

$$Q_{11} = \frac{E_1}{1 - \nu_{12}\nu_{21}} \tag{6.18}$$

$$Q_{12} = Q_{21} = \frac{\nu_{21}E_1}{1 - \nu_{12}\nu_{21}} = \frac{\nu_{12}E_2}{1 - \nu_{12}\nu_{21}} \tag{6.19}$$

$$Q_{22} = \frac{E_2}{1 - \nu_{12}\nu_{21}} \tag{6.20}$$

$$Q_{66} = G_{12} \tag{6.21}$$

According to the Betty-Maxwell theory and symmetry condition the following relation should apply: $E_1\nu_{21} = E_2\nu_{12}$. Therefore $Q_{12} = Q_{21}$. If the mechanical properties of the ply are not known, one should calculate the properties from the volume fractions. The corresponding equations, however, are not treated in this report.

When the fibers are rotated with respect to the x-axis, as is the case in Figure 6.7b, the principle axes of orthotropy are not parallel anymore to the corresponding global x and y-axes. Therefore the stress-strain relation of Equation 6.17 cannot be used anymore. The local $[Q]$ matrix has to be transformed to the global $[\overline{Q}]$ matrix [52]. To transform the local $[Q]$ matrix to the global $[\overline{Q}]$ matrix, the following transformation is applied:

$$[\overline{Q}] = [T]^{-1}[Q][T]^{-T} \tag{6.22}$$

Where:

$$[T]^{-1} = \begin{bmatrix} \cos^2\theta & \sin^2\theta & -2\cos\theta\sin\theta \\ \sin^2\theta & \cos^2\theta & 2\cos\theta\sin\theta \\ \cos\theta\sin\theta & -\cos\theta\sin\theta & \cos^2\theta - \sin^2\theta \end{bmatrix} \tag{6.23}$$

$$[T]^{-T} = \begin{bmatrix} \cos^2\theta & \sin^2\theta & \cos\theta\sin\theta \\ \sin^2\theta & \cos^2\theta & -\cos\theta\sin\theta \\ -2\cos\theta\sin\theta & 2\cos\theta\sin\theta & \cos^2\theta - \sin^2\theta \end{bmatrix} \tag{6.24}$$

Once matrix $[\overline{Q}]$ is calculated for the given ply or plies, the laminate stiffness matrices can be calculated.

The laminate stiffness matrices is also called the $[ABD]$ matrix, as it has the following form:

$$[ABD] = \begin{bmatrix} [A] & [B] \\ [B] & [D] \end{bmatrix} = \begin{bmatrix} A_{11} & A_{12} & A_{16} & B_{11} & B_{12} & B_{16} \\ A_{21} & A_{22} & A_{26} & B_{21} & B_{22} & B_{26} \\ A_{61} & A_{62} & A_{66} & B_{61} & B_{62} & B_{66} \\ B_{11} & B_{12} & B_{16} & D_{11} & D_{12} & D_{16} \\ B_{21} & B_{22} & B_{26} & D_{21} & D_{22} & D_{26} \\ B_{61} & B_{62} & B_{66} & D_{61} & D_{62} & D_{66} \end{bmatrix} \tag{6.25}$$

Where [A] is the membrane stiffness matrix, [B] is the membrane-bending stiffness matrix, and [D] is the bending stiffness matrix [51]. These matrices are calculated using the following equations:

$$A_{ij} = \sum_{k=1}^{n} [\overline{Q}]_{ij}^{(k)} \left(z_k - z_{k-1}\right) \tag{6.26}$$

$$B_{ij} = \sum_{k=1}^{n} \frac{1}{2} [\overline{Q}]_{ij}^{(k)} \left(z_k^2 - z_{k-1}^2\right) \tag{6.27}$$

$$D_{ij} = \sum_{k=1}^{n} \frac{1}{3} [\overline{Q}]_{ij}^{(k)} \left(z_k^3 - z_{k-1}^3\right) \tag{6.28}$$

Where i is the row, j is the column, k is ply number, n is the total number of plies, and z is the z-coordinate of the lower face of the ply measured from the mid-plane of the laminate in [m]. This is illustrated in Figure 6.8.

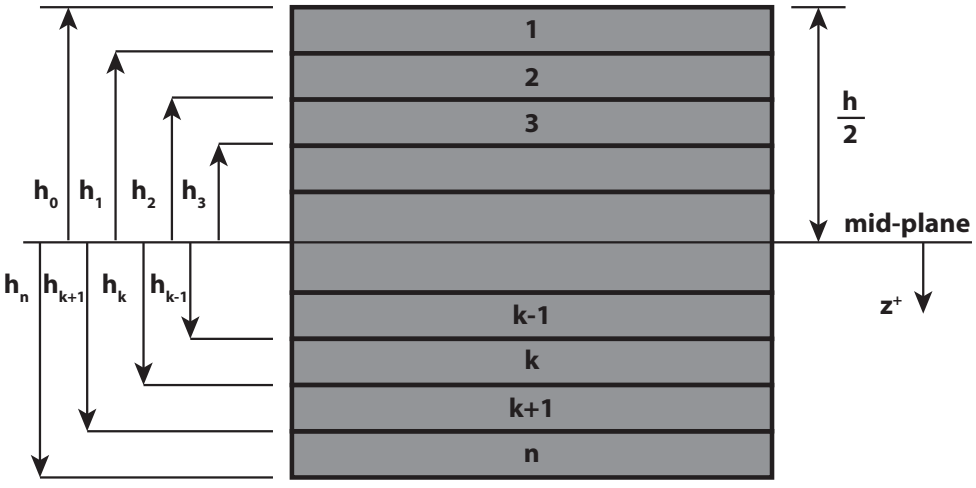

Figure 6.8 z coordinate system of plies in laminate

From these laminate stiffness matrices the global laminate properties can be calculated . The mechanical properties can be calculated using equations 6.29 to 6.33. Note that $[a] = [A]^{-1}$.

$$E_x = \frac{1}{ha_{11}} \tag{6.29}$$

$$E_y = \frac{1}{ha_{22}} \tag{6.30}$$

$$G_{xy} = \frac{1}{ha_{66}} \tag{6.31}$$

$$\nu_{xy} = -\frac{a_{21}}{a_{11}} \tag{6.32}$$

$$\nu_{yx} = -\frac{a_{21}}{a_{22}} \tag{6.33}$$

Next to the mechanical properties, the global CTE can be calculated using Equation 6.34:

$$\begin{Bmatrix} \alpha_x \\ \alpha_y \\ \alpha_{xy} \end{Bmatrix} = [a] \sum_{k=1}^{n} [\overline{Q}]_{ij}^{(k)} \left(z_k - z_{k-1} \right) \begin{Bmatrix} \alpha_1 \\ \alpha_2 \\ \alpha_{12} \end{Bmatrix}^{(k)} \tag{6.34}$$

Using the equations provided in this subsection, a proper laminate design can be performed, which is needed for further analysis in chapter 9. A MATLAB code is written, in which the individual ply properties and orientation can be entered, and the corresponding laminate properties are calculated. The code can be found in section A.1 of Appendix A. The code is validated by using values of different literature sources [50, 51, 53].

6.3.2 Stacking Sequence

Before analyzing the effects of individual plies on the laminate properties, a better understanding of the stacking sequence need to be provided [54]. The stacking sequence determine on whether the laminate is isotropic or quasi-isotropic. Isotropic means that the laminate has the same properties in both the longitudinal as the transverse direction. Quasi-isotropic means that in-plane properties are isotropic. In order to achieve an isotropic or quasi-isotropic CFRP laminate, multiple thin unidirectional plies are stacked on top of each other. If a laminate is symmetric, the plies above the mid-plane are a mirrored version of the plies below the mid-plane. If a laminate is not symmetrical, bending and twisting in the material can occur even if the external moment is zero. Also thermal twisting can occur. Therefore, in practical cases, one wants to have a symmetrical laminate. All elements of the $[\boldsymbol{B}]$ matrix of Equation 6.25 will be 0. If the amount of positive and negative angled plies is balanced, the laminate is also called balanced.

In this report the laminate stacking sequence notation is used. To give a better understanding of this notation, the notation steps are explained below [55]:

1. The stacking sequence starts from the top of the laminate;
2. Bracket symbols are used to enclose the stacking sequence, […];
3. A slash symbol, /, is used to separate the plies or groups of plies;
4. If plies are repeated in a sequence, subscript n is used for the common fiber direction, e.g. $[45_n]$, where n is the number of plies;
5. If a positive oriented ply is followed by a negative oriented ply, a $\pm$ sign is used in front of the angle of the plies, e.g. $[\pm 45]$;
6. If the laminate is symmetric, only the part above the mid-plane is noted, followed by a subscript s after the closing bracket, $[\dots]_s$;

6.3.3 Effects of Stacking

As was shown throughout this section, the orientation of the fibers of the ply will have affect on overall laminate properties. The MATLAB code was used to analyze the effects of the ply orientation, ply thickness and number of plies on the laminate properties. For this analysis, the mechanical properties of an IM-7/977–2 CFRP lamina are used, which are shown in Table 6.2.

Table 6.2 Mechanical properties of IM-7/977–2 CFRP ply [53]

ρ	E_1	E_2	G_{12}	ν_{12}
[kg/m^3]	[GPa]	[GPa]	[GPa]	[-]
1578	173	9.17	5.65	0.34

Ply Orientation For the first analysis a symmetrical laminate is chosen, which consist of four layers. The outer layers are 0° plies with two variable inner plies. As the laminate should be balanced, these inner plies have the same angle θ, however have opposite sign conventions. In other words it is a $[0/\pm\theta]_s$ laminate. θ is varied from 0° to 90°. The assumption is made that all layers have the same thickness. In Figure 6.9, the ply orientation is plotted against the Young's modulus and shear modulus.

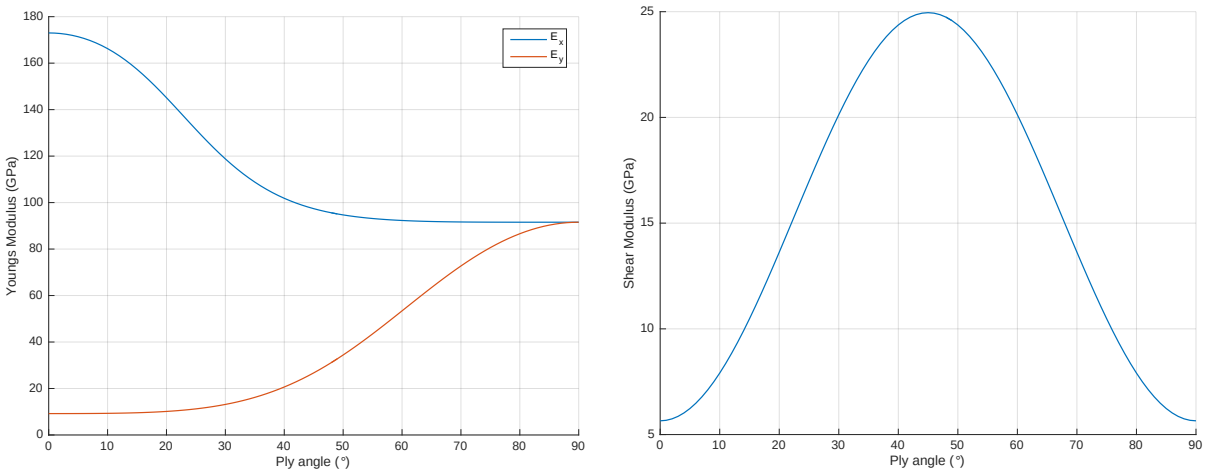

(a) Young's modulus **(b)** Shear modulus

Figure 6.9 Effect of ply orientation on mechanical properties at $t_1 = t_2$

In Figure 6.9a it can be seen that increasing the ply angle has a positive effect for the Young's modulus in transverse direction (E_y), but a negative effect for the Young's modulus in longitudinal direction (E_x). The laminate becomes isotropic, if $\theta = 90°$. Figure 6.9b shows that the highest shear modulus can be obtained when $\theta = 45°$. The shear modulus at this point has increased with a factor of about 4.5 from the original shear modulus.

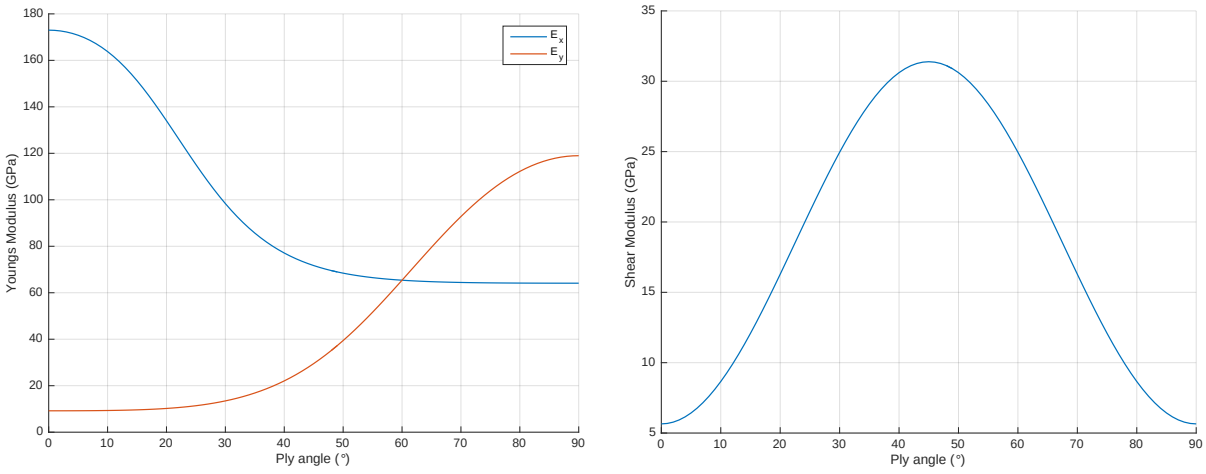

(a) Young's modulus **(b)** Shear modulus

Figure 6.10 Effect of ply orientation on mechanical properties at $2t_1 = t_2$

When the thickness of the inner plies are increased with a factor of two, a significant difference in the results can be observed. This is shown in Figure 6.10. E_x will drop to about 62 GPa, while E_y increases to 120 GPa when $\theta = 90°$. The laminate is isotropic at $\theta = 60°$, however the Young's modulus of the isotropic laminate is about 65 GPa, while the isotropic laminate with layers of equal thickness had a Young's modulus of about 90 GPa. The shear modulus, on the other hand, has increased from a maximum of 25 GPa to a maximum of about 32 GPa. Increasing the inner thickness with a factor of two, does have positive impact on the shear modulus and transverse Young's modulus, but has a negative impact on the

longitudinal Young's modulus.

Ply Thickness Since the first analysis has shown that ply thickness does have significant effect on the mechanical properties of the laminate, further analysis of the thickness is done. For this analysis two laminates are considered: a $[0/\pm 45]_s$ laminate and a $[0/90]_s$ laminate. The thickness of the outer 0° plies are labeled as t_1 and the thickness of the inner plies are labeled as t_2. To determine which thickness ratio is most favorable for the two laminates, the Young's modulus and shear modulus are plotted as a function of t_2/t_1 and can be seen in Figure 6.11 and Figure 6.12. In order to see the limit of the mechanical properties, it is chosen to vary t_2/t_1 from 1 to 100, however from a practical perspective one should only consider ratios from 1 to 10.

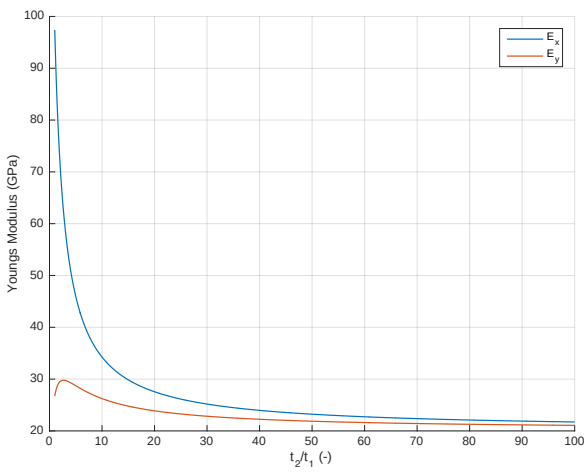

(a) Young's modulus

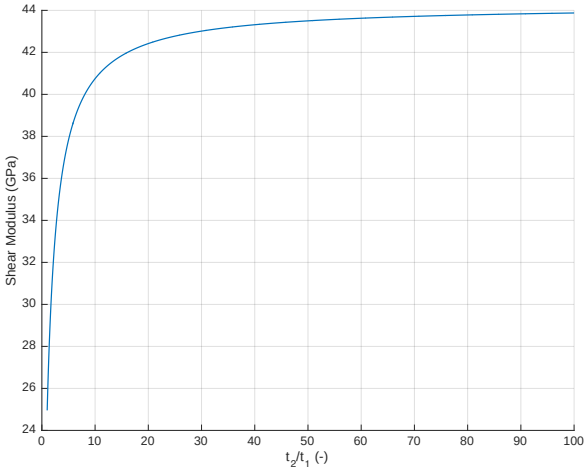

(b) Shear modulus

Figure 6.11 Effect of ply thickness on mechanical properties for $[0/\pm 45]_s$ layup

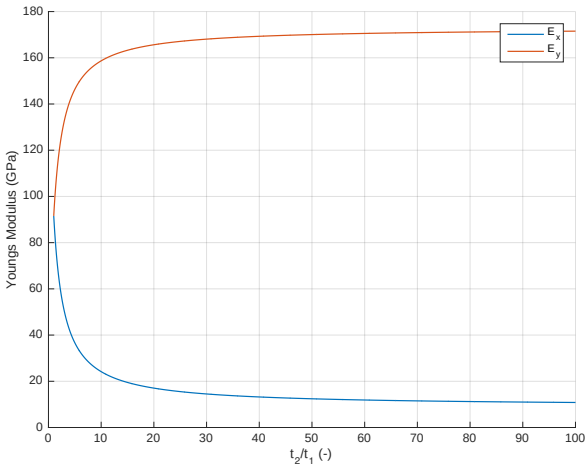

(a) Young's modulus

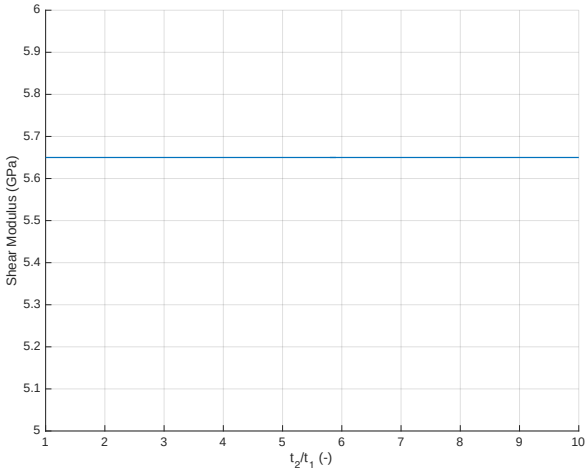

(b) Shear modulus

Figure 6.12 Effect of ply thickness on mechanical properties for $[0/90]_s$ layup

Figure 6.11a shows a significant drop in E_x when increasing the thickness, while E_y has a peak value and will drop afterwards. The optimal thickness ratio for E_y is in this case 2.7. The shear modulus in Figure 6.11b has a significant increase when the ratio is between 1 and 10. When the ratio approaches 100, a limit of about 44 GPa will be reached.

When the inner plies are 90°, it can clearly be seen in Figure 6.12a that E_x and E_y will be reversed. This means that for such a laminate, it would not be beneficial to increase the thickness. This is also seen in Figure 6.12a, where the shear modulus is not affected by the ratio, which is different than for the $[0/\pm 45]_s$ laminate.

The thickness can also be increased by stacking multiple plies in the same orientation. The effect of this case can therefore also be determined from Figure 6.11 and Figure 6.12. If a laminate consists only of plies in one direction, the number of plies will not have effect values of the Young's modulus and shear modulus. This, however, is in theory. In practical case, the mechanical properties might be slightly affected as the plies are bonded, although this will not have significant impact on the results.

6.3.4 Preliminary Laminate Design

From the analysis in subsection 6.3.3, it could be concluded that:

1. Ply orientation has positive and negative effects on the Young's modulus, depending on longitudinal or transverse Young's modulus;
2. The shear modulus is positively affected by the ply orientation and reaches its maximum at a ply orientation of 45°;
3. Increasing the thickness of the inner plies, will have a greater positive effect on the transverse Young's modulus and a more negative effect on the longitudinal Young's modulus;
4. Depending on the orientation of the plies, the shear modulus can be positively affected by the thickness of the inner plies;

In the literature it can be found that for maximizing bending and torsional stiffness a combination of 0° and ±45° plies need to be used [52, 53, 56]. Two designs have been found: $[0/\pm 45]_s$ laminate with $t_2 = 1.57t_1$ and a $[0/0/\pm 45]_s$ laminate with equal thickness. In Table 6.3 the options are compared. These values are obtained from entering the data in the MATLAB code. The initial ply values are still based on the IM-7/977–2 CFRP properties of Table 6.2.

Table 6.3 Mechanical properties of $[0/\pm 45]_s$ and $[0/0/\pm 45]_s$ laminates

Laminate	t_2/t_1	E_x	E_y	G_{xy}	ν_{xy}	ν_{yx}
	[-]	[GPa]	[GPa]	[GPa]	[-]	[-]
$[0/\pm 45]_s$	1.57	80.26	28.87	29.24	0.74	0.27
$[0/0/\pm 45]_s$	1	122.98	21.92	18.52	0.67	0.12

When comparing the most important mechanical properties for the design of the booms, namely E_x and E_y, there is a difference of 42.72 GPa and 6.95 GPa, respectively. Since the improvement of 42.77 GPa in E_x is much greater than in all the other properties, it can be concluded that the $[0/0/\pm 45]_s$ laminate would be the best option for to start with for further analysis. There is, however, an important note. This laminate stacking sequence is not final and the laminate can always be adjusted to improve the mechanical properties of the boom. This laminate can therefore be adjusted for each boom type. The final laminate stacking sequence per boom, can be found in chapters 7 and 8. Note that processes as vacuum-bagging, will be used to manufacture the booms, so carbon fiber prepregs are cut and shaped to fit a pre-designed mold of the relevant boom [57]. Prepregs are pre-impregnated composite fibers in which the polymer matrix material is already included [58]. After the baking process, the shaped CFRP tube or CTM boom will remain with the mechanical properties as calculated in this section.

The load cases have been defined, a proper boom length is determined and a preliminary laminate design has been performed. With these results, this chapter can be concluded. All the required information needed for a proper design process have been gathered. In the following two chapters the design process of the booms will be discussed.

Articulated Boom 7

Articulated booms have shown to be an ideal option for astrophysics missions. These mechanisms have a high stiffness and stability, and can be considered as reliable. The original design of the DST consisted of three articulated arms, made out of Invar. Nevertheless, the deployment ratio was relatively low and more important, the mechanism took almost up 20% of the total mass of the system. To reduce the mass and investigate options to increase the deployment ratio, an alternative articulated arm, based on the demonstration mission, is designed, as well as the hinges and the hold-down release mechanism (HDRM). In this chapter this design process is discussed.

7.1 Boom Design

In this section, the design steps of the CFRP boom segments of the articulated boom are explained. First the number of segments and hinges are determined, followed by the sizing of the boom segments.

7.1.1 Number of Segments and Hinges

The first important design parameter for the articulated boom, is the amount of segments and hinges used for the boom. As was discussed in chapter 2, the height of the SPS ring is chosen to be 60 cm. To extend the OEB 1.3 m from the primary mirror, a deployment ratio of at least 2.2 is required. The amount of hinges and segments need to be kept as low as possible, to keep the mass as low as possible and to reduce the amount of possible alignment errors. Therefore, the number of segments is chosen to be three. This is based on the deployment ratio and is rounded off to the next nearest integer. Since the OEB is only attached to a single arm, the position of the OEB in stowed configuration is not relevant. This would be relevant if, for example, two arms were connected to the OEB. The amount of hinges can be derived from the amount of segments. For this design, the amount of hinges is the amount of segments: one at the root, one between segment one and two, one between segment two and three. No extra hinge is needed at the OEB, as this box will be fixed to the third segment. An impression of the stowed configuration, with the segments and hinges, can be seen in Figure 7.1.

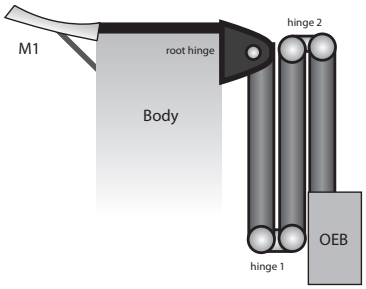

Figure 7.1 Impression of stowed articulated boom on downscaled design (not to scale)

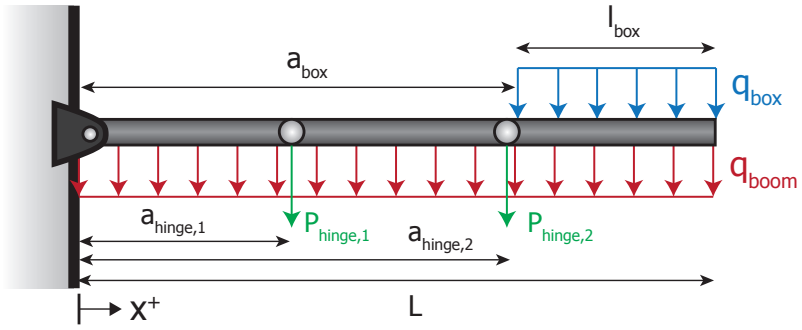

Figure 7.2 Articulated boom load case with correct amount of hinges (based on Figure 6.1a)

7.1.2 Sizing of Boom

The sizing of the boom is done according to the load case as described in chapter 6. In Figure 7.2 an updated version of Figure 6.1a can be found, including the amount of segments and hinges as determined in the previous subsection. The equations presented in this chapter have been used in a MATLAB code to find the optimal cross-sectional properties of the boom. This code can be found in section A.2. In is

short iteration process, where the outer boom diameter has an initial value of 1 cm and is increased until the deflections about both axes reach 15 µm. This deflection is calculated using Equation 6.4. Note that the deflection is calculated about both axes. The thickness is kept constant and a value of 1 mm is used assumed, to make sure the boom can be adhered or attached to the hinges. Sub-millimeter thickness is only required when the boom needs high elasticity, such as for the CTM case. This iteration is performed under milli-gravity condition, to make sure the design will withstand on-ground tests and production and still not be highly over-designed for micro-gravity conditions. The hinges are positioned (a_{hinge} in Figure 7.2) at one third and two third of the total boom length. The material properties are based on the $[0/0/\pm 45]_s$ CFRP ply of Table 6.3. The mass of the hinge is estimated to be 500 g. This is based on input from ADS, where a 200 g hinge is used for the deployment of solar panels. A more detailed mass prediction can be found later in this chapter. An overview of the input parameters of the code can be found in Table 7.1.

Table 7.1 Input parameters for the articulated boom MATLAB code

l_{boom}	l_{box}	t	$a_{hin,1}$	$a_{hin,2}$	m_{box}	m_{hin}	g	ρ	E
[m]	[m]	[m]	[m]	[m]	[kg]	[kg]	[m/s^2]	[kg/m^3]	[GPa]
1.3	0.3	$1{\cdot}10^{-3}$	0.43	0.87	3.2	0.5	$9.81{\cdot}10^{-3}$	1578	122.98

7.1.3 Overview

From the iteration process, as described in the previous subsection, the cross-sectional properties of the boom are obtained. In Table 7.2 these properties are presented and in Figure 7.3 a representation of the cross-section can be seen.

Table 7.2 Cross-sectional properties of articulated boom

d_{out}	d_{in}	t	I	m_{boom}	m_{seg}	δ_{max}
[cm]	[cm]	[cm]	[cm^4]	[g]	[g]	[µm]
3.3	3.1	$0.1{\cdot}10^{-3}$	1.29	206	68.7	13.9

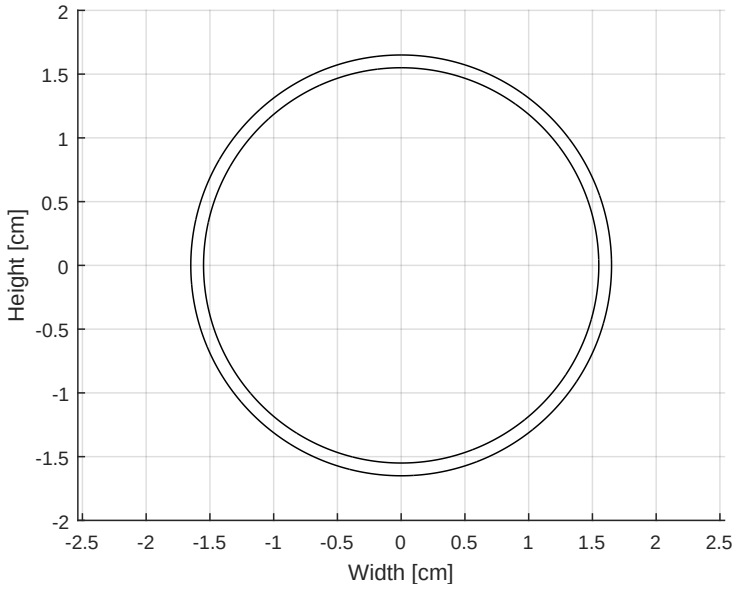

Figure 7.3 Cross-section of the articulated boom

The boom has an outer diameter of 3.3 cm with a thickness of 1 mm. This results in a boom with a total

mass of 206 g, so about 69 g per segment. Note that the mass of the real boom will slightly decrease as a continuous boom is assumed in this calculation.

Increasing the thickness of the boom allows the boom to have a smaller outer diameter and increases the moment of inertia, thus stiffness of the boom, however has a negative effect on the total mass of the boom. In order to show the effect of thickness on boom properties Figure 7.4 is used.

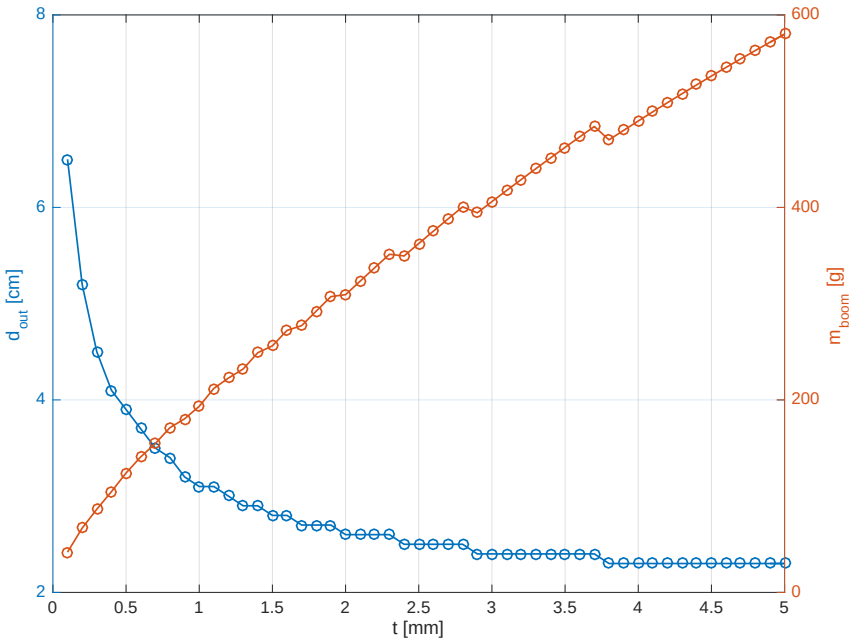

Figure 7.4 Effect of boom thickness on diameter and mass

The thickness is varied from 0.1 mm to 5 mm in discrete steps of 0.1 mm and for each thickness a corresponding required outer diameter is found with the iteration process. Due to the two iterations with discrete steps, both lines are not completely smooth, as they represent various cross-sectional configurations of the boom. The configurations have been indicated with dots. In Figure 7.4, it can clearly be seen that increasing the thickness will have a high impact on the mass of the boom. Therefore one wants to keep the thickness as low as possible, however the outer diameter should be balanced as well. For sub millimeter thicknesses high outer diameters are required. A thickness of 1 mm was chosen and from the figure it can be concluded that this was a reasonable value, as the required outer diameter is only 1.0 cm smaller than the limit the blue line starts to reach, which is 2.3 cm.

Using the values presented in Table 7.2, the hinges can be designed for the segments. In the next section the design process of these hinges are elaborated.

7.2 Hinge Design

In the previous section it was determined that three hinges will be used. These hinges are used to fold the boom segments. In this section the design of these hinges is presented. This design process consists of the sizing of the hinges and a torsional spring which is included in the hinges. Furthermore, the non-linear response of the hinges are discussed.

7.2.1 Sizing of Hinges

This hinge design is only conceptual and will be used to get a better estimation of the mass and to get a better impression of the deployable mechanism. A detailed design of the hinges will be made in a later phase of the DTS project, if the articulated boom shows to be the optimal boom design, and is not included in this thesis.

Hinge Shape A single segment needs to be connected to one or two hinges. To attach the segment to a hinge, it is determined that the hinge requires a tubular overlap with an outer diameter of 4 cm. The inner diameter of the overlap is close to the diameter of the segment of 3.3 cm, to allow a close-fit connection. This tubular overlap forms the base of the hinge. The hinges need to be designed such that during the stowed configuration the segments fit next to each other as parallel as possible (as shown in Figure 7.1). Therefore the hinges need to rotate about a center point at a certain distance from the vertical center axis of the tubular base. This is shown in Figure 7.5. This distance is determined to be 3.4 cm, to allow a gap of 2.8 cm between the two segments. This value has been determined based on an iteration process when designing the end stop of the hinges, which will be discussed in later in this subsection. The gap between the segments in stowed configuration has to be as small as possible, to enable a low stowage volume. Also the hinges will have less mass as they become smaller.

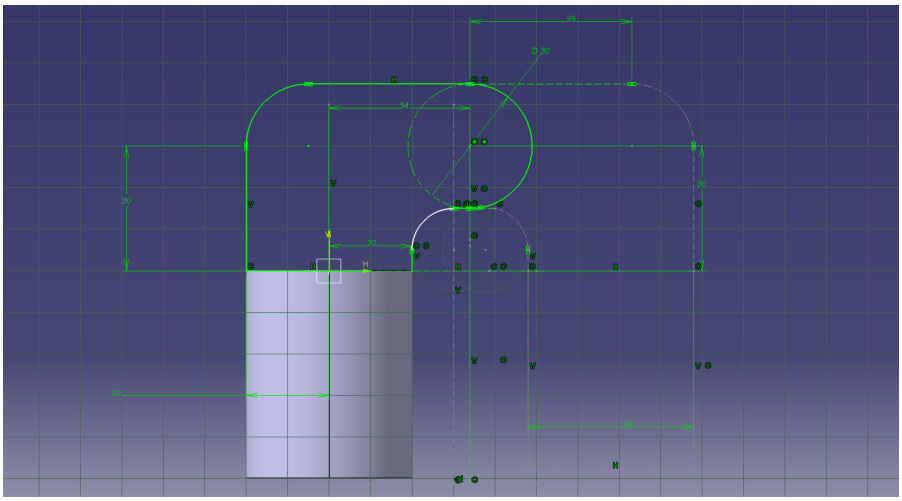

Figure 7.5 Sizing of the hinges

Hinge Elements To allow the hinge to rotate, the hinge requires an inner and an outer part. The outer part is designed to be hollow from the inside, so that the inner part is able to fit inside. Therefore the outer part has a larger width than the inner part. However, once the maximum angle is reached when deploying the hinge an end stop is required. To enable this end stop, the outer hinge part contains a small rod with a flat head and the inner part has a small plate, so that once the maximum angle has reached the rod will be pressed against the plate and further rotating motion is blocked. To connect these two hinge parts a bolt is used with a torsional spring coiled around the bolt and each end of the torsional spring is connected to the outer and inner part, respectively. In the following subsection, the spring design will be further elaborated. The design of the hinge, containing the elements as discussed above, is shown in Figure 7.6.

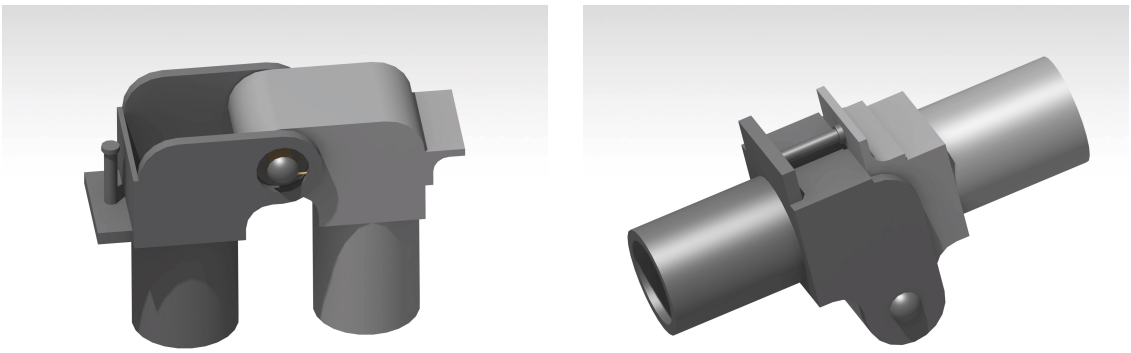

(a) Stowed view **(b)** Deployed view

Figure 7.6 Conceptual hinge design

Based on the experience of hinge designs of ADS, the material of the hinge elements, expect for the spring, is determined to be aluminum (7075.T6). The properties of this material can be found in Table 5.1. This resulted in total hinge mass of about 490 g, which is close to the 500 g, that was estimated for the MATLAB optimization code.

7.2.2 Spring Design

To enable the hinge to rotate and come back to the initial angle, a torsional spring is used inside the hinge. As was already mentioned, each leg of the torsional spring is connected to the inner or outer part of the hinge. As these parts rotate in opposite direction, the spring start to rotate as well. These parts however need a certain amount of force applied to them. This angular energy is stored in the spring, which the spring uses to push both parts back to the initial position [59]. Even though the spring is called a torsional spring, the spring is based on a bending moment. In Figure 7.7 a sketch of such a spring can be found.

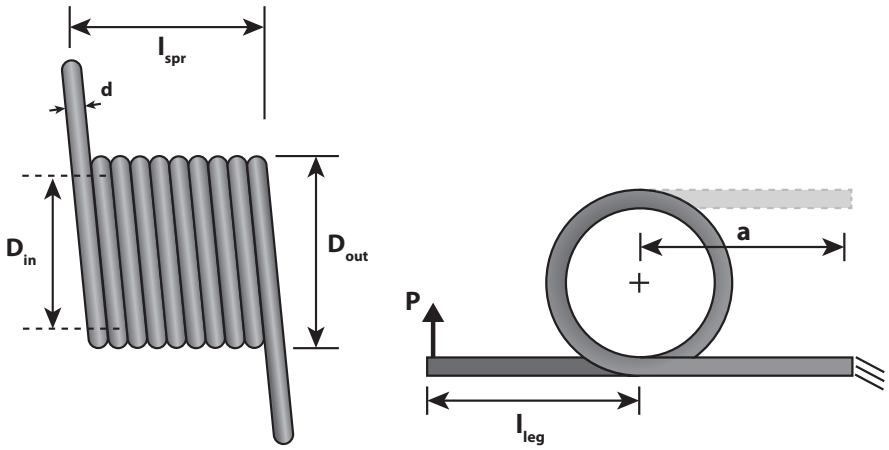

(a) Front view **(b)** Cross-sectional view

Figure 7.7 180˚ torsional spring with design parameters

The spring shown in Figure 7.7b is a 180˚ spring, which is required to allow the hinge to stow and deploy as shown in Figure 7.6. The bolt used between the two parts of the hinge has a diameter of 8 mm on the inside of the hinge. The torsional spring is coiled around this bolt, such that the spring is supported from the inside. To calculate the design parameters of the hinge, the following equations are used [60]:

$$P = \frac{\pi}{32}\frac{d^3}{l_{leg}}\sigma \tag{7.1}$$

$$\varphi = \frac{2D\pi n}{Ed}\sigma\frac{180}{\pi} \tag{7.2}$$

$$l_{spr} = n \cdot d \tag{7.3}$$

$$D = D_{in} + d \tag{7.4}$$

$$k = \frac{P}{\mathrm{d}\varphi} \tag{7.5}$$

Where P is the applied force on the legs in [N], d is the wire diameter in [m], l_{leg} is the length of the spring leg in [m], which is assumed to be equal to the moment arm a in Figure 7.7b, σ is the maximum tensile stress in [Pa], φ is the deflection angle of the leg in [˚], D is the mean coil diameter in [m], n is the number of active coils, E is the Young's modulus in [Pa], D_{in} is the inner diameter of the spring in [m], and k is the spring stiffness in [N/rad].

From the previous spring design it was already determined that D_{in} and l_{spr} are 8 mm and 4 cm, respectively. The thickness of spring was determined to be 4 mm. Using these values, D and n are determined to be 1.2 cm and 10, respectively. Rewriting Equation 7.5 with Equation 7.1 and Equation 7.2, results in

the following equation. Note that k is in [N/rad]:

$$k = \frac{d^4 E}{64 l_{leg} D n} \tag{7.6}$$

A common material type used for torsional springs is stainless steel [36, 61]. For space applications, it was already found in chapter 5 that 304L stainless steel is suitable. Therefore it is determined that this will be the material for this spring. This alloy is also confirmed to be used in other hinge designs [61].

Table 7.3 Initial spring design parameters

d	D_{in}	l_{leg}	l_{spr}	E
[mm]	[mm]	[mm]	[mm]	[GPa]
4	80	80	40	193

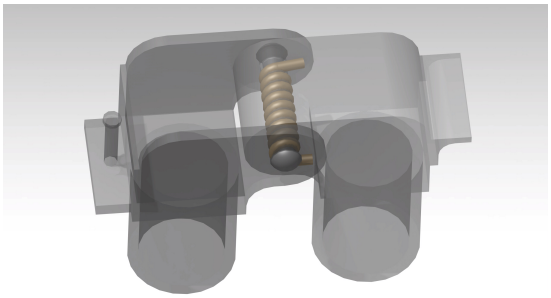

Figure 7.8 Location of spring in hinge design

For l_{leg} the distance from the center of the spring to the end of the tubular part of the hinge is assumed, which is 8 cm. Using the design parameters as given in Figure 7.3, the spring constant is determined to be 80.4 N/rad or 1.4 N/°. This means that a load of 1.4 N is required to rotate the spring a single degree. To stow the hinge, the spring needs to rotate 180°, which means that a force of about 253 N is required. In Figure 7.9 the situation is sketched of the spring deflection with respect to the total boom. The maximum angles the hinges can make to achieve the 15 µm limit are $\varphi_r = 0.2 \cdot 10^{-6}$ °, $\varphi_1 = 0.3 \cdot 10^{-6}$ °, and $\varphi_2 = 0.6 \cdot 10^{-6}$ °. The smallest angle to be taken into account is the angle with respect from the root, thus φ_r. As these angles are sub micro degree level, the load achieve the maximum deflection is also sub micro Newton. Therefore it can be concluded that the hinges should be locked. If stiffer the hinges are designed to be stiffer, a higher load is required to stow the hinges, resulting in more internal energy to be released, which means a higher end shock will happen if not enough damping is provided.

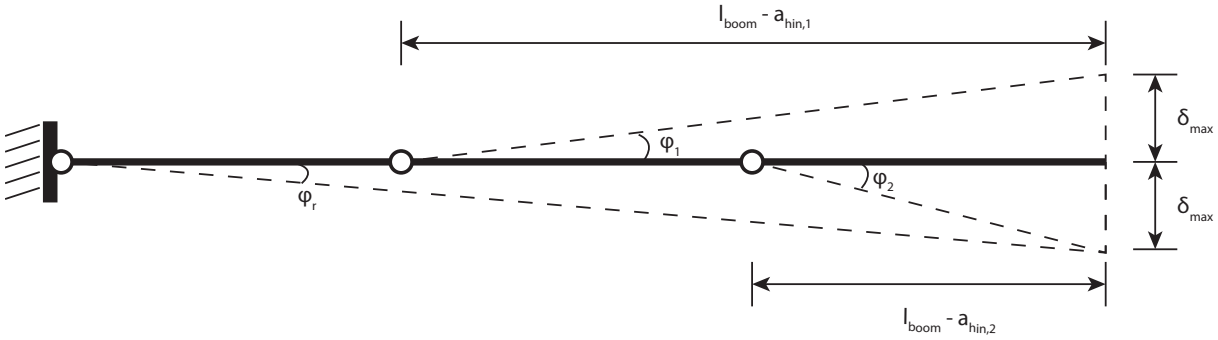

Figure 7.9 Maximum hinge deflection diagram

With this, the hinge and spring design is concluded. The location of the spring in the hinge is shown in Figure 7.8. In the following subsection the behavior of the hinge is discussed.

7.2.3 Non-linear Response

Hinges do often not response linearly. This has to do with the fact that if a hinge is in a tension-compression load cycling, it can experience three non-linear load-displacement responses. These responses are freeplay, non-linear elasticity, and hysteresis and can be seen in Figure 7.10 [62].

For hinges, freeplay is a typical response, as the hinge includes a clearance in order for the hinge to

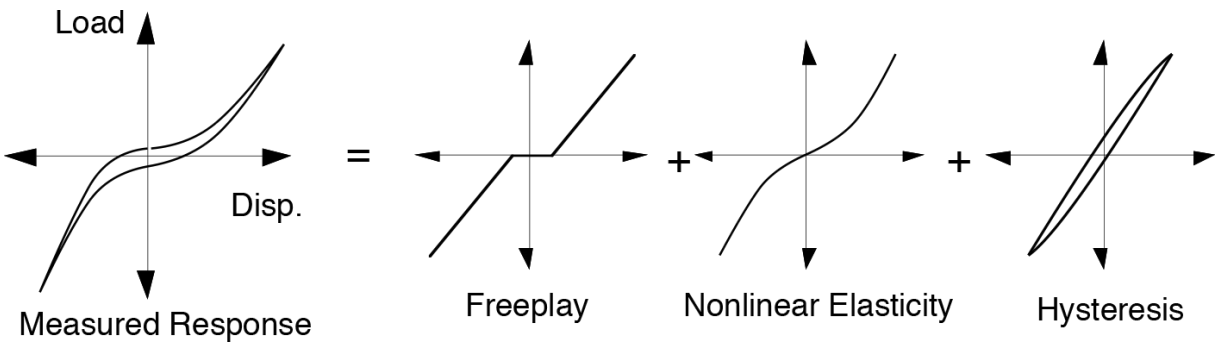

Figure 7.10 Non-linear behavior of mechanical joints [62]

articulate. As can be seen from Figure 7.10, there is a certain domain of which displacement occurs without applying any force. Non-linear elasticity can occur due to the internal load paths when the hinge or joint is in tension and compression. Also, the more surface contact between the mechanical interfaces is present, the more non-linear elasticity can be present. Hysteresis occurs due the tension-compression load cycling and is history dependent.

In order to minimize this non-linear elasticity and the freeplay, mechanical preload is often applied with a preload device. This device makes sure that a uni-axial compression load is applied in the primary direction of the load paths of the hinge or joint. Nevertheless, applying preload does not always guarantee extra stability for optical-precision applications. Sometimes it can actually reduce the freeplay and non-linear elasticity, but increase the hysteresis. Therefore, careful research have to be done on how the chosen preload device will increase the hysteresis of the system.

Although, preloading is a good solution for deployable mechanisms, as backlash can be recovered, the mechanism can be used more often, so has a better repeatability, and reducing all the non-linear responses will finally lead to having a much better deployment accuracy [17, 62].

7.3 Articulated Boom Mechanism

Combining the boom design and the hinge design, which were performed in the previous sections, results in the full articulated boom mechanism as shown in Figure 7.11.

7.3.1 Additional Components

During the stowed configuration (Figure 7.11a), the mechanism will be locked to the body of the instrument. This will be locked with non-explosive HDRMs. At least two HDRMs are required, as there are hinges at the top and at the bottom of the mechanism. Such HDRMs are available on the market, and is not needed to be designed separately. ADS has used the Non-Explosive Low Shock (NELS) on their recently developed articulated deployment system. This HDRM has a mass of 600 g without the outer shell [63, 64]. Nevertheless, for this design this HDRM would be over-designed and therefore smaller options need to be considered in the future. The assumption can be made that the required HDRM would have a mass of about 200 g, based on other projects of ADS, and off-the-shelf HDRMs such as the HDRM Series 06 by Glenair [65].

During the deployment of the boom, the HDRMs are released, which allow the hinges to release the stored angular energy. If this motion is not damped the hinges will return to the initial position with a high angular velocity, due to its stiffness, and will cause high shocks on the mechanism. These shocks are able to damage the mechanism, and therefore a damping mechanism is required. A low-mass and cost-effective solution would be to attach a cable from the root, along the booms, to each hinge. This cable will damp out the motion. This is an option to consider during a detailed design phase, if the articulated

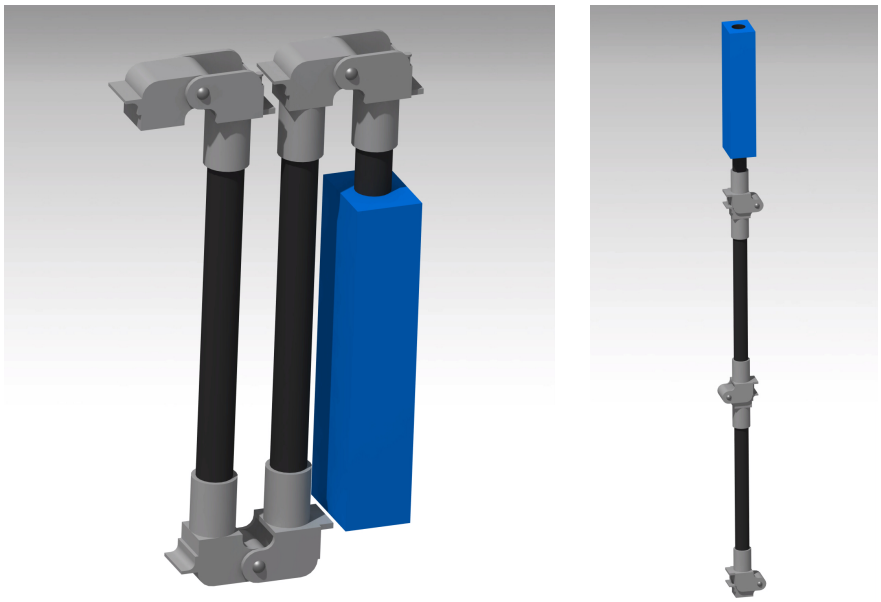

(a) Stowed configuration

(b) Deployed configuration

Figure 7.11 Design overview of articulated boom mechanism

boom shows to be the optimal boom for this mission. Nevertheless, the mass of such a damping cable can be neglected at this point.

7.3.2 Mass and Volume Estimation

In Table 7.4 the mass estimation of the articulated boom can be found. As this design is only conceptual and more components will be added trough the detailed design process, a contingency of 20% is assumed. This value based on agreements between the DST project group and ADS. The mass of the damping system is assumed to be included in this contingency factor. Adding this contingency to the mass of the designed components, resulted in a total estimated mass of 2460 kg. Reflecting this mass with requirement *R-M2D-DS-GEN-3*, this estimated mass does fulfill the requirement.

The mechanism has a stowed height, width, and depth of 48.5 cm, 21 cm, and 6 cm, respectively, which is a total stowed volume of 6111 cm^3. As the mechanism has a deployed length of 1.3 m and a stowed length of 48.5 cm, the deployment ratio is determined to be approximately 2.7. This value is typical for articulated booms, based on the results of chapter 4.

Table 7.4 Mass estimation of articulated boom

Component	Mass	Amount	Total Mass
	[g]	[-]	[g]
Boom segment	60	3	180
Hinge	490	3	1470
HDRM	200	2	400
Subtotal			**2050**
Contingency (20%)			410
Total			**2460**

7.3.3 Conclusion

This chapter has shown the design process of an individual articulated boom mechanism, for the down-scaled design of the DST. The boom consists of three CFRP tubular segments, with hinges at the root and two in the middle. At the end of the boom the OEB will be attached, which has a tight alignment budget with respect to the primary mirror (see chapter 2). To prevent the boom to exceed the alignment budget, it has been determined that the hinges would require an end-stop and a lock. Furthermore a torsional spring is used inside the hinges. If this boom type shows to be the most suitable boom for the DST mission, a more detailed design of the hinges is required.

In the original design of the DST, a structure of three articulated booms was used with a mass of 4.8 kg per articulated boom. In this mass estimation the hinge design was not included and the segments of the articulated booms were made out of Invar. After detailed material analysis in chapter 5 and the design process as shown in this chapter, a conceptual articulated boom mechanism has been designed with a total mass estimation of 2.46 kg, including three hinges. This is a reduction of almost 2.3 kg, which is a significant amount. This reduction would be even more if the mass of the hinges were included in the initial full system design.

7.4 Risk Analysis

Next to the structural and deployment performances of the articulated boom and the CTM boom, the risks of both booms play an important role in the final trade-off, which will be performed in chapter 10. In this section the approach of the risk analysis for both booms is explained, and a the potential risks of the articulated boom mechanism is presented. Furthermore the mitigation process of these risks is discussed.

7.4.1 Approach

The first step in the risk analysis process is to identify the risks. These risks are listed and each risk gets a label. The next step is to assess the risks. This implies that the risks will be examined on their likelihood and the consequence. Both the likelihood and the consequence have scores from 1 to 5. In Table 7.5 and Table 7.6 the scores and their descriptions of the likelihood and consequence are shown.

Table 7.5 Description of likelihood scores [66]

Score	Likelihood	Description
1	Rare	Very unlikely to occur, however there is still a tiny possibility.
2	Unlikely	Not expected to occur. Possibility of occurrence is a bit higher.
3	Possible	There is a moderate possibility of the event to occur.
4	Likely	There is a high possibility of the event to occur.
5	Almost Certain	It is expected that the event is very likely to occur.

Each risk will be assessed with these scores. Once this assessment is complete the risks are put into a risk map, which is a graphical overview of the risks, and the colored code gives an indication whether a certain action is required if the risks are too critical or not. After the risk map process, the final step is to identify potential risk mitigation options. These are especially required for the unacceptable and higher risks.

Table 7.6 Description of consequence scores [66]

Score	Consequence	Description
1	Insignificant	Negligible effect on optical performance.
2	Minor	Optical performance affected, but can be easily corrected.
3	Moderate	Optical performance moderate affected. Attempts can be made to correct images.
4	Major	Optical performance highly affected, no corrections possible.
5	Catastrophic	Full loss of optical performance.

7.4.2 List of Risks

In Table 7.7 potential risks of the articulated boom mechanism have been listed. These risks are based on the articulated boom which is designed in this chapter. In a later stage of the detailed design process of the DST project, this list needs to be updated continuously.

Table 7.7 List of potential risk for the articulated boom mechanism

Code	Risk	Likelihood	Consequence
RI-ART-01	Complete failure of one hinge or more.	2	5
RI-ART-02	Locking failure of single hinge after deployment.	2	2
RI-ART-03	Locking failure of two hinges or more after deployment.	1	2
RI-ART-04	Failure of spring in hinges during deployment.	1	5
RI-ART-05	One or both HDRMs not released.	1	5
RI-ART-06	Clamping failure of root hinge.	4	2
RI-ART-07	Failure of damping cable during deployment.	1	4
RI-ART-08	Fiber damage in CFRP material.	1	1
RI-ART-09	Thermal expansion of mechanism exceeds alignment requirements.	3	4
RI-ART-10	Connection between segments and hinges affected by thermal effects.	4	2
RI-ART-11	Collision of mechanism with space debris.	1	5
RI-ART-12	Deformations in mechanism due to unforeseen factors.	2	2
RI-ART-13	Mechanism starts to oscillate on natural frequency.	1	3
RI-ART-14	Stowed mechanism fails during launch conditions.	2	5

7.4.3 Risk Map

The risks which were presented in Table 7.7 were put into a risk map and the resulting risk map is shown in Figure 7.12. The legend of the color code of the risk map is presented at the bottom of Figure 7.12. What can be noticed is that no 'not acceptable' risks are identified. This can be explained with the fact that during the design process, potential risks were continuously identified and mitigated along the way. Nevertheless, the current design still has six undesirable risks. The mitigation process of these risks are discussed in the next subsection.

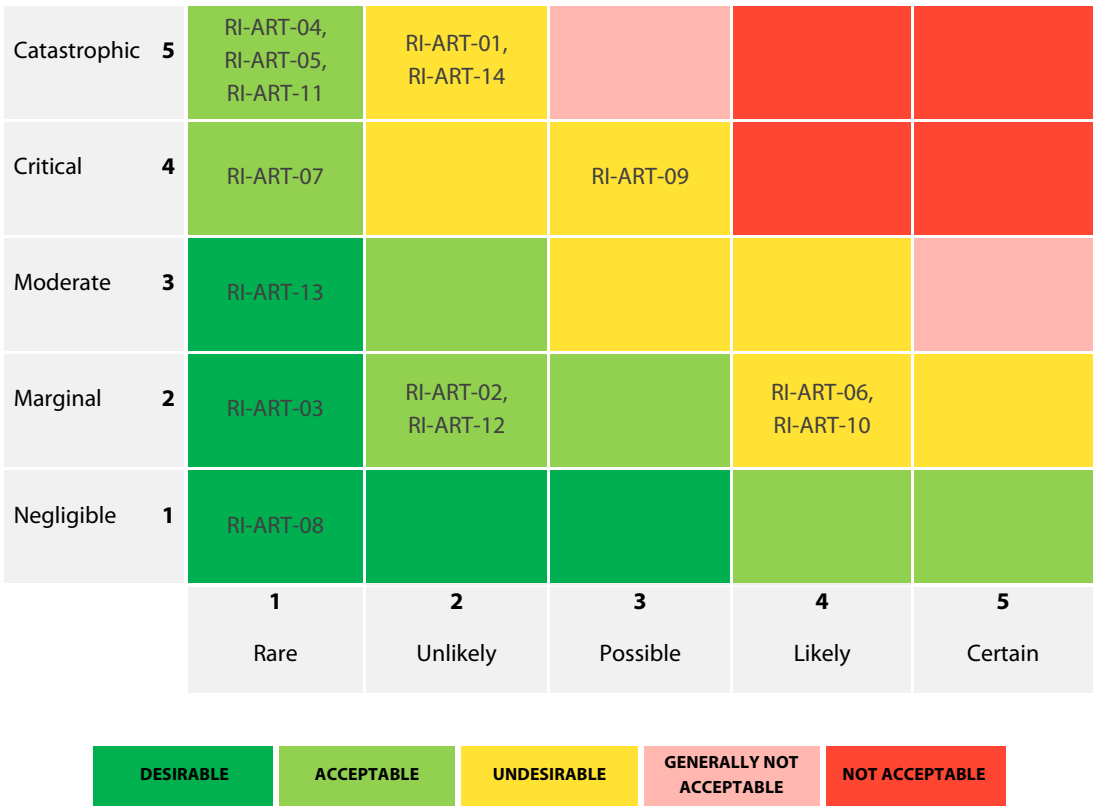

Figure 7.12 Articulated boom risk map

7.4.4 Risk Mitigation

For the risks which fall in the 'undesirable' to 'not acceptable zone' of the risk map, actions are required. Five risks were identified to be undesirable. All these risks have to do with the current status of the hinge design and the thermal effects on total mechanism. To mitigate these risks a more detailed design of the currently conceptual hinges is required. Also a full thermal analysis of such a system is required to find the bottlenecks in the design. In this report a preliminary thermal analysis is performed, however this would not be enough to mitigate all these risks. Nevertheless, most of these risks cannot be fully mitigated as there always is a possibility for them to occur. The consequences will remain more or less the same, however the likelihood of the risks can be shifted to left, which will make the risks more acceptable.

CTM Boom 8

The second deployable boom used for this research is the CTM boom. A CTM boom can be considered as two halves with an Omega-like cross-section, which are bonded together. Over the last years, a lot of research has been performed over this type of boom. In this chapter the design process of the boom itself is shown, as well of its HDRM. Furthermore, an overview is provided containing the main characteristics of the boom. This chapter is concluded with a risk analysis of this deployable boom concept.

8.1 Boom Design

This section will present the full design of the CTM boom specifically designed for the DST project. As the CTM boom is not a common type of boom, an impression of such a boom is given in Figure 8.1. The CTM boom in Figure 8.1 is a recently developed ultra lightweight CTM boom by DLR and ESA.

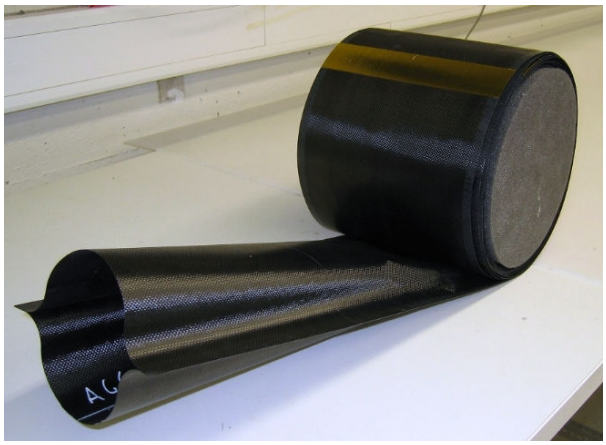

Figure 8.1 DLR/ESA's CFRP CTM boom [67]

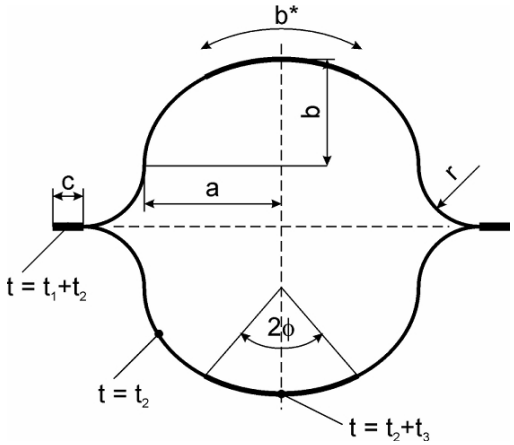

Figure 8.2 Cross-sectional view of CTM boom [68]

8.1.1 Design Parameters and Equations

The cross-section of a CTM boom has two axes of symmetry, as can be seen in Figure 8.2. Therefore a CTM boom can be fully designed by only designing a quarter of the boom. This is shown in Figure 8.3.

The quarter of the boom consist of two curves with radius r_1 and r_2, and a flat part. From this point there are eleven variables to define the cross-sectional shape of a CTM boom: x, y, $x_{0,1}$, $y_{0,1}$, x_1, $x_{0,2}$, $y_{0,2}$, x_2, x_3, r_1, and r_2. To reduce the amount of variables, some assumptions are made:

1. The center of the first curve starts on the y-axis so $x_{0,1} = 0$;
2. The shape should touch the x-axis at x_2, so the center of the second curve is vertically aligned with x_2, which means that $x_{0,2} = x_2$;
3. At x_1 the two curves overlap, which means that the curves should be tangent, so $(dy_1/dx_1)_{x_1} = (dy_2/dx_2)_{x_1}$;
4. Also at x_1 the y-coordinates of both curves should be equal, therefore $(y_1)_{x_1} = (y_2)_{x_1}$.

Applying the boundary conditions, simplifying the equations using the above mentioned assumptions, and using the standard equation for circular arcs $(x - x_{0,i})^2 + (y - y_{0,i})^2 = r_i^2$, one can describe the quarter

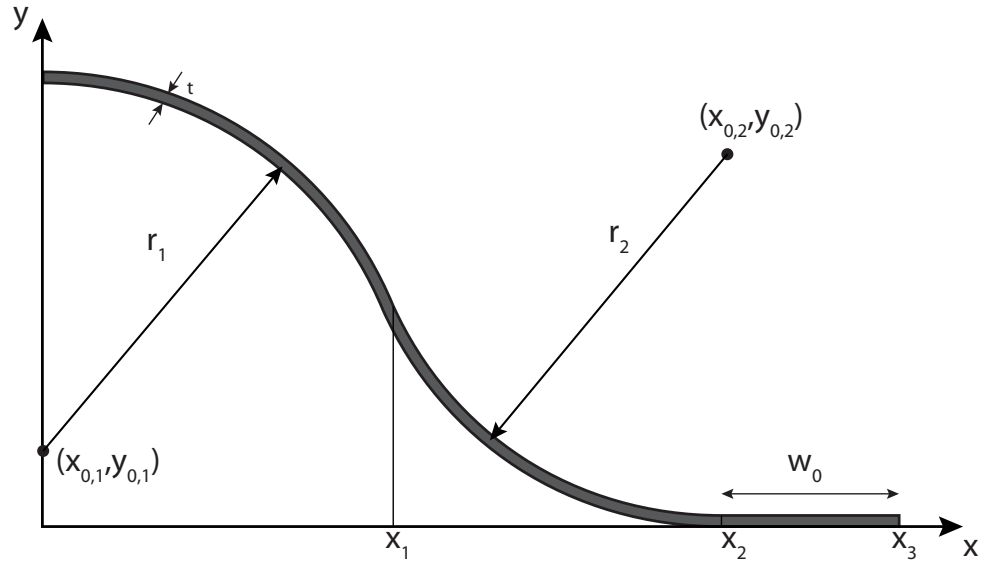

Figure 8.3 Quarter of a CTM boom with design parameters

of the boom with the following three equations:

$$y(x) = \sqrt{r_1^2 - x^2} - \sqrt{r_1^2 - x_1^2} - \sqrt{r_2^2 - x_1^2} + r_2, \qquad \text{for } [0 \le x \le x_1] \tag{8.1}$$

$$y(x) = -\sqrt{r_2^2 - (x - x_2)^2} + r_2, \qquad \text{for } [x_1 \le x \le x_2] \tag{8.2}$$

$$y(x) = 0, \qquad \text{for } [x_2 \le x \le x_3] \tag{8.3}$$

x_1 could be rewritten as a function of x_2, r_1, and r_1, so the function would be $x_1 = x_2/(1 + r_2/r_1)$. For the ease of manufacturing and to further reduce the amount of input parameters, it is assumed that $r_1 = r_2 = r$. From this point the only required input parameters for generating the cross-section for the boom are: r, x_2, and w_0 (which is the distance between x_2 and x_3). All variables are in [m].

8.1.2 Cross-sectional Properties

Once the shape of the boom is defined, other cross-sectional properties can be calculated, such as the moment of inertia about both axes (I_{xx} and I_{yy}) , the torsional constant (J), and the dimensions of the boom in deployed and stowed state.

Moment of inertia The equations for the moment of inertia have been derived by Hakkak and Khoddam [69]. This resulted in the following equations:

$$I_{xx} = 4t\left(\int_0^{x_1} r_1 \frac{\left(\sqrt{r_1^2 - x^2} + y_{0,1}\right)^2}{\sqrt{r_1^2 - x^2}}\mathrm{d}x + \int_{x_1}^{x_2} r_2 \frac{\left(-\sqrt{r_2^2 - (x - x_2)^2} + y_{0,2}\right)^2}{\sqrt{r_2^2 - (x - x_2)^2}}\mathrm{d}x\right) \tag{8.4}$$

$$I_{yy} = 4t\left(\int_0^{x_1} r_1 \frac{x^2}{\sqrt{r_1^2 - x^2}}\mathrm{d}x + \int_{x_1}^{x_2} r_2 \frac{x^2}{\sqrt{r_2^2 - (x - x_2)^2}}\mathrm{d}x + \beta \int_{x_2}^{x_3} x^2 \mathrm{d}x\right) \tag{8.5}$$

Where β is the parameter that is related to the thickness of the flange, and I_{xx} and I_{yy} are the moment of inertias about the x and y axis, respectively, in [m^4]. Normally β would be just 4, but this can become

less than four, depending on the flange thickness after joining. The equation for β is:

$$\beta = 2\frac{t_{join}}{t} \tag{8.6}$$

Where t_{join} is the total edge thickness after joining.

Torsional Constant As the boom can be considered as a thin-walled hollow tube, the torsional constant is derived from the equation:

$$J = \frac{4A^2}{\oint \frac{\mathrm{d}s}{t}} \tag{8.7}$$

Which result in [69]:

$$J = \frac{16t\left(\int_0^{x_1}\left(\sqrt{(r_1^2 - x^2)} + y_{0,1}\right)\mathrm{d}x + \int_{x_1}^{x_2}\left(-\sqrt{(r_2^2 - (x-x_2)^2)} + y_{0,2}\right)\mathrm{d}x\right)^2}{\int_0^{x_1}\left(\frac{r_1}{\sqrt{(r_1^2 - x^2)}}\right)\mathrm{d}x + \int_{x_1}^{x_2}\left(\frac{r_2}{-\sqrt{(r_2^2 - (x-x_2)^2)}}\right)\mathrm{d}x} \tag{8.8}$$

Where J is the torsional constant in [m^4], A is the enclosed area in [m^2], s is the perimeter of the area in [m], and t is the thickness of the cross-section in [m].

Dimensions During deployed state the height and the width of the boom can be calculate as (assuming $t << r$):

$$h_{dep} = 2\left(y_{0,1} + r_1\right) \tag{8.9}$$

$$w_{dep} = 2x_3 \tag{8.10}$$

Once the boom is flattened, the width of the boom becomes larger than the deployed state. The height can be approximated with twice the thickness of each shell. The height and width of the flat boom are expressed as [70]:

$$h_{flat} = 2t \tag{8.11}$$

$$w_{flat} = 2\left(w_0 + (r_1 + r_2)\cos^{-1}\left(\frac{r_2 - y_{0,1}}{r_1 + r_2}\right)\right) \tag{8.12}$$

8.1.3 Shape Optimization

Now all the equations for a CTM boom are stated and derived, the cross-sectional shape can be designed, corresponding to the given requirements. The boom is designed for the lateral load case, as this load case has a significant impact on the deflection, compared to the longitudinal load case. A MATLAB code has been written (see section A.3 of Appendix A), including Equations 8.1 to 8.12, Equation 6.5, and Equation 6.11, to find the optimal shape for the maximum allowed deflection. In short, the first version of the MATLAB code was intended to calculate the shape parameters of the boom, calculate the moment of inertia about both axis, and use this to determine the maximum deflection of the boom under the given load case. Nevertheless, this required a trial and error process to find the correct shape of the boom to meet the deflection requirement. This trial and error process, however, has given more insight of the boundary conditions of the input parameters. With this knowledge, the MATLAB code was extended to determine the optimal boom design in terms of mass and deflection. In Figure 8.4 this process is shown in a flowchart.

For a given range of r_1, x_2 is varied from half of the smallest value of r_1 to double the value of r_1. This because x_2 cannot be larger than double the value of r_1 as $r_1 + r_2 = 2r$. For each configuration the boom properties, including the deflection about both axes are calculated. From this data, all configurations with a deflection of higher than 15 µm are filtered out. The deflections are calculated about the x and y-axis. The maximum deflection occurs about the axis with the lowest moment of inertia. In this case this is I_{xx}.

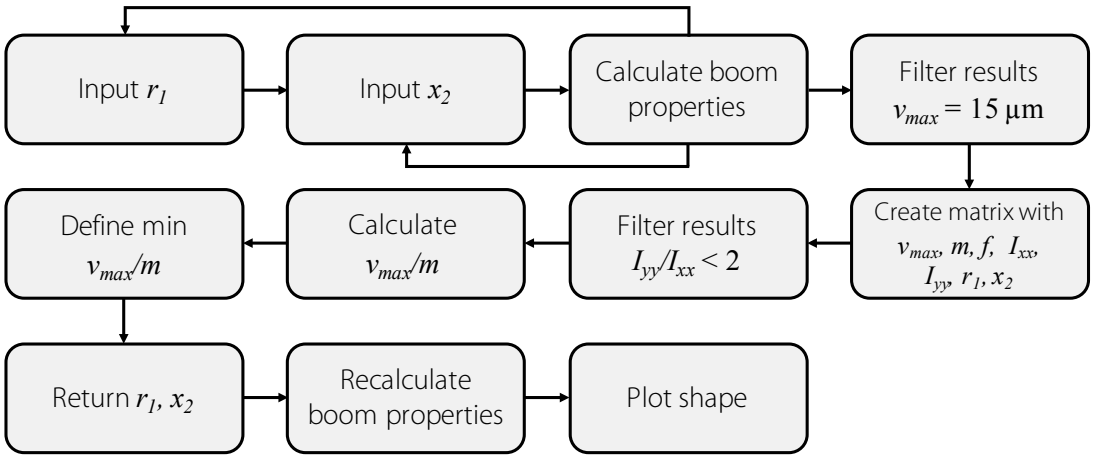

Figure 8.4 Flow chart of CTM boom optimization code

From this point a matrix is created for the different values of v_{max} with the corresponding values of m, f, I_{xx}, I_{yy}, r_1, r_1 and x_2. All results are filtered again, now for eliminating all boom designs at which I_{yy}/I_{xx} is larger than two. This is done to make sure that the boom will not have too large differences in performance about the two axis. Also if I_{yy} is more than the double of I_{xx} more material is needed to form the shape, which results in a higher mass. To find the optimal design based on deflection and mass, the relation between these two parameters has to be investigated. In Figure 8.5 these parameters are plotted against each other.

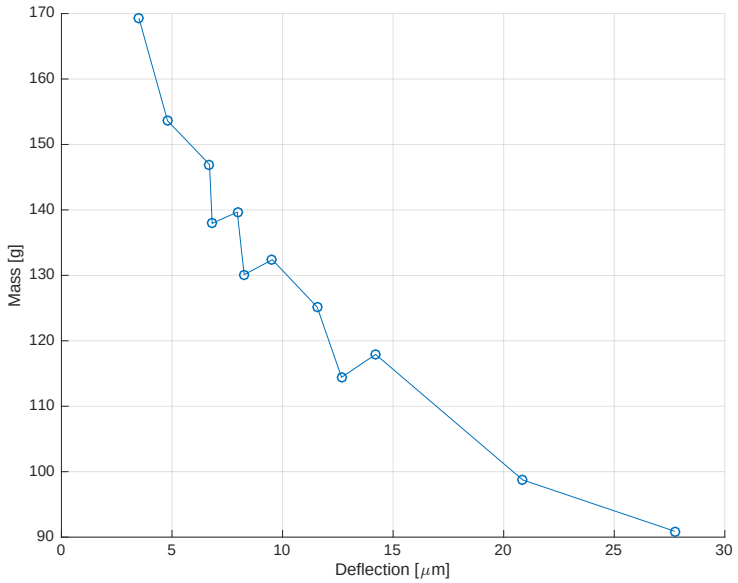

Figure 8.5 Deflection vs mass at 1 mili-g

The peaks in the graph are a result of the different combinations of r_1 and x_2 and have been sorted on deflection. The different combinations are indicated with dots. Despite of the peaks in the graph, it can clearly be seen that the mass and deflection have a quadratic or logarithmic relation. An important observation is that it is proven that if the mass boom decreases, the deflection, thus position accuracy, is negatively affected. To find an optimal design point, the minimum of v_{max}/m is chosen. Dividing these two parameters will tell which configuration has the lowest deflection per mass. With this rationale, it is determined that the corresponding configuration of r_1 and x_2 is the best option.

The values of r_1 and x_2 are returned, the boom properties are recalculated, and the shape of the boom is plotted. With this process, the most optimal boom has been found. A benefit of the code is that it can be used for other requirements as well. One just have to adjust the input parameters and set the boundary

conditions.

8.1.4 Boom Design and Properties

In Table 8.1 the input parameters of the current design are shown. These input parameters are almost the same as the ones used during the sizing of the articulated boom in chapter 7. To make sure the boom will not directly buckle under on-ground conditions (e.g. during testing), it is chosen to base the design on milli-gravity conditions, which means that the boom is 'over-designed'. However, if the boom would be designed for micro-gravity conditions, this could come in conflict with the manufacturability of the boom (small radii). Also the design will have a higher moment of inertia, which will provide more stiffness to the boom. The material properties originate from the $[0/0/\pm 45]_s$ laminate, which was discussed in chapter 6. As the fibers of the material are in the longitudinal direction of the boom, the highest Young's modulus of the material is used. The thickness t is based on earlier designed CTM booms, in which most booms had a thickness of about 0.3 mm. The radius r_1 (or r) is varied from 1 cm to 2 cm. These values were based on the earlier mentioned trial and error process.

Table 8.1 Input parameters for the CTM MATLAB code

l_{boom}	l_{box}	t	w_0	m_{box}	g	ρ	E
[m]	[m]	[m]	[m]	[kg]	[m/s^2]	[kg/m^3]	[GPa]
1.3	0.3	$0.3{\cdot}10^{-3}$	$5{\cdot}10^{-3}$	3.2	$9.81{\cdot}10^{-3}$	1578	122.98

With these input parameters, the shape of the boom is calculated. It was determined that $r_1 = r_2 = r = 1.6$ cm and $x_2 = 3.1$ cm. The optimal boom shape can be seen in Figure 8.6 and Table 8.2 gives the resulting boom properties.

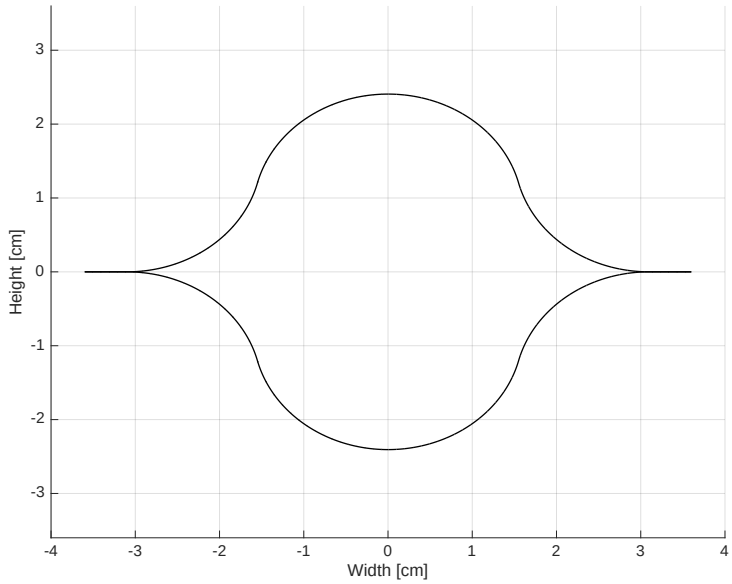

Figure 8.6 Cross-section design of the boom

Table 8.2 Cross-sectional properties of CTM boom

r	x_1	x_2	x_3	h_{dep}	w_{dep}	h_{flat}	w_{flat}	I_{xx}	I_{yy}	m_{boom}	δ_{max}
[cm]	[cm]	[cm]	[cm]	[cm]	[cm]	[cm]	[cm]	[cm^4]	[cm^4]	[g]	[µm]
1.6	1.55	3.1	3.6	4.9	7.2	0.06	9.2	1.12	2.21	145	14.2

The boom has a mass of about 145 gram and has a deployed height and width of 4.9 cm and 7.2 cm, respectively. When the boom is flattened the boom becomes wider and reaches a value of 9.2 cm. The thickness of the flattened boom is double the thickness, thus 0.6 mm. With these values, the sizing part of the boom itself is concluded. In the following section the sizing of the HDRM will be elaborated.

8.2 HDRM Design

The HDRM of a CTM boom allows the boom to deploy and retract about a central core. Furthermore, the HDRM provides stiffness and protection of the boom in stowed configuration. In deployed configuration the HDRM needs to clamp the boom at the root, providing stability to the boom itself. During the design phase of the boom, it was assumed that the root was clamped. Therefore, the amount of displacements possible at the root of the boom should be minimized, preferably bring it down to zero.

The HDRM consists of four main parts: a support for the boom, rollers, a storage drum, and an electric motor [70]. In Figure 8.7, the set-up of these parts is shown. Next to these parts, other structural elements are required, but this will not be treated in this section.

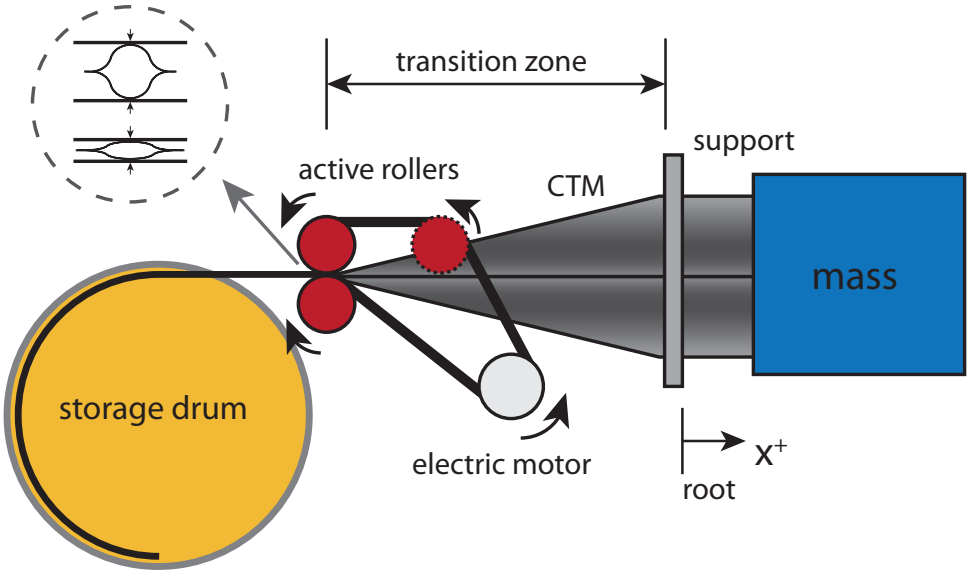

Figure 8.7 Schematic of the HDRM for a CTM boom

The design of this HDRM is conceptual, to get a more accurate mass and volume estimation of the total system. To achieve these estimations, each main component needs to be sized. The components shown in Figure 8.7 will be discussed from right to left.

8.2.1 Support

The support plate is required to provide the boom with the required stability. In Figure 8.8 a basic support plate can be seen. The plate consists of a hole with the same shape of the CTM boom. This shape, however, has an offset of 0.5 mm to make sure the boom is able to slide through the gap.

The challenge of designing this support is to allow the boom slide through the gap without damaging the boom due to friction. Also sharp edges could lead to damage. Simultaneously, the boom needs make sure that the boom is not able to rotate or move in the lateral direction of the boom. The only movement should be in the longitudinal direction of the boom. An option to clamp the boom is to split the support in two and use an extra spring mechanism to make sure the support clamps the boom once the boom reaches the required length. A disadvantage of such a mechanism is that the boom will not be able to correct in longitudinal direction, in other words being actively controlled. One could actively control this

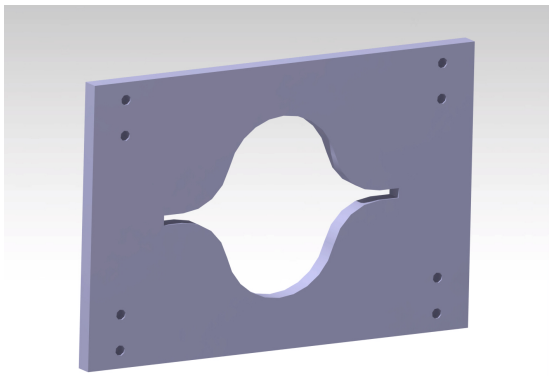

Figure 8.8 Basic support plate for HDRM of CTM boom

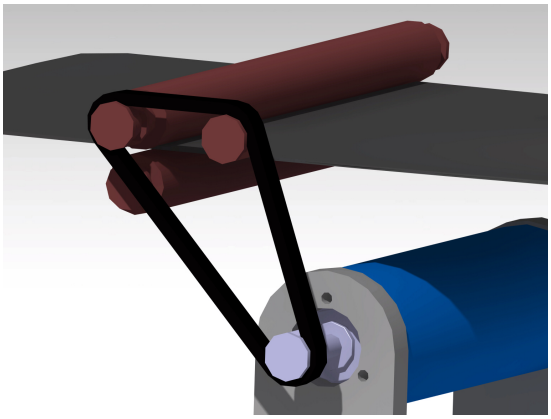

Figure 8.9 Roller system of the HDRM

opening and closing of the support, however this will make the mechanism more complex. One of the objectives was to keep the complexity of the boom as low as possible. If the CTM boom show to be the most optimal boom design for the DST telescope, this needs to be taken into account during the detailed design phase.

8.2.2 Rollers and Motor

The electric motor will be connected to the two top rollers. A belt is used for this connection. The most right roller in Figure 8.7 is actually considered as a pulley. It does not touch boom, but is rather connected to the outer case of the HDRM. This pulley will translate the motion of the belt for the top active roller. Only the top roller is required to be active. The other roller will automatically rotate in the opposed direction of the top roller. The rollers will make sure that the boom is flattened and rolled inside the storage drum. The flattening process of the boom is shown in the top left of Figure 8.7. The rollers will be made out of steel, to provide enough strength for the flattening process. In Figure 8.9 the rollers and the pulley are shown. To enable the rollers to flatten the boom the distance between the rollers is determined by adding twice the thickness of the boom, which is 0.6 mm. Based on the HDRM design of Chu and Lei, which had an approximate same design, the rollers are sized with a diameter of 1 cm [70].

8.2.3 Storage Drum

After the flattening process, the boom will be stored into a storage drum. To size this drum, the strain-limit of the CFRP material should be taken into account. To avoid fatigue damage accumulation in CFRP laminates, one must ensure that the strain-limit is set to approximately 0.4% [71]. This is based on practical experience in the aerospace industry. The inner diameter of this storage drum can be calculated using the following equation [72]:

$$D_{in} = \frac{t}{\varepsilon_{max}} \tag{8.13}$$

Where ε_{max} is the maximum strain. Using the thickness of 0.3 mm and a strain limit of 0.4%, results in an inner storage drum diameter of 7.5 cm.

The outer diameter of the storage drum, is dependent on the amount of coils the boom requires. When the boom is coiled, there is a possibility for local buckling. This is, however, not harmful for the boom itself, but should be taken into account when calculating the amount of coils required. Hence, a typical stacking factor of 1.1 is used [71]. This means that there will be a spacing of about 10% of the total flattened thickness (h_{flat}) between each coil. This would be 0.06 mm for this case. The outer diameter

of the roll can be calculated with Equation 8.14 and Equation 8.14.

$$D_{out} = 2\sqrt{\frac{l_{boom} k_{sf} h_{flat}}{\pi} + \frac{D_{in}^2}{4}} \tag{8.14}$$

$$n_{coil} = \frac{D_{out} - D_{in}}{2} \frac{1}{k_{sf} h_{flat}} \tag{8.15}$$

Where k_{sf} is the stacking factor. Using the values provided in this chapter, the outer diameter is found to be 8.2 cm, with a roll thickness of 0.35 cm and about 5 coils are required to fully retract the boom. The full design of the storage drum can be seen in Figure 8.10.

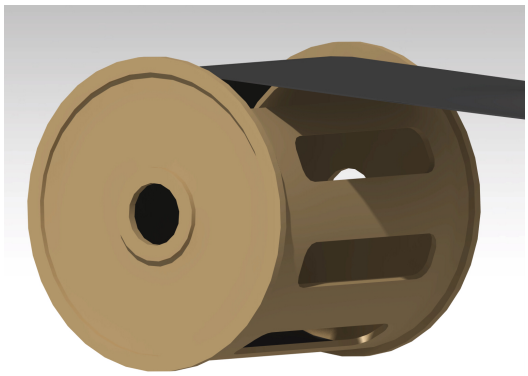

Figure 8.10 Storage drum of the CTM boom

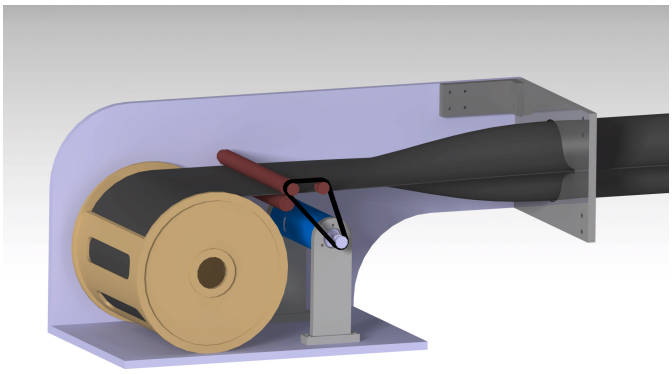

Figure 8.11 Early stage of the conceptual design of the HDRM

8.2.4 Case

To protect the components of the HDRM, an outer case is required. This case is also made out of aluminum. On the bottom plate, the electric motor and the storage drum are attached. The rollers and the support are connected to the side plates. To keep the mass as low as possible, the casing is designed to be as small as possible. The distance between the flat part and the full deployed part, is called the transition zone (see Figure 8.7). This transition zone is determined to be approximately 20 cm. This is based on an earlier optimization research of a similarly CTM boom [73]. Using the sizes of the previous sized components and the transition zone, the case is determined to have the following approximate dimensions: length of 31 cm, width of 12.5 cm, and height of 14 cm, resulting in a volume of about 5425 cm^3. An impression of the conceptual HDRM design can be seen in Figure 8.11.

8.3 CTM Boom Mechanism

The results of this sizing process have been combined and CAD drawings were made in CATIA, from which more accurate volume and mass estimations were obtained. In Figure 8.12 an impression of the total mechanism is given, both in stowed configuration and deployed configuration.

8.3.1 Mass and Volume Estimation

In Table 8.3, the mass properties of the total system can be found. What can be noticed is that the mass of the case is about 63% of the total mass of the HDRM system. Without the case, the mechanism would only have a mass of 945 g. However, this cannot be considered as realistic, as the components of the HDRM need to be attached to the case. Nevertheless, the shape, material, and required thickness can be optimized during a detailed design phase if this concept is chosen to be the most suitable boom design for the DST project.

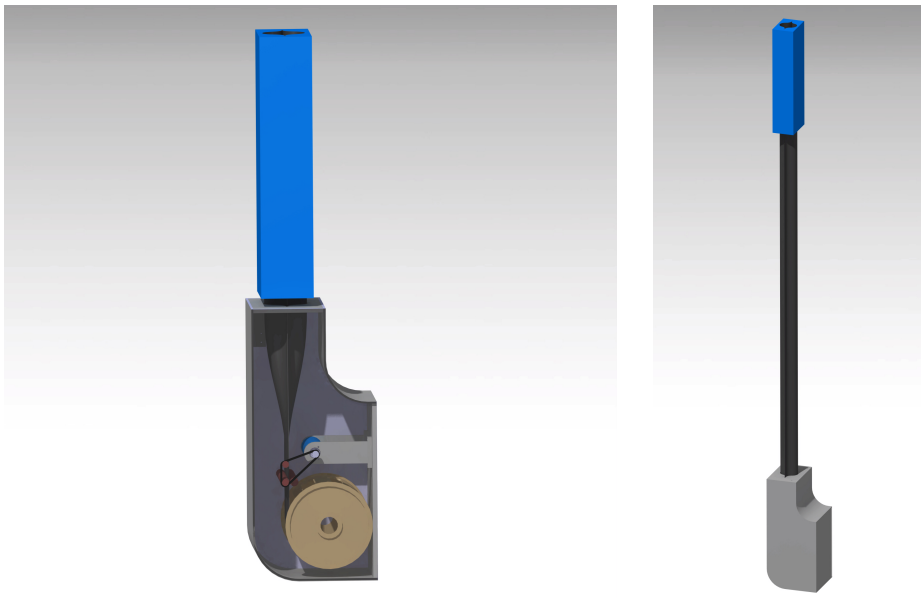

(a) Stowed configuration

(b) Deployed configuration

Figure 8.12 Design overview of articulated boom mechanism

Table 8.3 Overview of mass estimations for the CTM boom system

Component	Mass	Amount	Total Mass
	[g]	[-]	[g]
CTM boom	145	1	145
Support plate	100	1	100
Roller	70	2	140
Electric motor	500	1	500
Electric motor support	30	2	60
Case	1830	1	1830
Subtotal			**2775**
Contingency (20%)			555
Total			**3330**

The total mass is expected to be about 3.33 kg, including a contingency of 20%. Next to the mass, the system has a stowage volume of 5425 cm^3, which is identical to the volume of the case. The stowed length of the mechanism is 31 cm, so with a deployed length of 1.3 m, the deployment ratio of this mechanism is approximately 4.2. Note that the length of the OEB is not included in the calculation of the deployment ratio.

8.3.2 Conclusion

This chapter has shown the design process of a CTM boom including the design of its HDRM. The boom design has been optimized using an iterative process, which resulted in a CFRP boom mass of only 145 g. Nevertheless, to provide the required stiffness, stability and allow the boom to deploy and retract, a HDRM is required. This HDRM has an estimated mass of 1.95 kg, excluding the contingency of 20%.

This is 13 times higher than the mass of the boom itself. Therefore the HDRM is the bottleneck for mass constraints. Even though the high mass of the HDRM, this mechanism is able to provide controlled deployment, which is an important benefit of the mechanism.

8.4 Risk Analysis

This risk analysis was based on the same approach as the risk analysis performed in chapter 7 for the articulated boom. As the approach is already elaborated, this section only highlights the list of potential risks of the CTM boom mechanism, followed by the risk map and risk mitigation strategies.

8.4.1 List of Risks

In Table 8.4 potential risks of the CTM boom mechanism are shown. As was already mentioned in chapter 7, this list needs to be updated continuously.

Table 8.4 List of potential risk for the CTM boom mechanism

Code	Risk	Likelihood	Consequence
RI-CTM-01	Failure of the bottom roller during deployment.	1	3
RI-CTM-02	Failure of one of the active rollers during deployment.	1	5
RI-CTM-03	Failure of the electric motor during deployment.	2	5
RI-CTM-04	Failure of the belt between the rollers during deployment.	1	5
RI-CTM-05	CTM boom jams inside the HDRM.	2	4
RI-CTM-06	CTM boom deploys a few centimeters below the required deployment length.	2	5
RI-CTM-07	Buckling of the stowed boom inside the storage drum.	5	1
RI-CTM-08	Support plate shrinks due to thermal effects.	4	2
RI-CTM-09	CTM boom deforms permanently due to deployment and retraction.	3	2
RI-CTM-10	Thermal expansion of the boom exceeds the alignment requirements.	1	4
RI-CTM-11	Collision of the mechanism with space debris.	1	5
RI-CTM-12	Fiber damage in the CFRP material.	4	1
RI-CTM-13	Deformations in CTM boom due to unforeseen factors.	2	2
RI-CTM-14	Mechanism starts to oscillate on natural frequency.	1	3
RI-CTM-15	Stowed mechanism fails during launch conditions.	2	2

8.4.2 Risk Map

In Figure 8.13 the risks are shown in a risk map. Most of these risks are based on failures of individual components which are related to the deployment of the CTM boom. Once the boom is deployed, the amount of risks are significantly reduced.

8.4.3 Risk Mitigation

Five risks were identified as undesirable. Four these risks were involved during the deployment process of the boom. To mitigate these risks, the mechanism should be carefully tested under various conditions.

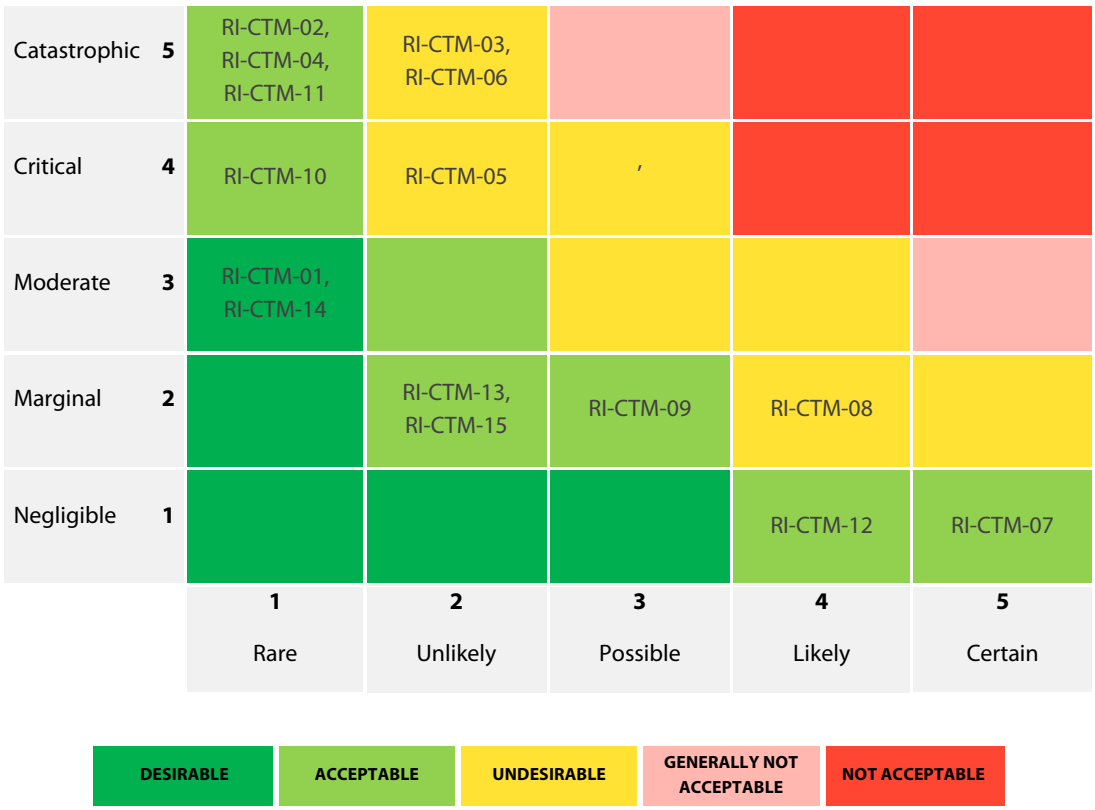

Figure 8.13 CTM boom risk map

These tests should be performed multiple times and issues with the mechanism should be solved in order to reduce the likelihood of these events. The remaining undesirable risk is *RI-CTM-08*, which implies that the support plate shrinks due to thermal effects. As the root of the boom is crucial for the stability and stiffness of the structure, more research need to be performed on the support plate. It has to be tested under various thermal conditions and alternative clamping options should be investigated to provide the reliability of the system. Furthermore, for critical components, such as the electric motor, redundancy can be added. Nevertheless, this will increase the mass of the system.

III

Analysis, Results & Comparison

Boom Analysis 9

This chapter will elaborate on the analyses performed on the two deployable boom designs made in the previous part of this report. First the methodology of the analyses is discussed, including the set-up of the software. Next, a thermal model is discussed, which predicts the incoming fluxes on the deployable booms. Finally, the analyses of each design are presented, containing static, modal, harmonic and thermal analyses.

9.1 Methodology

To enable reproducibility of this research, it is essential that the methodology of the analyses are clearly stated. The software used for the analyses is a finite-element method (FEM) tool, called ANSYS Mechanical. The version used is the 17.1 student version. This software allows the user to perform electromagnetic, structural, and thermal analyses. For this research only structural and thermal analyses are used. A crucial step in obtaining desirable results is to perform a correct set-up of the analysis settings. During the analysis process it was found that the following settings are the most critical: material, coordinate system, contacts, meshing, and boundary conditions. In each following subsection these settings will be further elaborated.

9.1.1 Material

ANSYS comes with a standard library of materials, however this library is editable so the user is able to modify the existing materials and add new materials to the list. CFRP is unfortunately not available in the default material list. Therefore, a new material was made containing the material properties of the $[0/0/\pm 45]_s$ CFRP laminate from chapter 6. The CTE of CFRP is not constant over the temperature spectrum. Confidential data from ADS was obtained for the CTE of a CFRP laminate and based on the given graphs, an approximation was made of the values for the tabular data in ANSYS. In Figure 9.1 the material properties in ANSYS can be seen.

	A	B	
1	Property	Value	
2	Density	1.6	g cm^-3
3	Isotropic Secant Coefficient of Thermal Expansion		
4	Coefficient of Thermal Expansion	Tabular	
5	Scale	1	
6	Offset	0	C^-1
7	Zero-Thermal-Strain Reference Temperature	20	C
8	Orthotropic Elasticity		
9	Young's Modulus X direction	1.2298E+11	Pa
10	Young's Modulus Y direction	2.192E+10	Pa
11	Young's Modulus Z direction	2.192E+10	Pa
12	Poisson's Ratio XY	0.67	
13	Poisson's Ratio YZ	0.12	
14	Poisson's Ratio XZ	0.12	
15	Shear Modulus XY	1.852E+10	Pa
16	Shear Modulus YZ	1.852E+10	Pa
17	Shear Modulus XZ	1.852E+10	Pa
18	Tensile Yield Strength	1.76E+09	Pa
19	Compressive Yield Strength	1.57E+09	Pa
20	Isotropic Thermal Conductivity	15	W m^-1 C^-1

(a) Mechanical and physical properties

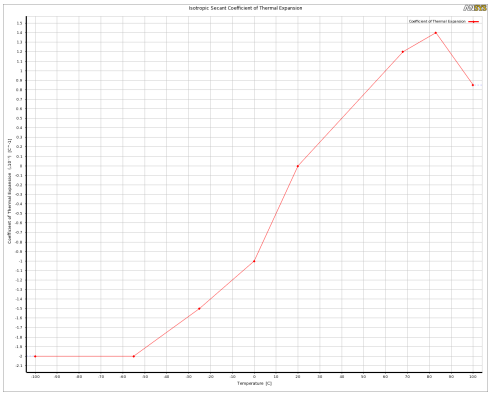

(b) CTE approximation

Figure 9.1 Material properties of CFRP material in ANSYS

9.1.2 Coordinate System

In Figure 9.1 it could be seen that two Young's moduli are present, each for a specific axis. If the coordinate system is not properly defined, the analysis of an orthotropic material can be drastically affected.

In the basic Workbench window of ANSYS, a default global coordinate system is given. This coordinate system, however, should not be used as default for the components. It has to be checked if the coordinate system matches the same local coordinate system of the laminate itself. If the coordinate system does not match with your part coordinate system, this is not critical as the values obtained will only belong to the different axis. Nevertheless if the coordinate system of the material does not match with the default global coordinate system, total different values will be obtained.

The effect of the coordinate system has been tested using a simple aluminum rod. The rod has a diameter of 10 cm, a length of 50 cm, and is treated as a cantilever beam. In the first analysis the default coordinate system is used to calculate the deflection under self-weight. This coordinate system implied that the y-axis is in the longitudinal direction of the beam. However, in the material coordinate system (see Figure 6.7) the x-axis is in the longitudinal direction of the material. Therefore, the wrong Young's modulus is used. This resulted in a deflection of 35.9 µm. Using a user-defined coordinate system with the correct orientation of all the axes, the correct deflection was obtained, with a value of 6.5 µm. As can be noticed, this has a significant impact on the result.

9.1.3 Contacts

Next to coordinate systems, contacts should be defined properly as well. This could be notices when analyzing both the articulated boom as well as the CTM boom. When loading a geometry in ANSYS Workbench, default contacts are generated. The contacts in the hinges of the articulated boom were causing wrong results when comparing them to analytical values. Multiple parameters have been changed to see if the results would improve, however no improvements were gained. Once the boom was made as a single solid part, the desired results were found.

For the CTM boom the contacts should only be between the flanges and the settings should be set to bonded. However, the default contacts generated for this boom included also contained contacts along the curves. This resulted in remarkable results, in which the boom deflected in an S-shape. This is shown in Figure 9.2a. After a parameter study, it was found that the contacts were the culprits. When changing the contacts only to the flanges, reliable results were obtained. This can be seen in Figure 9.2b. It is of high importance that the contacts are well set-up, else wrong results will be obtained. Therefore one should always validate the ANSYS values with analytical if possible.

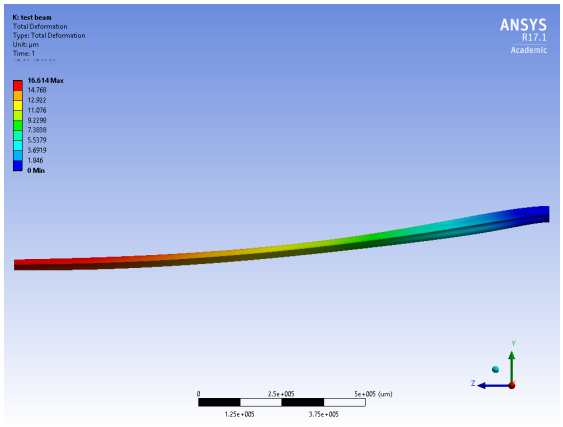

(a) Results of wrong contacts

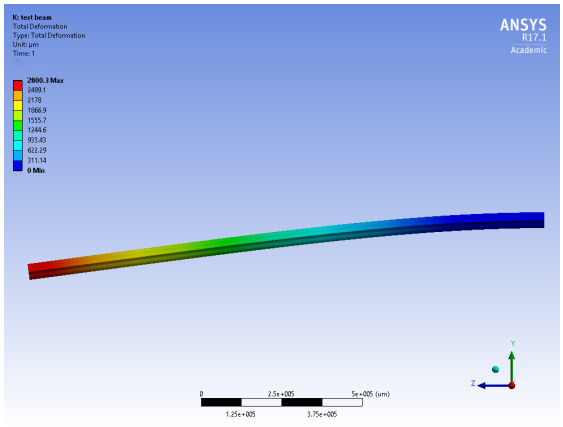

(b) Results of correct contacts

Figure 9.2 Errors due to wrong contacts in ANSYS

9.1.4 Meshing

In FEM, the geometry is split in smaller segments. This is called meshing. The student version of ANSYS limits the user to use 32,000 mesh nodes. For simple geometries, the number of meshes is not critical,

however once larger and more complex geometries are used, the mesh size becomes critical in obtaining accurate results. To stay within the mesh limits, the following settings are used:

1. Size Function: Adaptive
2. Relevance Center: Fine
3. Smoothing: High
4. Span Angle Center: Fine

This has proven to be the best settings, for achieving the smallest mesh size and also to prevent errors. Various different settings have been used, but lots of errors have shown to occur when using those settings for more complex shapes as CTM booms.

9.1.5 Boundary Conditions

The final set of settings are the boundary conditions. These settings define which parts of the geometry are allowed to move or rotate. In the default settings no boundary conditions are specified. As booms are treated as cantilevered beams, the only fixed part is the end of the boom, as it is assumed that the ends of the booms will be clamped by the root hinge of the articulated boom and the HDRM in the case of the CTM boom. The effects of clamping itself should be investigated through experimental research.

9.2 Thermal Environment

One of the analyses performed for this research, is the thermal analysis. To get an estimation of the fluxes obtained from the Sun and the Earth, a MATLAB script has been written. In this section the model is explained and the worst-case results are presented. The MATLAB code can be found in section A.4 of Appendix A. The equations presented in this section originate from the *Introduction to On-Orbit Thermal Environments* lecture by Rickman [74]. The model is also validated with the results found in this lecture.

9.2.1 Model

To model the incoming fluxes, an orbiting box is used and for each side of the box, these fluxes are calculated. In Figure 9.3 the situation is sketched. Note that side 6 is beneath side 5.

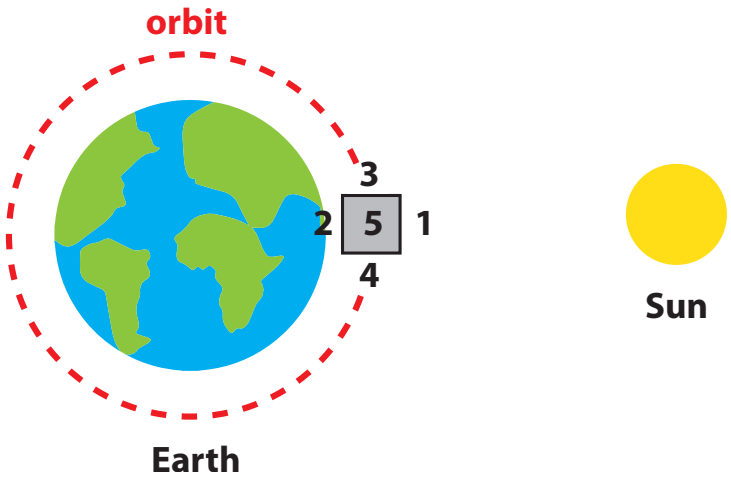

Figure 9.3 Situational sketch of orbiting box

The sides of the box are numbered from 1 to 6:

1. Sun facing side (Zenith);
2. Earth facing side (Nadir);
3. Velocity direction side;
4. Aft facing side;
5. West facing side;
6. East facing side.

Until now, no orbital analysis and design have been performed for both the DST mission and demonstration mission. However, the optical performance of DST has been based on an orbital altitude of 550 km [4]. In ideal case the telescope would also have an inclination of about 90°. For the calculations of the incoming fluxes, more parameters are required to get more accurate estimations. As these parameters are currently not available, it was determined to base the calculations on the worst case scenario. In the following subsection, the calculations and assumptions are further elaborated.

9.2.2 Incoming Fluxes

The incoming fluxes on the sides of the box can be categorized in the solar flux, albedo flux, and planetary flux.

Solar Flux The solar flux at the position of the box can be calculated using the following equation:

$$q_{sol} = \frac{q_{sc}}{\left(\frac{r_{ES} - (h + r_E)}{r_{AU}}\right)^2} \tag{9.1}$$

Where q_{sol} is the solar flux at the orbital height of the box in [W/m^2], q_{sc} is the solar constant in [W/m^2], which is the mean solar flux at a distance of 1 astronomical unit (AU), r_{ES} is the distance between Earth and Sun in [m], which varies of the true anomaly of the Earth's orbit about the Sun, h is the orbital altitude in [m], r_E is the Earth's radius in [m], and r_{AU} is 1 AU in [m].

As was mentioned, r_{ES} is dependent on the position of the Earth in its orbit around the Sun. It was chosen to base the analysis on the worst case scenario, therefore the Earth should be assumed to be in its closest position to the Sun, which is called the perihelion. At this point, the Earth is calculated to be at a distance of $1.471 \cdot 10^8$ km. Note that the model allows the user to change the value of the true anomaly.

Another assumption made is that the β-angle is zero. The β-angle is the angle between the solar vector and the orbital plane [74]. This angle varies per season and is dependent on the inclination and the perturbations of the orbit. However, the highest incoming fluxes will be obtained when this angle is zero.

Albedo Flux The albedo flux is based on the amount of energy of the Sun that is reflected by another planet. In this case this planet is the Earth. The albedo flux at the position of the box can be calculated with Equation 9.2.

$$q_{alb} = q_{sol} \alpha FF \cos \xi \tag{9.2}$$

Where q_{alb} is the albedo flux in [W/m^2], FF is the form factor (will be discussed in next subsection), α is the dimensionless albedo of the Earth and ξ is the solar zenith angle in [°] which can be calculated as:

$$\xi = \cos^{-1}(\cos\theta \cos\beta) \tag{9.3}$$

Where θ is the orbital angle in [°]. As it was assumed that β is zero, the solar zenith angle is equal to the orbital angle in this case.

Planetary Flux Next to the solar energy, the box receives emitted energy from the Earth itself as well. This can be calculated with the following equation:

$$q_{pla} = \frac{q_{sol}(1 - \alpha)}{4} FF \tag{9.4}$$

Where q_{pla} is the planetary flux in [W/m^2]. It is assumed that the Earth has a constant temperature over the total surface and therefore the planetary flux is assumed to be constant as well over the full surface of the Earth.

9.2.3 Effect of Box Orientation

Each side of the box will experience different values for the incoming fluxes. For example, side 1 only will receive a solar flux, while the dominating fluxes on side 2 will be the albedo flux and the planetary flux. The form factor FF, was already introduced in the previous subsection. This form factor characterize the orientation of the face to the planet. Only side 1 and side 2 are directly faced to the Earth of Sun. All other sides are perpendicular to the planet and will therefore have another form factor than side 1 and side 2. The form factor of side 1 and side 2, which can be labeled as the parallel form factor, can be calculated with Equation 9.5, while the perpendicular form factor can be calculated with Equation 9.6.

$$FF_{\parallel} = \left(\frac{r_E}{r_E + h}\right)^2 \tag{9.5}$$

$$FF_{\perp} = \frac{1}{2\pi}\left(\pi - 2\sin^{-1}\sqrt{1 - \left(\frac{r_E}{r_E + h}\right)^2} - \sin\left(2\sin^{-1}\sqrt{1 - \left(\frac{r_E}{r_E + h}\right)^2}\right)\right) \tag{9.6}$$

Next to the form factor, the angle of the face with the incoming flux per orbital angle must be taken into account as well. Depending on the position and orientation of the face, the incoming flux has to be multiplied with the sine or cosine of the orbital angle. This can be seen in the MATLAB code.

9.2.4 Results

Using equations 9.1 to 9.6, and taking into account the orientation of the sides with respect to the incoming fluxes, the incoming flux per side is obtained. In Table 9.1, the input parameters of the model are listed.

Table 9.1 Input parameters for the solar flux MATLAB code

h	r_e	q_{sc}	α	μ_E	β
[m]	[m]	[W/m^2]	[-]	[m^3/s^2]	[°]
$550{\cdot}10^3$	$6378.14{\cdot}10^3$	1367	0.3	$3.986{\cdot}10^{14}$	0

The resulting fluxes are presented in Figure 9.4. To simplify the case for the booms, it is assumed that the booms will only have incoming fluxes on the back and on the front of the geometry. This would mean that the fluxes have to be analyzed in pairs of side 1 and side 2, side 3 and side 4, and side 5 and side 6. If the mean absolute difference between the total fluxes are compared it can be concluded that the worst case scenario would be if the front and back of the booms were placed with the same orientation as side 3 and side 4. The mean absolute differences are about 390 W/m^2, 622 W/m^2, and 0 W/m^2, for side 1 and 2, side 3 and 4, and side 5 and 6, respectively. The data of the graphs shown in Figure 9.4 will be used in the thermal analysis parts of sections 9.3 and 9.4.

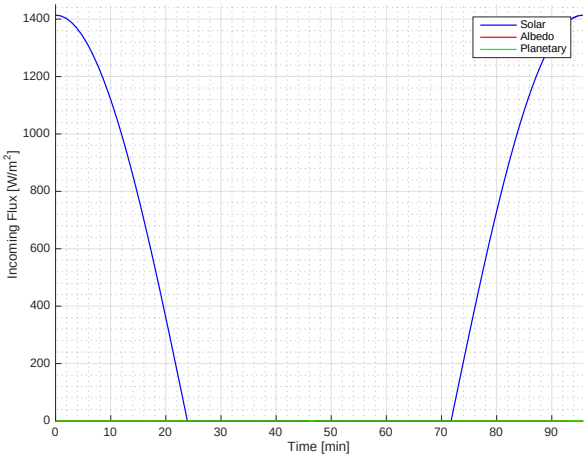

(a) Side 1: Sun facing

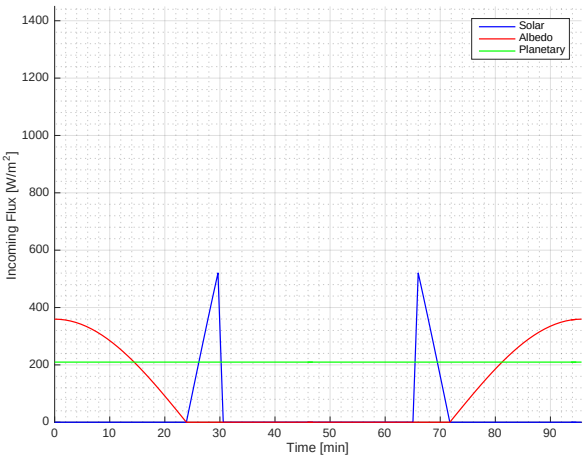

(b) Side 2: Earth facing

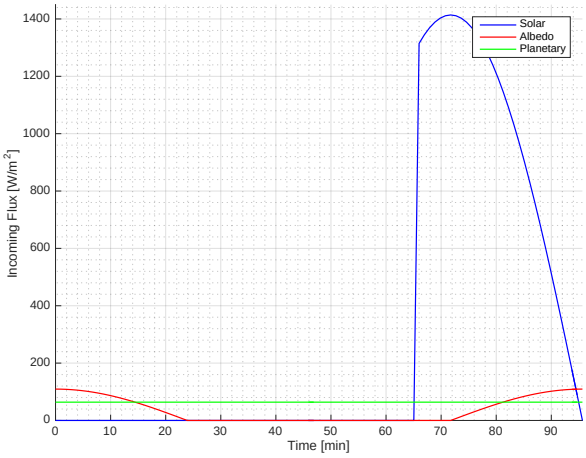

(c) Side 3: Velocity direction

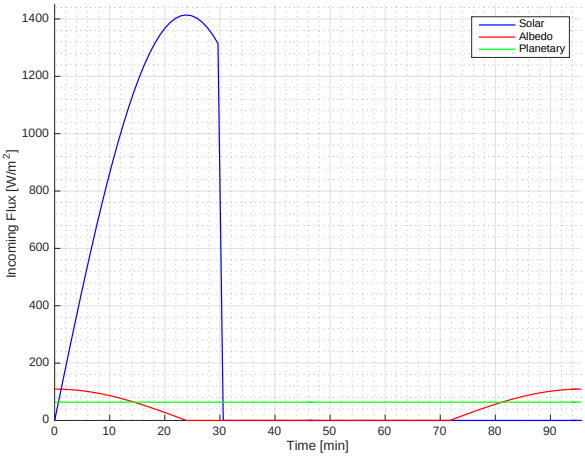

(d) Side 4: Aft facing

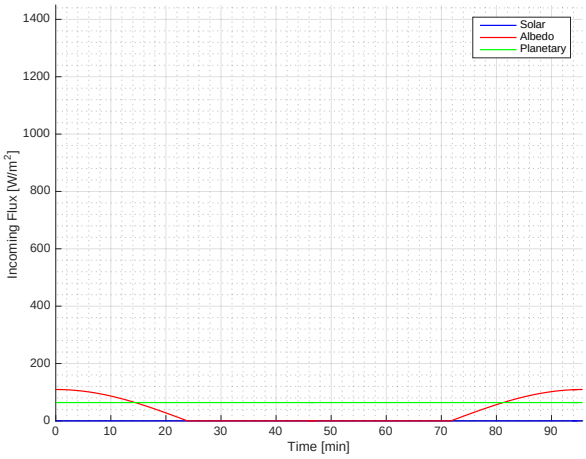

(e) Side 5: West facing

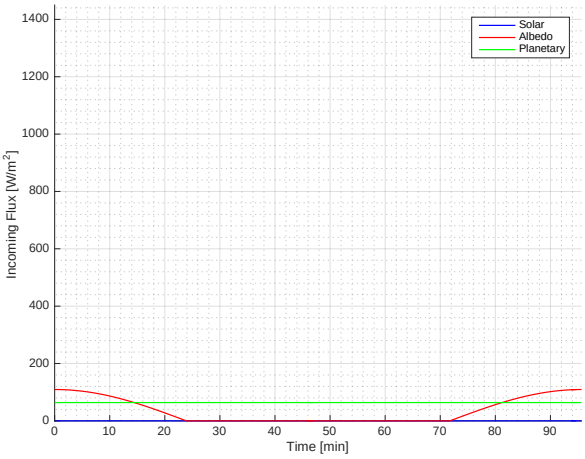

(f) Side 6: East facing

Figure 9.4 Incoming fluxes on a box-like satellite at an orbital altitude of 550 km

9.3 Articulated Boom

This section presents the analysis results of the articulated boom. For the articulated boom a few assumptions were made. The first assumption is that the root hinge is not included in the analysis, as a detailed design of the hinge would be required, including the mechanical performances. Also in the analytical calculations the stiffness of this root hinge was not included. The next assumption derives from the first assumption and is that the end of the rear boom is fully clamped. The final assumption is based on the problems with the contacts settings as mentioned in section 9.1. The hinges are assumed to be fully locked and due are made out of a solid part. As this part was fully solid, the total mass of the hinge for this analysis was increased with a small amount. However, the analytical results were corrected for validation. In Figure 9.5 the representation of the test set-up can be seen, including the coordinate system used for the analyses. In this section the static analysis will be discussed first, followed by the modal, harmonic, and thermal analyses.

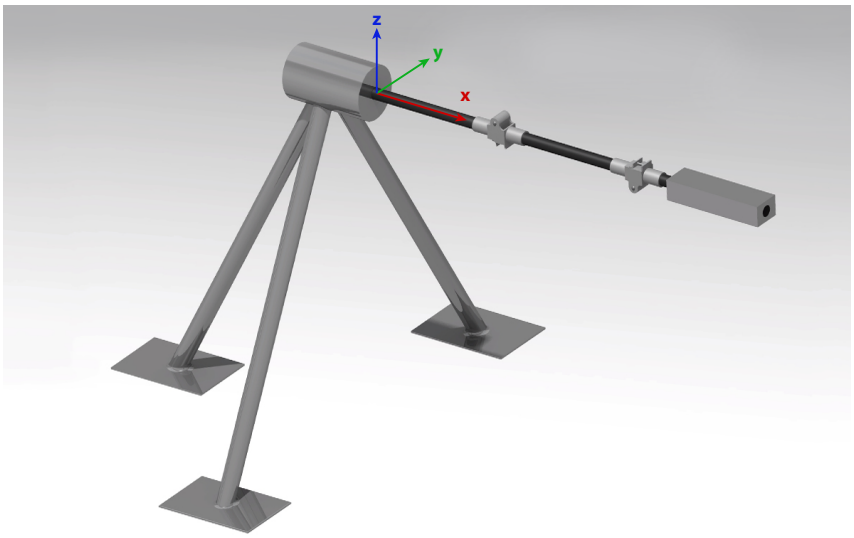

Figure 9.5 Representation of articulated boom test set-up

9.3.1 Static Analysis

The first analysis is the static analysis. In this analysis the deflections due to self-weight and due to the OEB under various magnitudes of the gravitational acceleration were calculated. In the analytical calculations of the deflection (see chapter 6), the hinges were assumed to be point loads acting on a CFRP tubular boom. Thus, the stiffness of each hinge was not included in this calculation. Therefore it was expected that the deflections in ANSYS would be lower, as the hinges are included in ANSYS and do provide stiffness. Even though the moment of inertia of the articulated boom is approximately the same in both z and y-direction, a gravitational load was applied on both directions (negative) separately, to validate this assumption.

In the first analysis, the boom was used without an end mass, so without the OEB attached. The results are shown in Table 9.2 and Table 9.3. As can be seen in both tables, the prediction that the analytical results would be higher than the ANSYS results is confirmed. However, the values are still relatively close to each other. Also the deflections about both axes are about the same and the assumptions therefore also validated. In the second analysis the tip mass (a representative of the OEB), was attached to the boom and the same gravitational loads were applied. The results are shown in Table 9.4 and 9.5.

What can be noticed in these tables, is that there is a larger difference between the ANSYS results and the analytical results. The influence of the hinges is more noticed in when the tip mass is applied. As the booms were designed for milli-gravity conditions, to ensure enough stiffness in both on-ground and space

Table 9.2 Deflection of articulated boom due to self-weight with gravitational acceleration pointed in the negative z-direction

	ANSYS	Analytical	
g	δ_{max}	δ_{max}	$\Delta\delta_{max}$
[m/s^2]	[µm]	[µm]	[%]
9.81	$1.84 \cdot 10^4$	$2.03 \cdot 10^4$	9
$9.81 \cdot 10^{-3}$	1.84	2.03	9
$9.81 \cdot 10^{-6}$	$1.84 \cdot 10^{-3}$	$2.03 \cdot 10^{-3}$	9

Table 9.3 Deflection of articulated boom due to self-weight with gravitational acceleration pointed in the negative y-direction

	ANSYS	Analytical	
g	δ_{max}	δ_{max}	$\Delta\delta_{max}$
[m/s^2]	[µm]	[µm]	[%]
9.81	$1.85 \cdot 10^4$	$2.03 \cdot 10^4$	9
$9.81 \cdot 10^{-3}$	1.85	2.03	9
$9.81 \cdot 10^{-6}$	$1.85 \cdot 10^{-3}$	$2.03 \cdot 10^{-3}$	9

Table 9.4 Deflection of articulated boom with end mass with gravitational acceleration pointed in the negative z-direction

	ANSYS	Analytical	
g	δ_{max}	δ_{max}	$\Delta\delta_{max}$
[m/s^2]	[µm]	[µm]	[%]
9.81	$1.12 \cdot 10^4$	$1.43 \cdot 10^4$	22
$9.81 \cdot 10^{-3}$	11.2	14.3	22
$9.81 \cdot 10^{-6}$	$1.15 \cdot 10^{-2}$	$1.43 \cdot 10^{-2}$	20

Table 9.5 Deflection of articulated boom with end mass with gravitational acceleration pointed in the negative y-direction

	ANSYS	Analytical	
g	δ_{max}	δ_{max}	$\Delta\delta_{max}$
[m/s^2]	[µm]	[µm]	[%]
9.81	$1.12 \cdot 10^4$	$1.43 \cdot 10^4$	22
$9.81 \cdot 10^{-3}$	11.2	14.3	22
$9.81 \cdot 10^{-6}$	$1.14 \cdot 10^{-2}$	$1.43 \cdot 10^{-2}$	20

conditions, the deflections of all analyses in the quasi-static micro-gravity conditions are in the nanometer range. Therefore it can be concluded that the boom will satisfy the deflection requirement under quasi-static micro-gravity conditions. In Figure 9.6 an impression of the deflection during the static analysis is given, including the end mass.

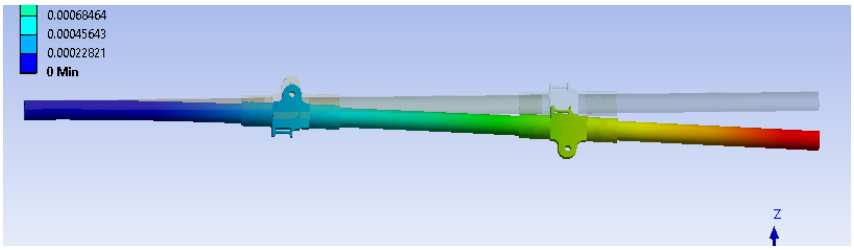

Figure 9.6 Representation of articulated boom test set-up

9.3.2 Modal & Harmonic Analysis

Even though the deformation of the boom under micro-gravity conditions is below the micrometer range, vibrations can allow the boom to deflect at higher magnitudes when the boom starts to resonate. This resonance will occur if external vibrations will vibrate at the same natural frequency of the boom. One of the requirements (R-M2D-STR-4) was that the total system shall have a natural frequency higher than 5 Hz. The natural frequencies of the articulated boom are shown in Table 9.6. These frequencies are calculated without the end mass (left part of Table 9.6) and with the end mass (right part of Table 9.6).

First the results without the OEB are discussed. As the analytical calculations are based on a very simplified model, it was expected that there would be a large deviation between the results. For the analytical results the mass which was used in Equation 6.11 is the combination of the boom mass and the mass of

Table 9.6 Natural frequencies of articulated boom with and without end mass

	Without OEB			With OEB		
Frequency	**ANSYS**	**Analytical**	**Difference**	**ANSYS**	**Analytical**	**Difference**
Mode	[Hz]	[Hz]	[%]	[Hz]	[Hz]	[%]
1	15.9	11.6	37	5.2	4.1	21
2	15.9	11.6	37	5.3	4.1	19
3	111.3	72.3	54	62.6		
4	111.6	72.3	54	63.0		
5	209.1	202.6	3	67.7		
6	326.5	397.4	18	188.5		

the two hinges. The first two modes, which are about the same due to the symmetrical boom, have a difference of about 4 Hz. When looking at the third and fourth mode, the differences become significantly high, while the differences between the final modes are relatively small. This is because the third and fourth mode were directly related to the hinges. In chapter 11 the effect of the hinges on the natural frequency will be further elaborated.For the results with the OEB attached, only the first two modes could be calculated analytically using Equation 6.12. Because of the stiffness of the hinges, the natural frequencies are higher, compared to the analytical results. However, the difference between the results is only about 1 Hz. One of the requirements of the mechanism is that the natural frequency shall be higher than 5 Hz. In both cases, with or without the OEB attached, this requirement is met. However, this can only be fully concluded if a detailed design has been made of the hinge and a prototype has been tested.

To show the effect of the boom vibrating at the natural frequency on the total deflection, a frequency response plot was made for vibrations in y and in z-direction with a gravitational acceleration of 1-µg. The articulated boom including end mass was used for this analysis, as it has to be a representative for the demonstration mission. The plot is shown in Figure 9.15.

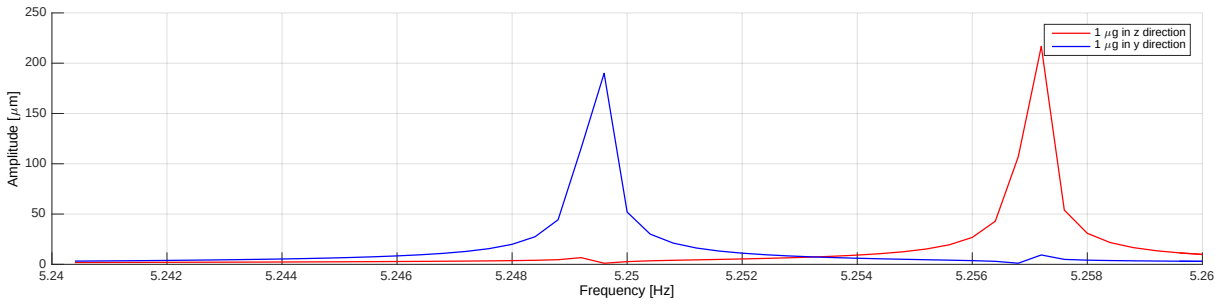

Figure 9.7 Frequency response plot of articulated boom with end mass

The maximum allowed deflection of the articulated boom is 15 µm in the z and y-direction of this coordinate system. Note that this coordinate system is different than the one presented in chapter 2. What can be noticed from Figure 9.15 is that this value is surpassed with a factor of larger than 10. The risk of vibrating at such a frequency can clearly be seen and will have a critical consequence on the optical performance of the DST. Therefore, it is of high importance that the boom is designed to stay out of reach of the frequencies of vibrations caused by other component on the DST.

9.3.3 Thermal Analysis

For the thermal analysis the values the incoming flux are used (see Figure 9.4). These values are multiplied first with the absorptivity of CFRP and aluminum, which are 0.85 and 0.15, respectively [75].

Other values for the thermal analysis can be found in Table 9.7, where c is the thermal capacity, k is the thermal conductivity, α is the absorptivity, and ε is the emissivity.

Table 9.7 Thermal properties of CFRP and aluminum alloy 7075 [75]

Material	c	k	α	ε
	[J/(kg·C)]	[W/(m·C)]	[-]	[-]
CFRP	1100	20	0.85	0.85
Aluminum (7075)	960	134	0.15	0.05

The box which was modeled for the incoming fluxes, has three couples of opposite sides. The values for these sides have been applied, including the absorptivity, to each half of the boom. It is chosen to only apply incoming flux on the flat side parts of the hinge, as these are the largest surfaces. The incoming fluxes on other sides are neglected, as this would introduce more complexity. Furthermore the outer surface of the CFRP segments and the hinges have been set-up as a radiative surface with a surrounding temperature of -273 °C. The emissivity of these materials (Table 9.7) is used in the settings of the radiative surfaces. With these settings the temperature of the boom under the various cases have been determined using the Thermal Transient option in ANSYS. It is assumed that the boom starts with an initial temperature of 20 °C as this is the reference temperature for the CFRP material.

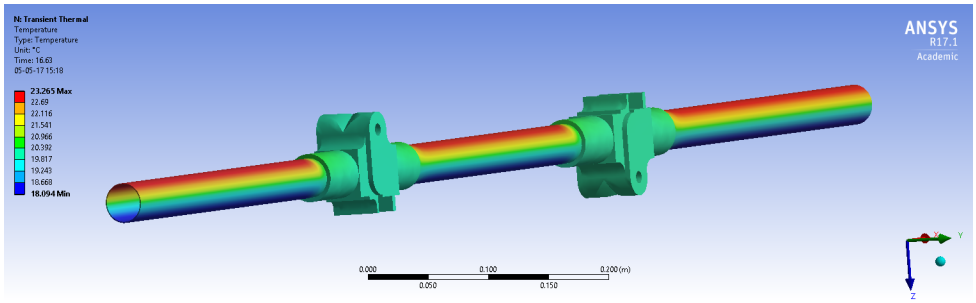

Figure 9.8 Temperature distribution of articulated boom with different incoming flux at front and back

An example of the temperature distribution of the articulated boom can be seen in Figure 9.16. Using the outcome of the temperature distribution over time, the deformations in each axis have been calculated. Note that these deformations only include deformations due to thermal effects and not gravitational effects. In Figure 9.9, Figure 9.9, and Figure 9.9 the results are shown. To improve in calculation time, the orbital period has been divided down into 10 time steps for the deflection calculation, while there were 122 time steps for the temperature calculations. Therefore the temperature graph is more smooth. Note that the absolute values for the deflections are used in the deflection plots.

The temperature difference for the first case, as shown in Figure 9.9a stays within a boundary of 5°C. The maximum and minimum temperatures are mostly located in the segments, while the temperature of the hinges are fluctuating around the average temperature (see Figure 9.8). Even though the temperature difference between the maximum and minimum is relatively small, the deformations caused by this difference in temperature is significant in the micrometer range. In Figure 9.9b it can be seen that the highest deflections occur in the z-axis. This is because the boom has the maximum and minimum temperatures of the opposite faces, which cause the boom to bend and deflect along the z-axis. However, the deflections along this axis surpass the limit of 15 µm, and is expected to have higher deflections during further orbital periods. Furthermore the boom experience a significant amount of expansion along the x-axis as well. Recalling requirement *R-M2D-DS-STR-2*, it states that the mechanism shall have a maximum deflection of 10 µm in the z-direction. As the z-axis of the requirements is the x-axes of this analysis, it means that the deflection along the orbit exceeds this requirement with a few micrometers. This can cause a diffraction in the image of the telescope.

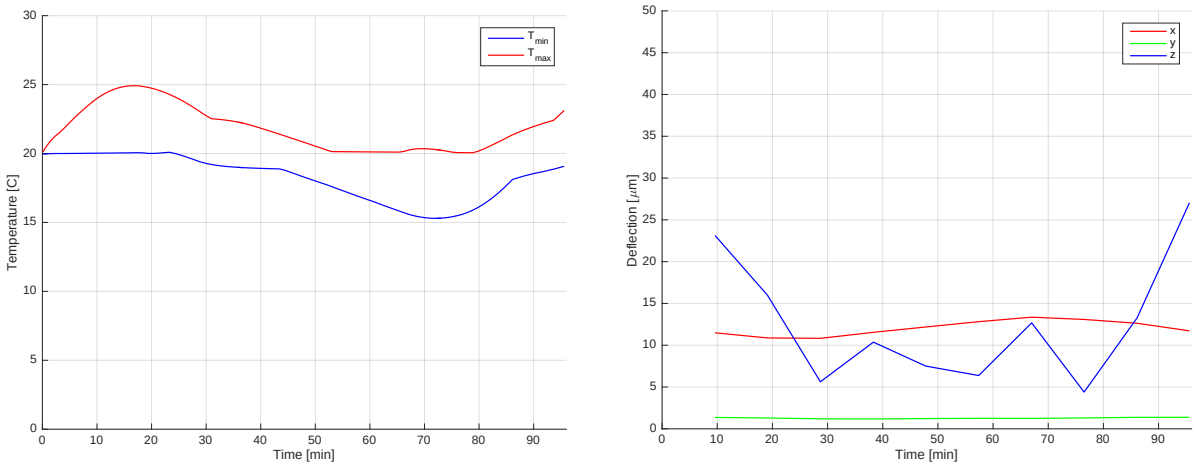

(a) Temperature **(b)** Deflection

Figure 9.9 Temperature and deflection of articulated boom based on incoming flux of box side 1 and 2

Looking at all the temperature distributions in the figures, the prediction of the worst-case scenario, which was done in the previous section, is confirmed. It was expected that the deflections would be largest due to the largest mean difference of the maximum and minimum temperatures, when using the incoming fluxes of box sides 3 and 4. In this case, compared to side 1 and 2, the deflections along the x and y-axes stay approximately the same. Nevertheless, the boom has higher differences in temperature causing the boom to bend even more. The peak deflection is 45 µm, which is three times higher than the maximum allowed deflection for the system. This is an issue which has to be dealt with during the detailed design process.

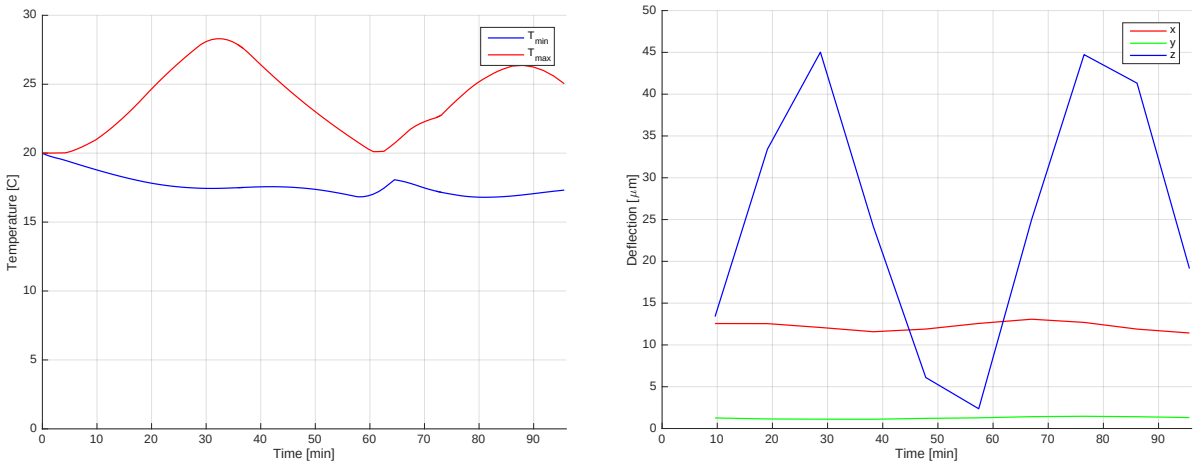

(a) Temperature **(b)** Deflection

Figure 9.10 Temperature and deflection of articulated boom based on incoming flux of box side 3 and 4

When the boom is oriented such as side 5 and 6 of the box, the incoming heat flux is low. As the aluminum has a low emissivity, the temperature stays quite constant over the orbit. However, due to the high emissivity of the CFRP material, the segments radiate quite a lot of its temperature into outer space, causing the temperature to drop significantly compared to the hinges. A snapshot of the temperature distribution during this orbital period is shown in Figure 9.12, which can be used to get a better understanding of Figure 9.11. As the segments have quite a uniformal temperature distribution, the dominating deflection is caused in the x-direction, as the segments are contracting due to the temperature drop. This contraction exceeds the limit of 10 µm at the half of the single orbit, and as the boom has almost no incoming heat

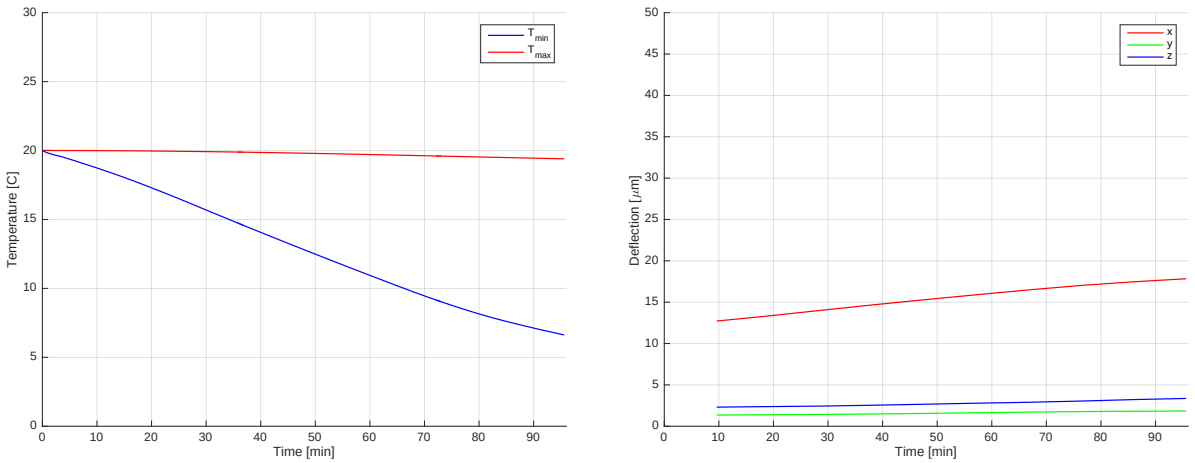

(a) Temperature **(b)** Deflection

Figure 9.11 Temperature and deflection of articulated boom based on incoming flux of box side 5 and 6

flux, the temperature keeps decreasing, causing a larger contraction of the boom.

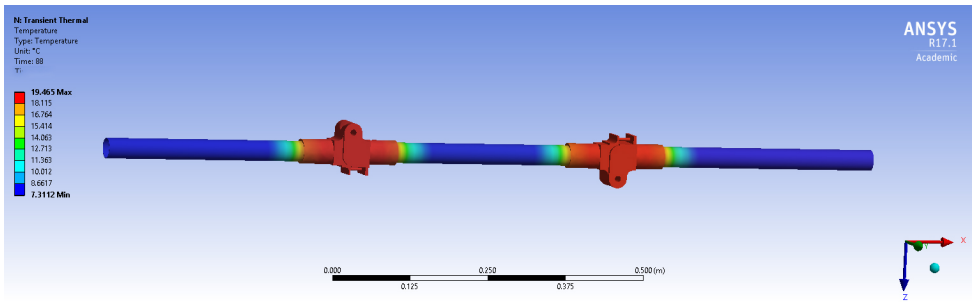

Figure 9.12 Temperature distribution of articulated boom with different incoming flux at front and back

As could be seen in this analysis, the thermal effects on the boom are critical. The deflections in the x and z-directions are significantly high and exceed the given requirement of the mechanism, to allow the required optical performance of the telescope. To keep reduce the amount of deflection in the z-direction, options need to be considered to keep the front and back of the boom at more or less the same temperature. An option could be to use a baffle around the whole telescope, an extending collar around the booms, or a layer of aluminum coating could be applied to the boom to decrease the amount of absorptivity and emissivity. To see the effect of aluminum coating, the worst-case scenario (side 3 and 4) is used as reference. The theoretical values of the emissivity and absorbtivity of aluminum are applied to the surface of the CFRP segments. Note that in practical, these segments cannot fully reach these values as the coating can get damaged due to various reasons. In Figure 9.13 the results of the coated boom are shown and are plotted against the results of the non-coated boom.

As can be seen in Figure 9.13a the maximum temperature and minimum temperature are both shifted more to the initial temperature of initial 20°C. Also the difference between these maximum and minimum temperatures has decreased. This means that a reduction in deflection is expected. This is confirmed when looking at Figure 9.13b. The deflection in the y-axis stays the same and the deflection along the x-axis is slightly increased as the overall temperature is lower than before. The largest difference can be seen in the deflection along the z-axis. The peak has reduced with a factor of about 3, which is a significantly high amount. The peak is still reaching the 45 µm, however a large improvement is noticed. Therefore, from a deflection perspective, a aluminum coating would certainly beneficial. Nevertheless, it was still noticed that the deflection along the longitudinal axis of the boom still exceeds the requirement. As already mentioned, options should be considered in the future design of the mechanism, such as readjustment of

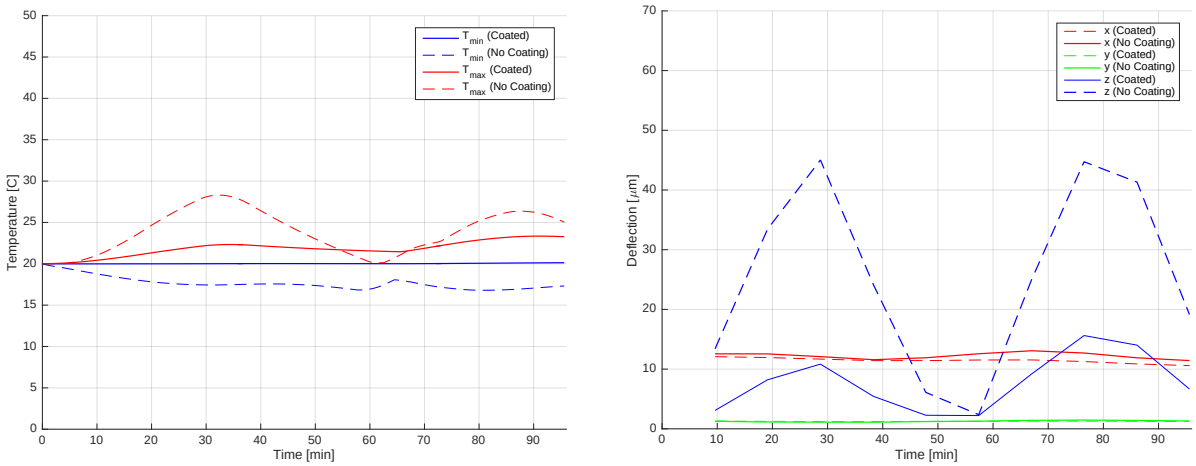

(a) Temperature **(b)** Deflection

Figure 9.13 Temperature and deflection of articulated boom based on incoming flux of box side 3 and 4, with and without aluminum coating

the materials for the hinges and the CFRP lay-up of the segments.

9.4 CTM Boom

The same analyses performed for the articulated boom has been performed for the CTM boom as well. In Figure 9.14, the a representation of the test set-up can be seen, including the coordinate system used in ANSYS. It is assumed that the boom is fully clamped at the root. In the subsections below, the results of the analyses are presented.

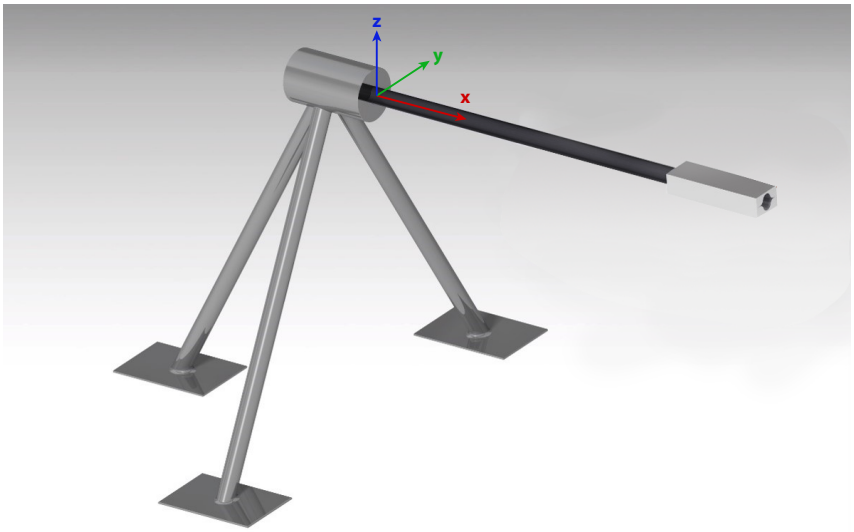

Figure 9.14 Representation of CTM boom test set-up

9.4.1 Static Analysis

The model and settings have been validated by comparing the results with the analytical results obtained from the MATLAB optimization and analysis script of the CTM boom. A gravitational acceleration have been applied to the boom in z-direction and separately in the y-direction. This has been done as the

boom has different values of stiffness depending on the axis. In Table 9.8 and Table 9.9 the results are shown.

Table 9.8 Deflection of boom due to self-weight with gravitational acceleration pointed in the negative z-direction

	ANSYS	Analytical	
g	δ_{max}	δ_{max}	$\Delta\delta_{max}$
[m/s^2]	[µm]	[µm]	[%]
9.81	231	233	1
$9.81 \cdot 10^{-3}$	0.231	0.233	1
$9.81 \cdot 10^{-6}$	$2.31 \cdot 10^{-4}$	$2.33 \cdot 10^{-4}$	1

Table 9.9 Deflection of boom due to self-weight with gravitational acceleration pointed in the negative y-direction

	ANSYS	Analytical	
g	δ_{max}	δ_{max}	$\Delta\delta_{max}$
[m/s^2]	[µm]	[µm]	[%]
9.81	119	117	2
$9.81 \cdot 10^{-3}$	0.119	0.117	2
$9.81 \cdot 10^{-6}$	$1.19 \cdot 10^{-4}$	$1.17 \cdot 10^{-3}$	2

The results of ANSYS are for both cases very accurate, when comparing them to the analytical results. The slight difference in result probably originates from the contacts setting and meshing of the boom. What can be noticed for both cases, is that there is a linear relation between the gravity and the deflection. This was also noticed in the static analysis of the articulated boom. If no buckling occurs, what is not expected to occur due to self-weight, this conclusion is valid. This would mean that the measured deflection during an experiment can be divided with $1 \cdot 10^6$ to obtain the expected deflection in space. However, if buckling occurs during 1-g conditions, this calculation is not valid anymore. An important conclusion to be drawn from this analysis is that the deformation due to self-weight under micro-gravity conditions in space is far from critical. The deflection is even lower than a nanometer.

When applying a representative element for the OEB on the top 30 cm of the boom, higher deflections are expected. These results are shown in Table 9.10 and Table 9.11.

Table 9.10 Deflection of CTM boom with end mass with gravitational acceleration pointed in the negative z-direction

	ANSYS	Analytical	
g	δ_{max}	δ_{max}	$\Delta\delta_{max}$
[m/s^2]	[µm]	[µm]	[%]
9.81	$1.40 \cdot 10^4$	$1.42 \cdot 10^4$	1
$9.81 \cdot 10^{-3}$	14.3	14.2	1
$9.81 \cdot 10^{-6}$	$1.43 \cdot 10^{-2}$	$1.42 \cdot 10^{-2}$	1

Table 9.11 Deflection of CTM boom with end mass with gravitational acceleration pointed in the negative y-direction

	ANSYS	Analytical	
g	δ_{max}	δ_{max}	$\Delta\delta_{max}$
[m/s^2]	[µm]	[µm]	[%]
9.81	$7.15 \cdot 10^3$	$7.13 \cdot 10^3$	0
$9.81 \cdot 10^{-3}$	7.17	7.13	1
$9.81 \cdot 10^{-6}$	$7.18 \cdot 10^{-3}$	$7.13 \cdot 10^{-3}$	1

Even though a mass of 3.2 kg is attached to the boom, the deflection of the boom is still in nanometer range in micro-gravity conditions. Even during on-ground experiments the boom will not deform at such state that buckling is expected. Also the values of these analyses have been validated with the analytical solutions. With these results it can be concluded that the deformation due to micro-gravity is negligible and the settings of ANSYS are correct in order to continue with further analysis.

9.4.2 Modal & Harmonic Analysis

For the first analysis the natural frequency of the CTM boom alone is calculated. After this analysis, the end mass was applied and the natural frequencies were calculated again. These results can be found in Table 9.12

An important observation is that the natural frequencies calculated by ANSYS are not close to the ana-

Table 9.12 Natural frequencies of CTM boom with and without end mass

	Without OEB			With OEB		
Frequency	**ANSYS**	**Analytical**	**Difference**	**ANSYS**	**Analytical**	**Difference**
Mode	[Hz]	[Hz]	[%]	[Hz]	[Hz]	[%]
1	40.7	35.6	14	4.6	3.8	21
2	56.7	50.3	13	6.4	5.4	19
3	174.2	222.7	22	43.4		
4	245.8	314.5	22	84.4		
5	262.6	624.7	58	113.9		
6	289.1	881.9	67	232.2		

lytical solutions. The first two natural frequencies of the first analysis show to have an accuracy of about 87%, however the higher the mode becomes, the less accurate ANSYS becomes. This phenomena was also found multiple times in other literature. Experimental validation is required to determine which of the two results are accurate.

When applying the end mass, it is only possible to calculate the first two natural frequencies, which correspond to the two moments of inertia, using Equation 6.12. The first frequency does not meet the requirement of 5 Hz, which can be critical. If this concept is chosen, methods need to be found to increase the natural frequency. Based on Equation 6.12, one could reduce the end mass, reduce the length, use a CFRP laminate with a higher Young's modulus, or increase the moment of inertia of the boom.

To see the deflections at these frequencies including the end mass, a frequency response plot was made for vibrations in y and in z-direction with a gravitational acceleration of 1-µg. This frequency response plot can be seen in Figure 9.15.

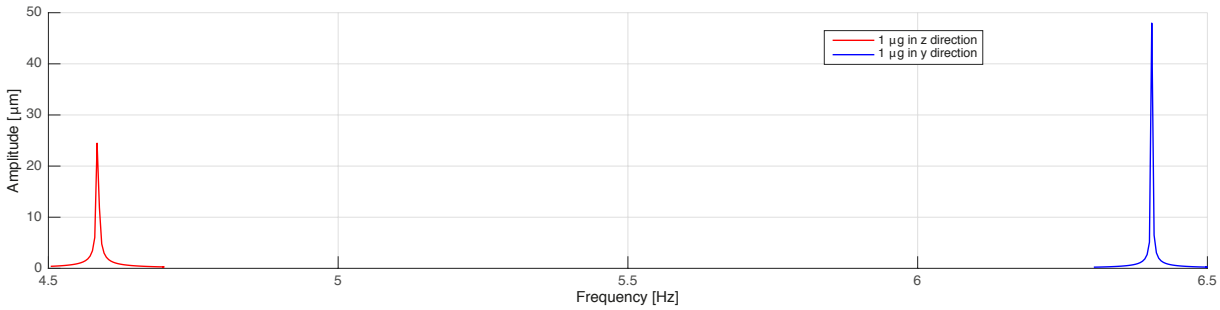

Figure 9.15 Frequency response plot of CTM boom with end mass

Referring back to requirement R-M2D-STR-1, the boom shall not have a deflection higher than 15 µm in the y and z-direction of the current coordinate system (note that the coordinate system used for the requirements is different). From the figure it can be concluded that the deflections at the natural frequencies surpass the 15 µm limit. This should be taken into account during the system design, as it can have high impact on the performance of the telescope if the boom starts to resonate. With these results the structural analysis part is concluded. In the following subsection, the results of the thermal analysis is presented.

9.4.3 Thermal Analysis

This thermal analysis performed similarly to the approach of the thermal analysis of the articulated boom. An example of the temperature distribution of the CTM boom can be seen in Figure 9.16. The results of

the temperature and deflection over the orbital period, for the different incoming fluxes, can be seen in Figure 9.17, Figure 9.18, and Figure 9.19.

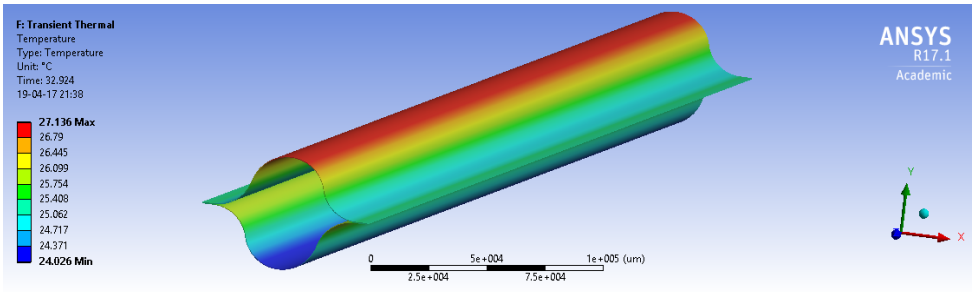

Figure 9.16 Temperature distribution of CTM boom with different incoming flux at front and back

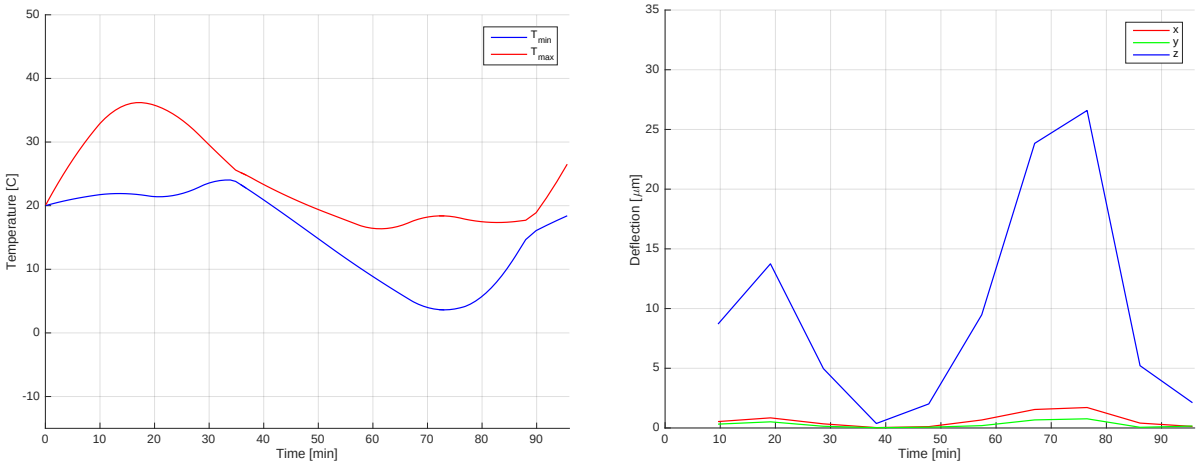

(a) Temperature **(b)** Deflection

Figure 9.17 Temperature and deflection of CTM boom based on incoming flux of box side 1 and 2

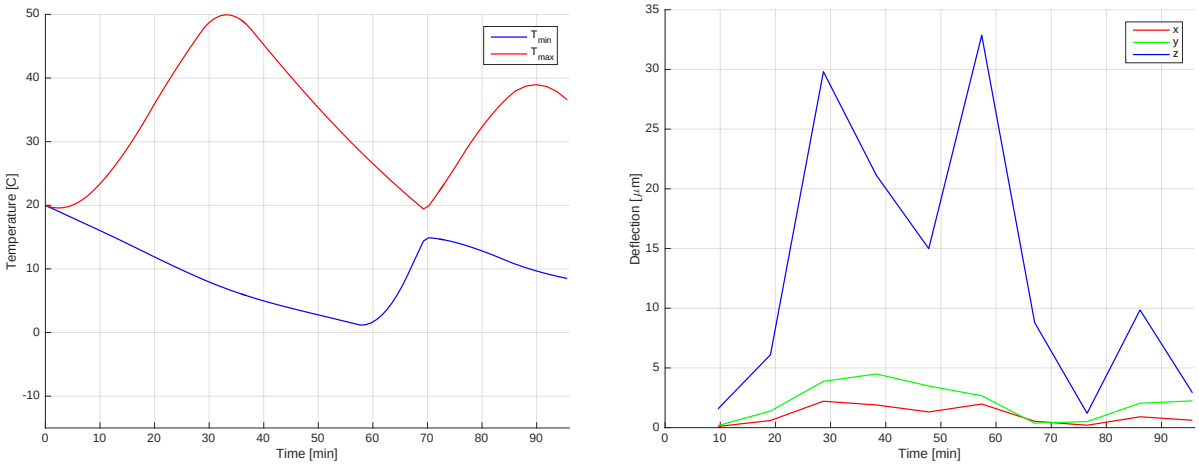

(a) Temperature **(b)** Deflection

Figure 9.18 Temperature and deflection of CTM boom based on incoming flux of box side 3 and 4

What can be noticed when looking at all figures, is that the highest temperature differences and deflection occur when the boom is oriented with its front in velocity direction and its back in aft direction, so side 3 and 4 (Figure 9.18). This was already seen in the thermal analysis of the articulated boom. In this case the boom will have significant deflections in the z-direction. The deflections in x and y-direction are in the

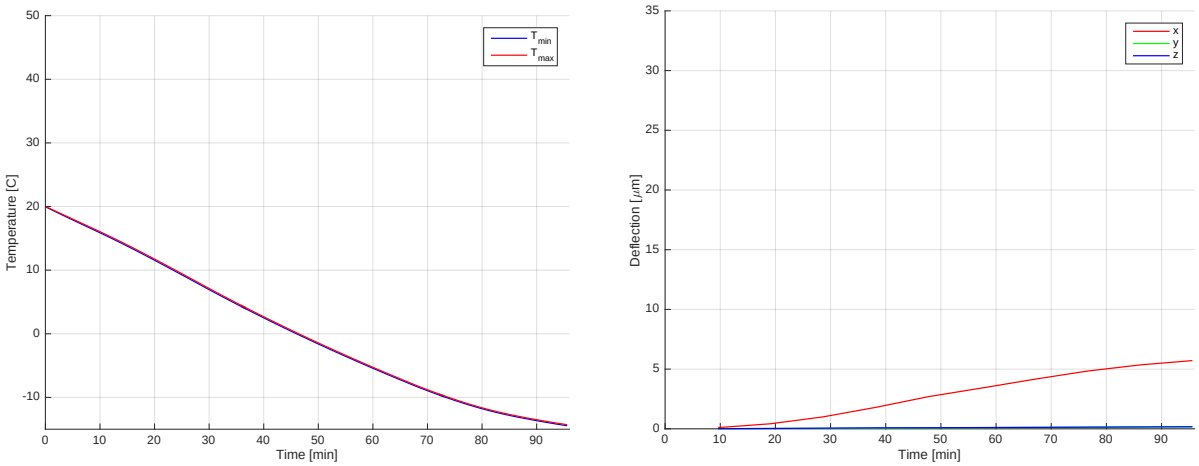

(a) Temperature

(b) Deflection

Figure 9.19 Temperature and deflection of CTM boom based on incoming flux of box side 5 and 6

micrometer range, however are still below the acceptance limit. For the case of side 1 and 2 (Figure 9.17) and side 3 and 4 (Figure 9.18) the deflections surpass the limit of 15 µm. This is a critical issue.

If the booms are oriented in the West and East direction (Figure 9.19), the booms will not experience this problem. In this case the boom will only shrink in the x-direction, as the incoming fluxes are minimal. However, the CTM boom cannot be considered as a flat plate, and will obtain certain amount of heat flux on the sides of the boom. This cannot be modelled in ANSYS as the shape is too complex. For this an actual experiment is required or more advanced modelling software is required.

With these results, this chapter is concluded. Both boom have been analyzed using structural, modal, harmonic, and thermal analyses. The next chapter will elaborate on the differences between these results.

Results Comparison 10

In this chapter a detailed comparison is made between the articulated boom and the CTM boom, which were designed analyzed in the previous chapters. First the boom properties are compared, including the mass, stowed volume, and deployment ratio. Next, the mechanical performance and thermal performances are compared, which include the results of chapter 9. Furthermore, the risks of each mechanism are compared. This chapter will be concluded with a final trade-off between the two mechanisms and a final conclusion is drawn on which boom is the optimal boom design for the DST project.

10.1 Boom Properties

Both booms have been designed to meet the given requirements, as presented in chapter 2. In Table 10.1 the most important boom properties of both designs are recapped.

Table 10.1 Comparison of boom properties

Deployment Mechanism	Total mass	Stowage volume	Stowed length	Deployment ratio	Active Controlled deployment
	[kg]	[cm^3]	[cm]	[-]	
Articulated boom	2.46	6111	48.5	2.7	No
CTM boom	3.33	5425	31	4.2	Yes

10.1.1 Total Mass

To start off with the total mass, the articulated boom has shown to have a lighter total mass than the CTM boom, with a difference of about 1 kg. When multiple booms are used in the deployment mechanism, such as for the full design of the DST, this difference could even go up to 4 kg, which is a significant amount of extra mass. From the literature review in chapter 3 and the technology comparison in chapter 4, an impression was given that the SMC types of booms tend to be very lightweight. If only the booms itself are considered, this is a valid impression. However, in the research for deployable booms, the mass of the HDRM was not included. This was not done in this literature review, nor in the research performed by Puig *et al.* [2]. The CTM boom itself had a mass of 145 g, which is only about 4% of the total CTM boom mechanism. However, even though the mass of the HDRM is high, it allows the CTM boom to have a controlled deployment.

The mass of the articulated boom is mostly dominated by the hinges and the HDRM. Also in this case the CFRP segments only take about 7% of the total mass of the mechanism. This design does not include controlled deployment, by for example introducing an electric drive at the root. It is all based on spring energy. With the use of a damping wire, the motion can be controlled in some kind of way, but this is only passive. Nevertheless, this kind of system is widely used by ADS and is space proven.

10.1.2 Dimensions

Even though the articulated boom has a lower mass, the CTM boom has a lower stowage volume. This can be an important property if volume constraints play an important role for the mission. Also the stowed length of the CTM boom is lower than the articulated boom. Another advantage of the CTM boom over the articulated boom is that the HDRM of the CTM boom can be built inside the bus of a satellite, while the articulated boom is mostly attached on the outside of the spacecraft. Furthermore, due to this smaller

stowed length, the deployment ratio of the CTM boom is also higher, which is positive. So in terms of compactness, the CTM boom mechanism is smaller than the articulated boom. These results do match with Figure 4.2 in chapter 4.

10.2 Mechanical Performance

Looking at the mechanical performance, it was expected that the results of the booms would be more or less the same as they were designed and optimized for the same requirements. A recap of the most important results of the static, modal and harmonic results of chapter 9 are shown in Table 10.2.

Table 10.2 Comparison of mechanical performance

Deployment Mechanism	Max. defl. z (Static)	Max. defl. y (Static)	Max. defl. z (Harmonic)	Max. defl. y (Harmonic)	First mode natural freq.
	[μm]	[μm]	[μm]	[μm]	[Hz]
Articulated boom	$1.15 \cdot 10^{-2}$	$1.14 \cdot 10^{-2}$	216.8	189.9	5.2
CTM boom	$1.43 \cdot 10^{-2}$	$7.18 \cdot 10^{-3}$	48.0	24.5	4.6

10.2.1 Static Results

As was already concluded in chapter 9, the deflections due to (quasi-)static gravity in space is very minimal. The largest deflection does not even reach the micrometer range, so from this perspective both designs meet the requirements. The articulated boom has less deflection along the z-axis due to the extra stiffness of the aluminum hinges, however if the gravity is pointing in the y-direction, the CTM boom has less deflection due to the higher moment of inertia.

An important note however is that the assumption was made that both booms are fully clamped. This is an important assumption when comparing the two mechanisms. The articulated boom can be fully clamped when the root hinge locks itself. The CTM boom can only be fully clamped if the support plate clamps the boom along the flanges and preferably also around its shape. This, however, is a complex process and should be further researched if the CTM boom shows to be the optimal boom design. It can be thus concluded that even though the articulated boom and the CTM boom, both meet the requirements when they are fully clamped, the results of the articulated boom seem more reliable than the ones of the CTM boom due to the complexity of the root clamping.

10.2.2 Modal & Harmonic Results

Looking at the harmonic deflections in Table 10.2, it can be noticed that the results of the articulated boom are more than five times higher than the results of the CTM boom. This has probably to do with the fact that the articulated boom has a much higher mass than the CTM boom, causing the boom to have higher deflections. This could also be caused by the interval steps taken for the frequency response calculation and that a peak of the CTM boom might have been missed. However, the process have been iterated until the highest deflection was found. Despite the values, they both have shown that it can become critical for the DST if the boom starts oscillating at its natural frequency.

Even though both booms were not specifically designed to have natural frequencies higher than 5 Hz, the stiffness and mass of the booms have automatically caused the boom to have the first natural frequency around this value. As the articulated boom has a higher mass, the natural frequency is slightly higher than the CTM boom, however this difference is marginal. This has to do with the fact that the natural frequency is dominated by the end mass (see Equation 6.12). In conclusion, there is no specific boom which performs better in terms of harmonic results.

10.3 Thermal Performance

The final analysis of chapter 9, was the thermal analysis. In Table 10.3 the most important values over all results are shown.

Table 10.3 Comparison of thermal performance

Deployment Mechanism	Max. temp.	Min temp.	Max. defl. x	Max. defl. y	Max. defl. z
	[˚C]	[˚C]	[µm]	[µm]	[µm]
Articulated boom	28.3	6.6	17.8	1.5	45.0
CTM boom	49.9	-14.3	5.7	4.5	32.9

10.3.1 Temperature

The main difference between the two boom types is that has major influence on the temperature is the use of aluminum hinges in the articulated boom mechanism. The CFRP material has a much higher emissivity and absorptivity than aluminum. This means that more energy is radiated to the surroundings and more energy is absorbed by the incoming heat flux. This effect can clearly be seen in Table 10.3. As the CTM boom only consist of CFRP the maximum temperature is much higher than the maximum higher of the articulated boom, and the minimum temperature is much lower than the minimum temperature of the articulated boom. The temperature of the articulated boom is kept more in balance due to the use of the hinges, which in their case cool the high temperatures of the CFRP segments and warm up the cold temperatures of the CFRP segments. This effect can clearly be seen when comparing Figure 9.10a and Figure 9.18a. So in terms of temperature, the articulated boom would have a better performance, however no conclusion can be drawn as the most important factor, the deflections, need to be compared first.

10.3.2 Deflections

Even though the maximum and minimum temperatures were found in the data of the CTM boom, most important is that the temperature difference in the boom is kept minimal to have the minimum amount of deflection. Looking at all the maximum deflections in Table 10.3, it shows that the maximum deflections for the CTM boom are significantly lower than the deflections of the articulated boom. This is probably caused by the use of the hinges. CFRP and aluminum have very different thermal properties, and the connections between these materials can have significant impact on the resulting behaviour. Therefore, it can be concluded that the CTM boom does perform better in terms of thermal results.

10.4 Risks

At the end of chapter 7 and chapter 8, the risks of both booms have been listed. Both risk maps are quite comparable. Nevertheless, there are important differences in the risks themselves. Most of the risks of the articulated boom come from the hinges and the possible failure. As the deployment is passively, not much extra components are required. This is different for the CTM boom mechanism. The HDRM of the CTM boom consist of multiple components, with each a risk of failure. As was mentioned, redundancy can be added, however this will have a negative effect on the total mass of the system. Another important risk which was already highlighted, is the clamping of the root. This risk is much higher for the CTM boom than for articulated boom. When looking at the amount of components and the risk they introduce in the system, one can conclude that the articulated boom will have the lowest risks in overall. Most of the identified risks were based on the current design and could be mitigated much easier than the risks of

the CTM boom mechanism.

10.5 Final Trade-Off

For the final trade-off, all results of both booms have been included. This trade-off is based on the preliminary trade-off from chapter 4, however in this case actual values could be used to get a more reliable outcome.

10.5.1 Trade-Off Parameters

The trade-off parameters are listed in order of their weight, including a brief description:

1. Risk (3): The risk has the highest weight as the deployment mechanism should be reliable, as this is a crucial part of the DST.
2. Stiffness (2): The stiffness of the boom is based on the structural performance of the boom under static and harmonic conditions.
3. Thermal stability (2): The thermal stability is the amount of deflection the mechanism experience in space during thermal effects. The lower the deflection the better.
4. Deployment ratio (2): The research question implies that the deployment ratio is an important trade-off parameter for the final decision. The higher the better.
5. Mass (2): The mass should be as low as possible.
6. Controlled deployment (2): If a mechanism has controlled deployment, more certainty can be guaranteed for correct deployment.
7. Complexity (1): As this is a university project, the complexity of such a deployable structure should be kept as low as possible. This however is not a key parameter.
8. TRL (1): Also the TRL is not a key parameter, but shows if these technologies have already been space proven, also introducing more reliability of the system. Furthermore, a higher TRL can reduce the development time.

10.5.2 Final Trade-Off

As only two mechanisms are compared, scores are only given with a 1 or a 2. When a mechanism performs better in terms of the relating trade-off parameter, it gets a score of 2 and the other gets a score of 1. Using this approach, a weighted score is calculated with a maximum score of 2. In Figure 10.1 the final trade-off is shown. The scores are based on the comparisons made in this chapter.

Criteria / *Deployable mech.*	Risk	Stiffness	Thermal stability	Deployment ratio	Mass	Controlled deployment	Complexity	TRL	Score
	3	2	2	2	2	2	1	1	Max. 2
Articulated boom	2	2	1	1	2	1	2	2	✓ 1.6
CTM boom	1	1	2	2	1	2	1	1	✗ 1.3

Figure 10.1 Final trade-off

10.5.3 Discussion & Conclusions

As can be seen from the final trade-off in Figure 10.1, the articulated boom has shown to be the best option for the deployment mechanism of the DST project. At the start of the literature review, the CTM boom

looked very promising: low mass, high deployment ratio, and the required stiffness could be met through an iteration process. However, with the knowledge based only on the literature it was not expected that the HDRM would be the bottleneck in the design. The HDRM had a major impact on the complexity, mass and risks.

If the alignment budget of the DST project would be less demanding, the results would have been different. The HDRM of the CTM boom could have been based passive and not actively controlled as the current design. Also the deployment length has played a major influence in the outcome. If a larger deployment length was required the articulated boom would require more hinges, which would result in a higher mass and also the risks of the articulated boom would increase. A prediction of the mass of both booms against the deployment length is made in Figure 10.2.

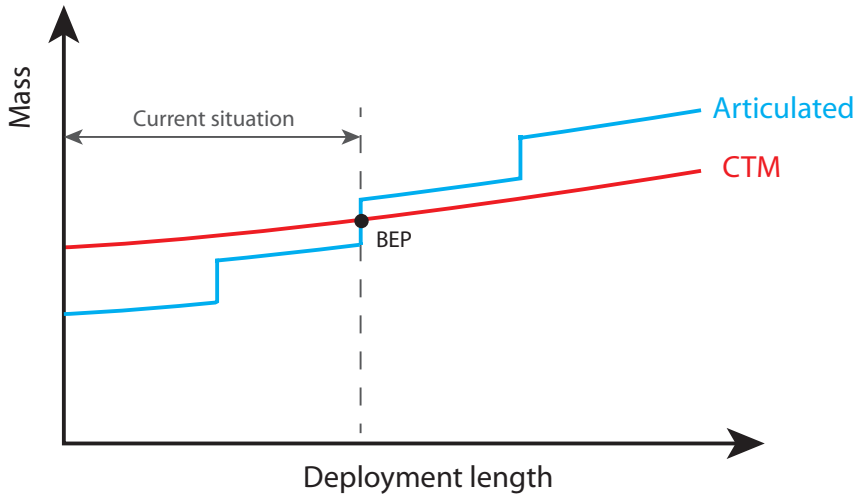

Figure 10.2 Mass prediction of articulated boom and CTM boom for larger deployment length

As shown, the articulated boom has a step increment after a certain deployment length, which is the hinges that are introduced in the concept to achieve the required deployment ratio. The CTM boom has a slow increase, as the HDRM slightly increases in mass, but the largest increment comes from the CTM boom itself. However, this is only a few grams and therefore it is expected that there will be a slow increment over deployment length. After the break-even point (BEP) the CTM boom would be a better option, as the HDRM design nearly changes, while the boom continuously adds extra hinges to meet the required deployment ratio.

In conclusion, for the DST mission the articulated boom has shown to be the best option in terms of risk, stiffness, mass, complexity and TRL. This is what ADS implied from the beginning, however no evidence was available. With this research the evidence have been provided. However, the idea of using CTM booms was also a realistic option and has shown to be a potential candidate for other astrophysics missions with less tight alignment budgets.

IV

Project Integration

DST System Design 11

Until now this report has been based on demonstration mission, as this would be the worst case scenario for the design of the booms. Nevertheless, the booms have to be adapted into the final design of the DST telescope. The main difference between the demonstration mission and the original mission, is that the demonstration mission uses only a single boom with an optical element box on top, while the original mission makes use of multiple booms with a secondary mirror on top. Also there are strict volume constraints for the demonstration mission, while the original mission has no strict volume constraints. Furthermore, the number of segments and the position of the booms on the instrument need to be determined. Once these are determined, a preliminary analysis of the mechanism can be performed. In this chapter these topics will be dealt with.

11.1 Interface Proposal

In this section an initial interface proposal is made. In a later stage of the DST project, a detailed design is required. The topics discussed in this section can form the base for this detailed design. First the number of segments are treated, followed by the location of the mechanism, and the interface with the secondary mirror.

11.1.1 Number of Segments

An important note at the start of this section is that the number of segments described in this section is only the number of tubular segments which allow the mirror to extend vertically. Extra hinges or members which allow the mirror to fold in the body of the instrument, while are positioned horizontally when deployed, are not categorized as 'segments'. For the demonstration mission, it was chosen to use three segments of the boom. The original mission, however, cannot have an uneven number of booms. Multiple booms are connected to the secondary mirror, so the mirror on top should be positioned at the top of the instrument, and not at the bottom as is the case of the demonstration mission. In Figure 11.1 the cases are shown.

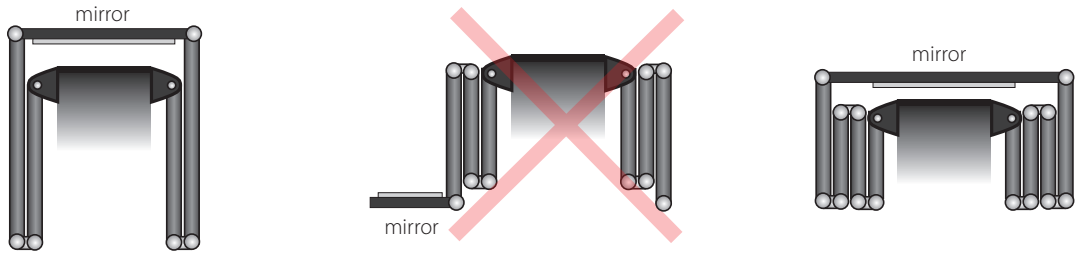

(a) Two segments **(b)** Three segments **(c)** Four segments

Figure 11.1 Number of boom segments with secondary mirror

As was shown in the comparison between the CTM boom and the articulated boom in chapter 10, the articulated boom can achieve a lower mass than a CTM boom due to the low amount of hinges used. However, more segments means more hinges, which will increase the total mass. At that point an articulated boom is not beneficial anymore. Also the more hinges used, the more errors can be introduced into the system. The total length of the boom should be therefore divided into two or four segments and not more, such as six or eight. In Table 11.2 a small trade-off of the two options are shown.

Criteria / No. of segments	Risk	Stiffness	Stability	Deployment ratio	Mass	Score
	3	2	2	2	1	Max. 3
Two	3	1	3	1	2	✓ 2.1
Four	1	3	1	2	1	✗ 1.8

Figure 11.2 Number of segments trade-off

Risk The more hinges used, the higher the risk becomes. Each hinge increases the amount of single-point failure that can occur. Not only the risk of failure has influence on the total risk, but also more possible alignment errors are introduced. Therefore the score of two segments is three times higher than the four segments option.

Stiffness One might assume that the stiffness decreases, when increasing the amount of hinges. Nevertheless, the hinges are made out of aluminum and have a higher stiffness than the CFRP tubes. Also the torsional spring, end stop, and a possible lock will make sure that the boom remains stiff. Furthermore, the total tube length is reduced which result in a lower deflection per boom. The relation between boom length and deflection is discussed in chapter 6. For this reason the four segments option has a three times higher score than the two segments option.

Stability Stability is the resistance to sudden change. One of the most crucial changes in space is the temperature, which varies over each part of the orbit. The hinges, made out of aluminum, do not have such a low CTE as CFRP (see Table 5.1) and will introduce higher deformations in the structure. Also the contact between CFRP and aluminum can introduce stability issues. The more contact points, the less stable the structure becomes. Hence, the two segment concept gets a score three times higher than the four segments concept.

Deployment Ratio If only two segments are used, the stowed length will be high compared to the four segments concept, as the longest segment has a length of about half or two third of the total length, while the longest segment in the four segments concept has only a length of a quarter or a third of the total length. The stowed width of the four segments concept, however, is double of the two segments concept. Therefore the difference deployment ratio between the two concepts is not significantly high, but the four segments concept still has a slight lower stowage volume than the two segments concept. This explains the score difference between the two concepts.

Mass The final trade-off criteria is the mass. Each extra hinge will introduce more mass to the system. Since the amount of hinges used for the four segments concept is double the amount of hinges used for the two segments concept, the score of the mass is also determined in the same ratio.

Result The difference between both concepts is not significantly high. Nevertheless, the most important trade-off criteria, risk, is crucial for determining which option would be most suitable. The two segments concept has the highest score and also has the least amount of risk introduced to the system. In conclusion the demonstration mission will make use of the least amount of segments possible for an uneven number of segments, namely three, and the original mission will make use of two segments. In the next section, the location of the mechanism on the instrument is discussed.

11.1.2 Location of Mechanism

The next important integration step of the mechanism is the attachment location of the mechanism on the instrument. The mechanism will consist of four articulated booms. In the original design, three booms were used, but this was based on a three segmented primary mirror. In the current design, the primary mirror consists of four segments. Three booms would have been enough for static equilibrium. Nevertheless, the three booms should be placed at an angle of 60° with respect to each other, which would mean that at least one of the booms would interfere with the light path from one of the segments to the

secondary mirror. Hence, three booms would not be an option. Reducing the amount of booms, for example to one or two, could lead to stability issues over at least one axis. Therefore, it is chosen to use four articulated booms, even though the system could be considered as overdetermined.

Two locations are considered for positioning the mechanism on the telescope. In Figures 11.3 and 11.4 the position locations are shown.

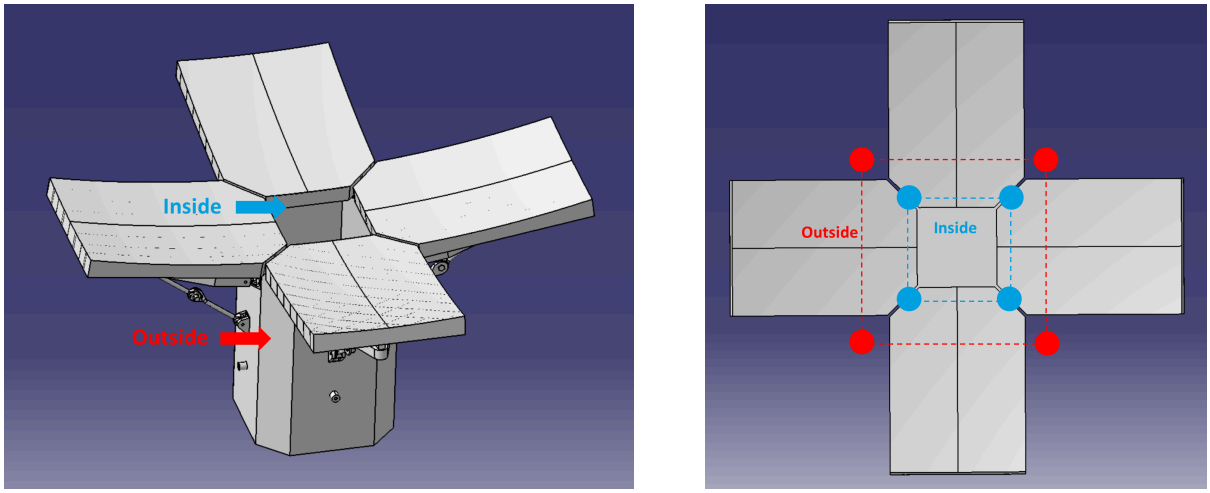

(a) Telescope with primary mirror only **(b)** Top view

Figure 11.3 Position options of deployable mechanism on instrument

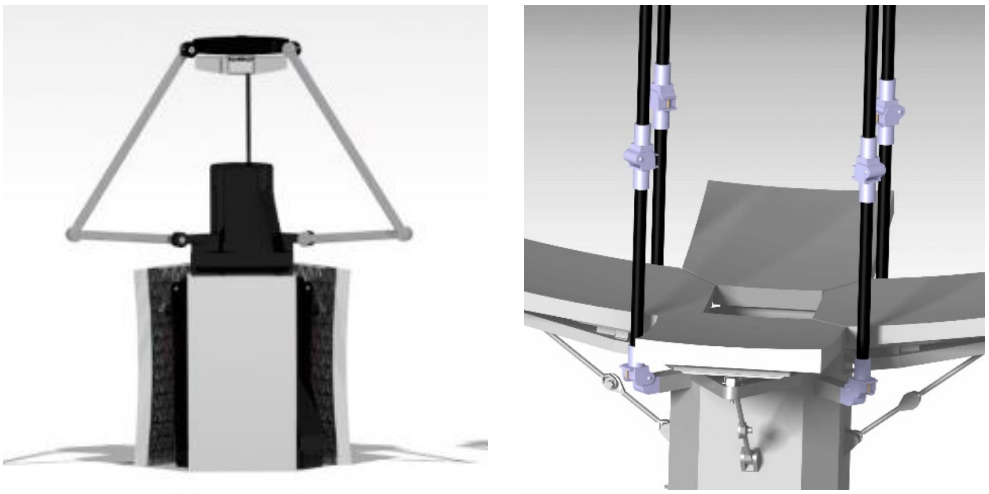

(a) Inside position (original position of the mechanism) [5] **(b)** Outside position

Figure 11.4 Examples of the two position options

Inside The first location is labeled with 'inside'. This location is based on the original design of the DST (Figure 11.4a). The advantage of this position is that the booms can be placed relatively close to each other, resulting in a small attachment structure for the secondary mirror. The arms would have a distance of approximately 30 cm. Also the arms are not connected to the same face as the primary mirror, so the loads are not directly transferred from one mechanism to the other. Due to the higher starting position of the booms, the total length of the booms decreases, which has lots of advantages in terms of positioning accuracy and mass. This has been proven throughout this report. Nonetheless, the starting position of the mechanism has the disadvantage that the stowed length will be larger compared to the 'outside' option. Another big disadvantage is that a certain area of the booms and the mirror will overlap

the mirror, resulting in less incoming light and reducing the performance of the mirror. This is crucial, as the incoming light should be maximized.

Outside To continue on the outside option (Figure 11.4b), this option has the advantage that most of the boom length can be folded along the total body of the telescope, so the stowed length would be lower than the 'inside' option. Also the segments of the primary mirror are located between the booms, so there is no chance of interference with the optical path, due to displacements of the booms. In Figure 11.3b the position of the booms is seen from the top. The gaps between the segments are about 9 mm. Therefore the booms cannot be placed directly along the body of the telescope, as you would need a very thin rectangular cross-section, which will reduce the overall stiffness of the mechanism. To overcome this problem, the booms need to be placed with an off-set with respect to the body, between the corners of the segments. This is shown with red dots in the figure and can be seen in three dimensional in Figure 11.4b. Though, this means that the booms are placed further apart from each other, compared to the other option. This would be about 52 cm. This is not only an increase in the attachment structure of the secondary mirror, but also an increase in the stowed width if the interface plate is rigid. If the interface plate is designed to fold, this issue can be resolved. Placing the arms close to the primary mirror, has the disadvantage that the two systems could interfere with each other. Loads and vibrations can be easily transferred through the body of the telescope. However, the risk of this occurrence is minimal, as the booms and primary mirror are designed to withstand these vibrational loads. Furthermore, a higher boom length is required as the length has to bridge the part between the location of the mechanism and the vertical position of the primary mirror.

Even though the 'outside' position seem to have more disadvantages than the 'inside' position, the outside positioned mechanism can be designed such that the mirror, nor the booms will block the incoming light. This is inevitable with the inside positioned mechanism and therefore the most beneficial position for the mechanism is to be attached on the outside of the instrument. In subsection 11.1.3 the interface design will be further elaborated.

11.1.3 Interface with Secondary Mirror

In subsection 11.1.2, it was concluded that the root of the mechanism should be located on the outer faces of the body of the DST. The most important reason was that the booms would not interfere with the light path, coming from the primary mirror to the secondary mirror. However, at this point another issue is introduced, which is the interface with of the incoming light with the primary mirror. The part of the primary mirror where two segments come together is important for the optical calibration. The secondary mirror needs to be designed such, that the interface plate or the mirror itself blocks the least amount of incoming light as possible on the primary mirror. In Figure 11.3b, it can be seen that there is a small open square, which is connected to four diagonal lines. To make sure that the mirror has a close fit with this gap and the small gaps between the segments, the 'spider' concept is introduced and can be seen in Figure 11.5.

The secondary mirror consist of a circle with a diameter of 282 mm, with thin legs overlapping the 9 mm gaps between the segments of the primary mirror. This would be the optimal shape. However, the structural performance of the shape has not been analyzed in this thesis. In a further stage of the project, an optimal design of the interface plate is required, which both satisfies the calibration requirements and the structural performance of the plate.

Each end of the interface plate is connected to a hinge, which is directly connected to an articulated boom. This is shown in Figure 11.6. The hinges that were designed for the demonstration mission (see chapter 7), can also be used in the full design. Nevertheless, options can be considered to replace these hinges with a rotary hinge as was used in the initial design of the DST. In the current design, the booms cannot be stowed parallel to the body, as the hinges require to be stowed at a certain angle to keep the interface plate of the secondary mirror in position. If a rotary hinge is used, the center line axis of all hinges, is aligned, which allows the boom to fold parallel to the body of the instrument. The situation is

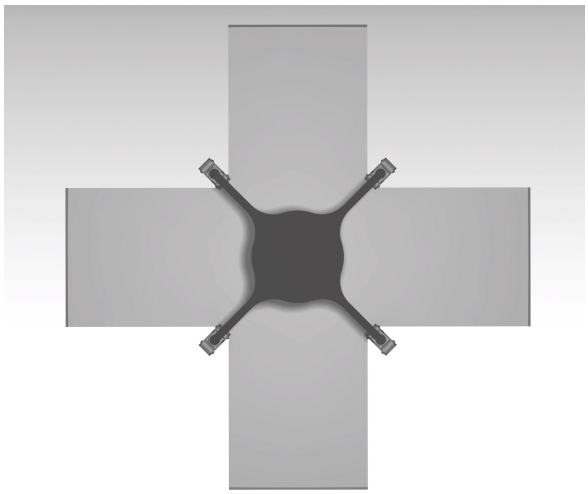

Figure 11.5 Spider concept shape of interface plate of the secondary mirror

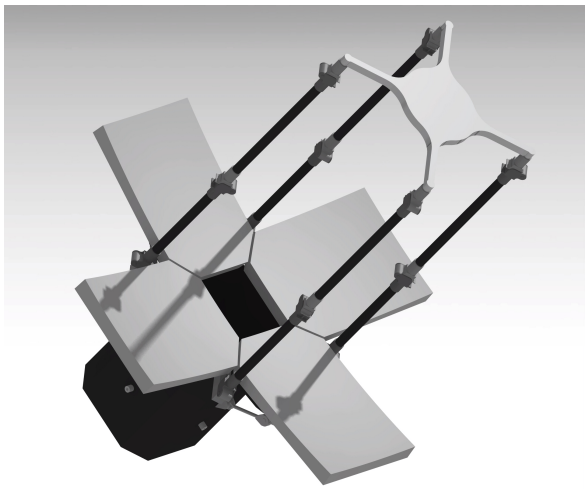

Figure 11.6 Spider concept with articulated booms attached

sketched in Figure 11.7. More research is required on this topic in the future, during the detailed design phase of the hinges.

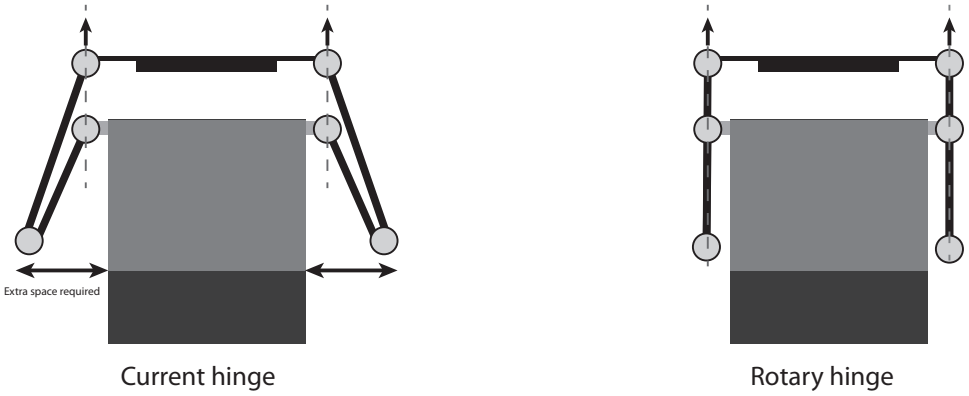

Figure 11.7 Effect of hinge type on stowed configuration

To see the difference of the initial design and the 'spider' concept, the initially designed interface of the secondary mirror is shown Figure 11.8.

Figure 11.8 Original design of secondary mirror [4]

11.2 Natural Frequency Analysis

Using the same analysis method as describe in chapter 9, the natural frequencies of the 'spider' concept are calculated. In Figure 11.9 the six modes of the natural frequency are shown. The deflection from low to high is colored from blue to red, respectively.

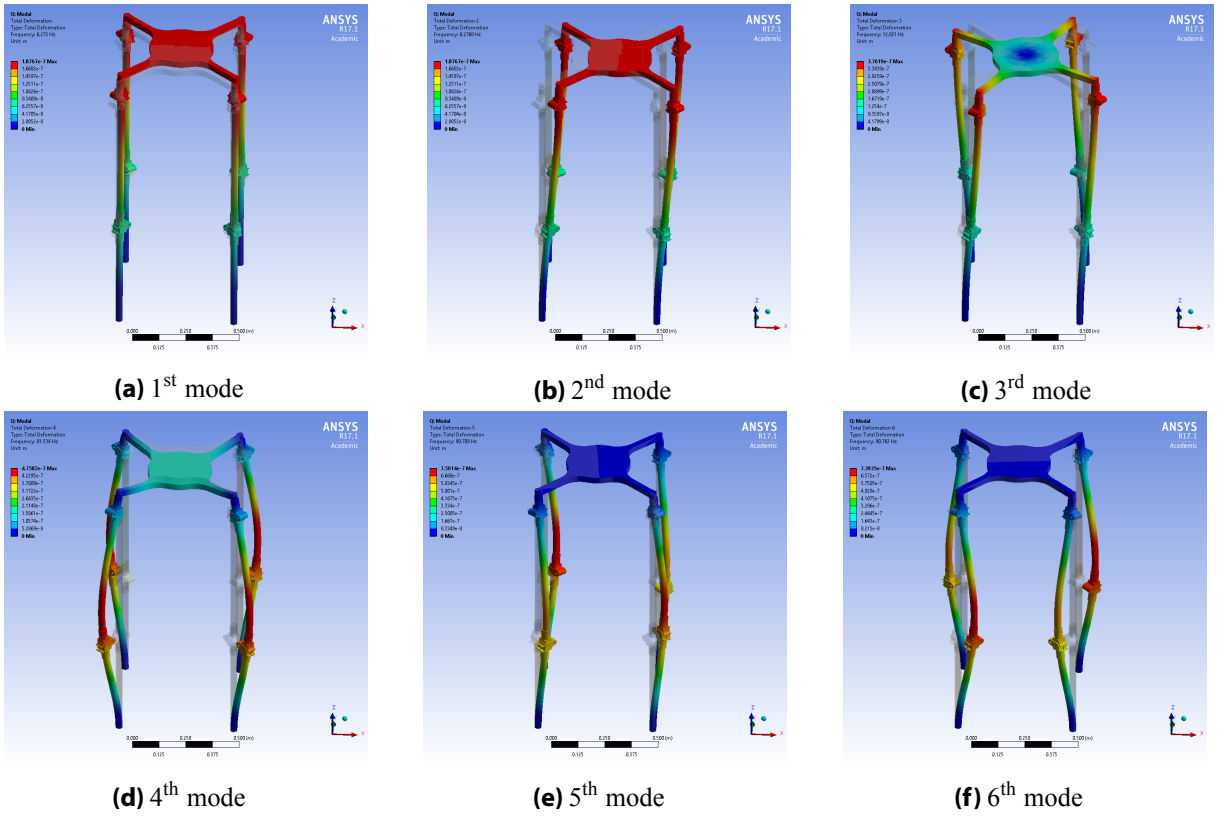

(a) 1st mode **(b)** 2nd mode **(c)** 3rd mode

(d) 4th mode **(e)** 5th mode **(f)** 6th mode

Figure 11.9 Modes of natural frequencies of the system

What can be seen is that the first two modes do have a significant effect on the positioning of the mirror. The first mode (Figure 11.9a) and second mode (Figure 11.9b), cause the mirror to have a decenter. It will move forward and backward or left and right, depending on the reference point. The third mode (Figure 11.9c) causes the mirror to rotate about the vertical axis. The center of the mirror seem to stay in position, a rotation will not affect the light path. However, if the mechanism start to resonate, the light path can become an issue. The fourth mode (Figure 11.9d) shows a small decenter of the secondary mirror.

It can be concluded that these modes are crucial and it has to be made sure during the detailed design phase of the system, that the frequencies of these modes will not be close to potential vibrations in the satellite.

The fifth and sixth mode (shown at the bottom of Figure 11.9) are not crucial for the positioning of the secondary mirror. These modes are more related to the hinges. To have a better understanding of these modes and the effect of the design of the hinges and the mirror, a comparison between four different set-ups is made:

1. The current design, so an Invar mirror with CFRP boom segments and aluminum hinges;
2. An Invar mirror with CFRP boom segments and steel hinges;
3. An aluminum mirror with CFRP boom segments and aluminum hinges;
4. An Invar mirror with CFRP boom segments and aluminum hinges.

In Table 11.1 the natural frequencies of the different concepts are shown. R-M2D-STR-4 (see chapter 2) states that the natural frequency of the deployed mechanism shall be larger than 5 Hz. It can be seen that at this simplified model meets this requirement. Even though these values do not represent the final design, the effects of the design parameters can be evaluated from these results.

Table 11.1 Natural frequencies of full design for variable design parameters

Mode	Frequency [Hz]			
	Current design	Steel hinges	Aluminum mirror	Steel booms
1	6.27	5.96	9.38	7.54
2	6.28	5.97	9.38	7.54
3	12.82	10.58	16.41	17.34
4	81.53	58.74	83.08	80.04
5	90.71	58.91	83.33	86.47
6	90.76	58.95	83.91	86.55

Effect of hinges The effect of the hinges can be analyzed by comparing the second and third columns of Table 11.1. The first and second eigenmode, are not highly affected by changing the material of the hinges. As was already observed in the first part of this analysis, the fourth to the sixth natural frequencies were related to the hinges. This is confirmed by looking at the large differences between these modes for the different configurations.

As the detailed hinge design need to be performed in a later stage of the DST project, the effect of using conceptual hinges need to be investigated as well. To perform this analysis, a representative uniform boom without hinges, but with a similar length has been used to compare the natural frequencies. This can be seen in Table 11.2. The first two natural frequencies can now be confirmed to be dominated by the segments. It can also be concluded that the use of hinges has significant effect on all the other natural. In conclusion, the first two natural frequencies can be predicted with the current design of the boom. For the other natural frequencies a detailed design of the hinges should be taken into account.

Table 11.2 Effect of hinges on natural frequencies

Mode	Frequency [Hz]	
	Without hinges	With hinges
1	5.83	6.27
2	5.83	6.28
3	13.64	12.82
4	89.61	81.53
5	192.49	90.71
6	192.53	90.76

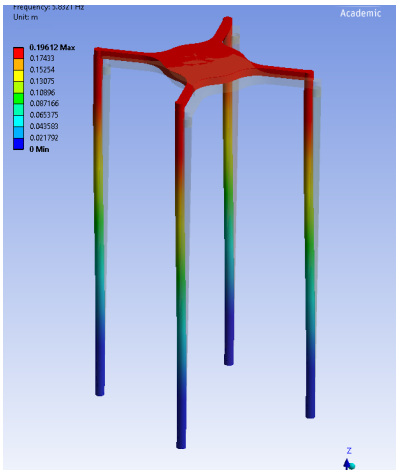

Figure 11.10 Secondary mirror attached to booms without hinges

Effect of mirror Changing the material, thus the mass, of the mirror do not have a significant effect of the overall natural frequencies. This can be observed from the fourth column of Table 11.1. The frequencies are slightly higher, but are still very comparable.

Effect of boom segments The boom segments are made out of CFRP, which was already determined in chapter 5. Even though, it was still interesting to investigate the effect of increasing the mass and stiffness of the boom, by replacing them with steel segments. What can be noticed is that is does not have a significant impact on the first three natural frequencies. It does slightly increase it, however not significantly. The fourth to sixth natural frequencies almost remain the same, as these frequencies were dominated by the hinges as shown.

11.3 Compliance Matrix

In chapter 2, the list of requirements of the DST project were given, including the requirements for the downscaled version. Along the research and design process of the booms, the design was continuously verified with these requirements, to make sure that most of these requirements were fulfilled. Unfortunately, not all requirements could be met. In the following subsections the compliance matrix and the bottlenecks of the system are discussed.

11.3.1 Discussion of Compliance Matrix

In Table 11.3 the compliance matrix of the deployment mechanism for the full DST system design is presented. What can be noticed is that most of the requirements are fulfilled. Two requirements could not

Table 11.3 Compliance matrix for full design

Code	Requirement	Compliant
R-M2D-GEN-1	The mechanism shall extend M2 1.3 m from M1.	✔
R-M2D-GEN-2	The mechanism shall provide structural support for M2.	✔
R-M2D-GEN-3	The total mass of the mechanism shall not exceed 14 kg.	✔
R-M2D-GEN-4	The mechanism shall have a minimum deployment ratio of 2.	✔
R-M2D-GEN-5	The mechanism shall not contain ITAR related components.	✔
R-M2D-GEN-6	The mechanism shall comply with the CSG safety regulations.	✔
R-M2D-STR-1	The deployed mechanism shall have a maximum deflection of 15 µm in the x and y-direction.	✗
R-M2D-STR-2	The deployed mechanism shall have a maximum deflection of 10 µm in the z-direction.	✗
R-M2D-STR-3	The deployed mechanism shall have a maximum twist of 100 µrad about all axes.	✔
R-M2D-STR-4	The deployed mechanism shall have a minimum natural frequency of 5 Hz.	✔
R-M2D-LAU-1	The stowed mechanism shall be able to withstand accelerations up to 30 g.	-
R-M2D-LAU-2	The stowed mechanism shall have a minimum natural frequency of 100 Hz.	-

be checked: R-M2D-LAU-1 and R-M2D-LAU-2. Both of these requirements are related to the stowed mechanism. As no detailed design of the hinges was present, no reliable analyses could be made as it would require a more mature design for the stowed configuration. Components as the HDRM should have been included before one could calculate these values.

However, one of the most crucial requirements of the system, R-M2D-STR-1 and R-M2D-STR-2, could not be met. The analysis in chapter 9, has shown that the deflections due to thermal effects exceed these requirements. It was noted that these effects can be minimized when using aluminum coating or a baffle for the system. If these precautions are taken, these requirements can be met. In conclusion, this research has shown that the given requirements could be met, however more detailed design of the deployable mechanism is required and especially on the thermal design of the system.

11.3.2 System Bottlenecks

During the design process of both booms, some bottlenecks of the deployable mechanism was found. Below a list of the most important bottlenecks can be found:

1. The boom length is crucial for the required optical performance of the DST. As the required boom length decreases, the Strehl ratio of the system decreases as well, causing a significant drop in optical performance;
2. The laminates and the orientation used in the CFRP material can have a big influence on the structural and thermal behaviour of the mechanism. Detailed material analysis is required to ensure the required thermal stability;
3. The maximum allowed stowage volume of the DST has proven to be one of the most crucial bottlenecks of the deployable mechanism. If only a small stowage volume is allowed and a large deployment length is required, some deployable mechanisms cannot be used, such as the articulated boom. In this case, other options should be considered, however this could have a negative impact on the structural performance;
4. The type of hinges used can have a significant impact on the total stowage volume and the thermal behaviour of the system. Therefore a detailed design and analysis of the hinges is required;
5. The thermal behaviour of the boom, as already mentioned, is the largest bottleneck of the whole DST system. If the thermal design of the system is not performed correctly, it could be catastrophic for the optical performance of the DST.

In chapter 14, some proposals are made for future research, to deal with these bottlenecks.

Demonstration Mission 12

This chapter will present a short overview of the integration of the designed articulated boom with the downscaled version of the DST. First an overview of the integrated articulated boom with the downscaled design is shown and finally the compliance matrix is discussed.

12.1 Overview of Design

The downscaled version of the DST, does not look like the full system design of the DST. In consists of a bus, which is connected to the SPS ring, a segmented primary mirror and the deployable boom with the OEB on top. This was already shown in Figure 2.2 of chapter 2. However, in this figure a dummy deployable boom was used to demonstrate the concept.

The deployable articulated boom, which was designed in chapter 7, has replaced the dummy boom and the root hinge has been attached to the bus. In Figure 12.1 the demonstration mission version of the DST is shown, with the stowed configuration of the boom in Figure 12.1a and the deployed configuration in Figure 12.1b.

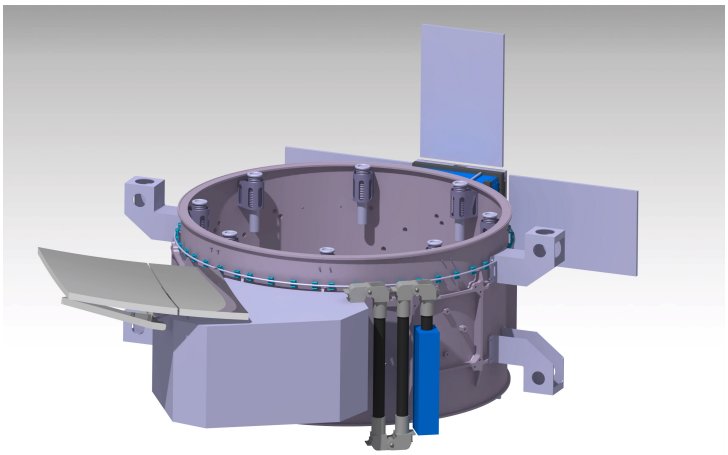

(a) Stowed configuration

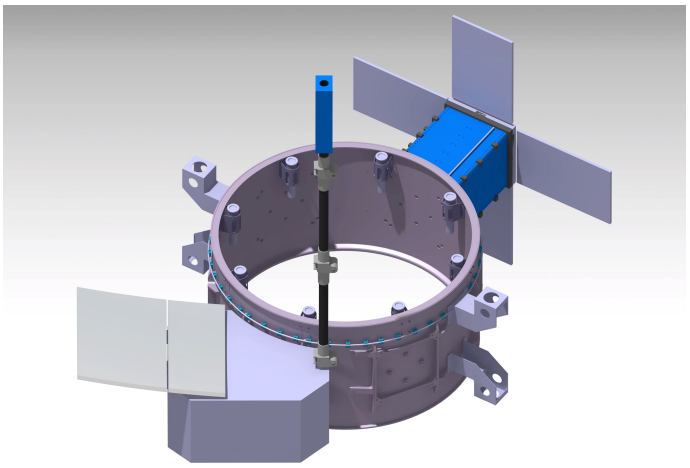

(b) Deployed configuration

Figure 12.1 Articulated boom connected to the downscaled version of the DST

The blue box in the figures, only serves as representative of the OEB, so the shape and the size will be different when a detailed design of the OEB is made. The boom is located on the opposite side of the primary mirror. Due to the shape of the primary mirror, the incoming light will reflect into the opening of the OEB, directly to the collimator optics inside the OEB, as shown in Figure 2.3. What can be noticed in Figure 12.1a, is that the stowed configuration is lower than the SPS ring. This is not directly an issue, as there is room below the SPS ring within the Vega launcher [7]. Another option could be to shift the bus a bit more upwards, so the stowed mechanism would be approximately aligned with the SPS ring at the top and bottom.

In a later stage of the DST project a more detailed design of this downscaled system will be made. However, with the results of this research important conclusions on the deployable mechanisms were drawn. These results and conclusions will form the back-bone for the design of the downscaled version, as well as the full design of the DST. In the following section, the compliance matrix of the downscaled design is discussed.

12.2 Compliance Matrix

The compliance matrix of the downscaled design can be seen in Table 12.1.

Table 12.1 Compliance matrix of the downscaled design

Code	Requirement	Compliant
R-M2D-DS-GEN-1	The downscaled mechanism shall extend the OEB 1.3 m from M1.	✔
R-M2D-DS-GEN-2	The downscaled mechanism shall provide structural support for the OEB.	✔
R-M2D-DS-GEN-3	The total mass of the downscaled mechanism shall not exceed 4 kg.	✔
R-M2D-DS-GEN-4	The downscaled mechanism shall have a minimum deployment ratio of 2.8.	✗
R-M2D-DS-GEN-5	The downscaled mechanism shall be completed before 2019.	-
R-M2D-DS-GEN-6	The downscaled mechanism shall not contain ITAR related components.	✔
R-M2D-DS-GEN-6	The downscaled mechanism shall comply with the CSG safety regulations.	✔
R-M2D-DS-STR-1	The deployed downscaled mechanism shall have a maximum deflection of 15 µm in the x and y-direction.	✗
R-M2D-DS-STR-2	The deployed downscaled mechanism shall have a maximum deflection of 10 µm in the z-direction.	✗
R-M2D-DS-STR-3	The deployed downscaled mechanism shall have a maximum twist of 100 µrad about all axes.	✔
R-M2D-DS-STR-4	The deployed downscaled mechanism shall have a minimum natural frequency of 5 Hz.	✔
R-M2D-DS-LAU-1	The stowed downscaled mechanism shall be able to withstand accelerations up to 30 g.	-
R-M2D-DS-LAU-2	The stowed downscaled mechanism shall have a minimum natural frequency of 100 Hz.	-

The main discussion of the compliance matrix is already performed in chapter 11, for the full design. The three major differences in requirements were the mass, deployment ratio, and schedule. With an expected total mass of 2.46 kg, the articulated boom meets the mass requirement and still has a margin of about 1.5 kg. Nevertheless, the deployment ratio was determined to be 2.7, while the requirement implies that a minimum deployment ratio of 2.8 is required. This could also be seen in Figure 12.1a, as the mechanism is lower than the SPS ring. Nevertheless, this requirement can be easily met when the articulated boom will be optimized during the detailed design process, so it is expected that this will be resolved.

Currently, nothing can be determined about the schedule, as there are multiple factors of which this is dependent on. However, looking at the complexity of the system and the TRL of articulated booms for astrophysics missions, it can be expected that this requirement will be met.

Finally, the requirements which could not be met were the crucial structural requirements, due to the thermal effects of the articulated boom. As already discussed, with the use of a baffle or aluminum coating, this issue might be resolved. However, a detailed thermal analysis is required in the future to provide more reliability to the designed system.

V

Conclusions & Recommendations

Conclusions 13

This thesis has provided an answer to the research question: *"What is the optimal deployable structure for the extension of the secondary mirror of the DST project, in terms of positioning accuracy, mass, and deployment ratio and how can this be integrated in the system design?"*. In order to find an answer to the research question, the research project was broken down into multiple work packages. With the use of the results of each work package, the research question was answered and the objective was met.

Technologies One of the first processes of the research project was to identify the possible technologies for the deployment of the secondary mirror. Six commonly used deployable structures in space flight were found: articulated booms, coilable booms, SMC booms, telescopic booms, inflatable booms, and deployable truss structures. Each of these technologies have shown potential solutions to solve the challenge of designing the deployable structure for the secondary mirror of the DST. Based on the deployment accuracy, stability, feasibility, deployment ratio, TRL, and the mass of the deployable structures, a preliminary trade-off was performed. The results of this trade-off did quite meet the expectations. However, it was not expected that the CTM boom, would end with one of the highest scores. The highest scoring deployable structure was the articulated boom, which was expected as they are commonly used as deployable structures in astrophysics missions.

Materials Next to the technology selection, a trade-off for the material selection was performed. The materials used for this trade-off were aluminum, stainless steel, titanium, Invar and CFRP. Using the density, Young's modulus, CTE, cost, and shear modulus of each material, it was found that CFRP was the best option to use as main material for the design process of the articulated boom and the CTM boom. With the use of the classical lamination theory, multiple lay-up configurations of a CFRP laminate were analyzed with respect to the resulting mechanical properties of the laminate. It was found that a lay-up configuration of $[0/0/\pm 45]_s$, had the optimal mechanical properties for the design of the articulated boom and the CTM boom. This was both based on the analysis in the report, as well as on other research projects in the literature. However, in a later stage of the DST project a detailed material analysis is required, including experimental results, to verify this lay-up configuration.

Optimal Boom Length Before both booms were designed, it was concluded that the loads on the boom during the demonstration mission could be considered as the worst case scenario, in comparison with the full system design. Therefore, the design process of the booms was based on the single deployable structure of the demonstration mission. The extension length of the deployable mechanism was found to be 1.3 m. This length was found through a detailed trade-off between the optical and the mechanical performances of the DST. This length was used in both the full design, as well as in the downscaled design.

Articulated Boom The design process of the research project, was started with the design of the articulated boom. The articulated boom consisted of three CFRP tubular segments with hinges at the root and two in the middle. At the top of the boom a dummy mass was attached, which served as a representative of the OEB. The segments of the articulated boom had a thickness of 1 mm and an outer diameter of 3.3 cm, resulting in a mass of 69 g per segment. This sizing was performed according to an iterative process, in which the outer diameter was varied until the required stiffness was found. The aluminum hinges consisted of two hinge parts, connected with a bolt and a torsional spring. These hinges were estimated to have a mass of 490 grams, which was close to initially estimated mass of 500 g. To prevent the articulated boom from exceeding the alignment budget, it was determined that a locking mechanism and an end stop are required in the hinges, as it was shown that small angular deflections could cause significant deflections at the tip of the boom. Due to the stored angular energy in the hinges, a damping system is required that no end-shock is present during the deployment. With a total mass of 2.46 kg, including a

contingency factor, it could be concluded that the redesigned articulated boom had a significant improvement in terms of mass compared to the initial designed articulated booms of the DST. Furthermore, the articulated boom had a deployment ratio of 2.7, with a stowage volume of 6111 cm^3.

CTM Boom Parallel to the articulated boom design process, the CTM boom was designed. A CTM boom can be considered as two halves with an Omega-like cross-section. As the cross-section of a CTM boom is symmetrical about two axes, the full cross-section of the boom was designed with the eleven shape parameters of a quarter of the boom. As for the articulated boom, the CTM boom design was performed according to an iterative process as well. During the iteration, two shape parameters were iterated until the optimal shape was found, which satisfied the stiffness requirements. It was shown in this process that there is a relation between the deflection and the total mass of the boom. The lower the mass of the boom, the higher the deflection becomes. The optimal boom shape had a mass of only 145 g. From the literature review it was expected that the total mass of the boom would be low, which was confirmed with this result. Nevertheless, to provide the required stiffness, stability and allow the boom to deploy and retract, a HDRM was required. This HDRM, consisted of rollers, a storage drum, an electric motor, and support structures had an estimated mass of 1.95 kg, which was 13 times higher than the mass of the boom itself. Therefore the HDRM was proven to be the bottleneck for potential mass constraints. The total mass of the CTM boom mechanism, was estimated to be 3.33 kg, including the contingency factor. Despite of the high mass, the mechanism had a stowage volume of 5425 cm^3 and a deployment ratio of 4.2.

Analyses Both designs have been analyzed in ANSYS, using static, harmonic, modal, and thermal analyses. The assumption was made that both booms are fully clamped at the root. It was found that the deflections due to (quasi-)static micro-gravity conditions, were minimal and did not reach the micrometer range. This was the case for both booms. The articulated boom had less deflection along the z-axis due to the extra stiffness of the aluminum hinges, however when the gravity was pointing in the y-direction, the CTM boom had less deflection due its higher moment of inertia about that axis. Nevertheless, the deflections caused by vibrations at the natural frequency, have shown to be critical. Therefore, the natural frequencies of the subsystems need to be spread over the frequency domain, to prevent unwanted interference with the AOCS or other components of the satellite. The most crucial results were found in the thermal analyses. The deflection limits along multiple axes were exceeded, calculated over one orbital period. The highest maximum and lowest minimum temperatures were found in the CTM boom, however the largest deflections caused by these temperature distributions were found in the articulated boom. This was most probably caused by the hinges. To solve the thermal issue, it was proposed to use a baffle around the telescope, to apply aluminum coating on the booms, or use alternative materials as Invar for the hinges of the articulated boom. Applying aluminum coating showed significant positive impact on the calculated deflections.

Optimal Deployable Structure Using the results of the analyses, the boom properties and risks of both deployable structures, a final trade-off was made. The CTM boom mechanism had shown a better thermal stability, had a higher deployment ratio, and was able to have (actively) controlled deployment. Nevertheless, the articulated boom had better scores on the most crucial parameters, such as risk, stiffness, which is directly related to the positioning accuracy, and surprisingly the mass. Furthermore, the complexity of the system was lower than the CTM and literature had shown that articulated booms are more mature in terms of TRL. It could be concluded that the articulated boom is the optical deployable structure for the deployment mechanism of the secondary mirror. Not in terms of deployment ratio, which was one of the key trade-off parameters of the research question, however in terms of positioning accuracy and mass. In comparison with the initially designed articulated booms, the boom had significant improvement in terms of mass. At the start of the literature review, the CTM boom looked very promising: low mass, high deployment ratio, and the required stiffness could be met through an iteration process. However, with this detailed design and analysis process, it was found that the HDRM was the bottleneck in the system. Due to the demanding alignment budget, the HDRM needed to be designed such that it had a major impact on the complexity, mass and risks.

Interface with DST As the designed articulated boom was designed for the worst case scenario, the boom configuration of the downscaled version could directly be implemented in the full version of the DST, apart from the amount of hinges and segment length. The mounting location of the mechanism was determined to be on the outside of the instrument's body, in order to prevent interference with the light path between the primary mirror and the secondary mirror. A proposal was made to use a so-called 'spider' concept for the secondary mirror. This name originates from the shape of the secondary mirror and the connection to the articulated booms. Analyses have shown the impact of hinge design, boom material, and mirror material on the natural frequency of the full DST system.

Conclusion This thesis has formed the backbone of the design of the deployable mechanism of the secondary mirror. The research has treated the available technologies, the most suitable materials and their properties, elaborate preliminary boom designs, analyses, bottlenecks, and several trade-offs were made. With the results of this thesis, the detailed design process of the deployable mechanism for the secondary mirror can be continued, to reach the final objective: designing a compact, lightweight and most of all, an accurate deployable structure for the extension of the secondary mirror of the DST.

Recommendations 14

Throughout the research, multiple assumptions and simplification have been made and also some issues have revealed, which need to be taken into account during future research and design of the deployable mechanism for the secondary mirror.

Detailed Design During the design of the articulated boom, the hinges were designed on a conceptual base. Multiple simplifications have been used and no calculation of the actual performance of the hinges was done. In a future step, a detailed design of the hinges should be made including effects of the end stop, the locking mechanism, and the spring. The stresses in the spring should be calculated, with the knock down factor. Also the effects of actual preloading of the hinges need to be further explored. Furthermore, the assumption was made that the booms were fully clamped during the analysis. Nevertheless, to ensure this clamping, the root hinge requires a proper design, ensuring full clamping of the boom. Else this can have a significant impact on the structural performance. Furthermore, due to the internally stored angular energy, the articulated boom requires a damping system. This damping system needs to be designed in detail for the amount of energy stored, to prevent the boom from having a high end-shock. All these changes will eventually have influence on the mass, however with the contingency factor used of 20%, it is not expected that the current estimation will be surpassed significantly. Next to the design of the hinges, a reconsideration of the material should be made if the thermal stability is not met when the hinges are made out of aluminum. Moreover, a detailed lay-up design of the CFRP material should be made, including all the effects and internal stresses caused by multiple factors. Actual experiments are required for this process. In the current full design of the DST, four booms are used which means that the boom is statically overdetermined. The amount of booms should be rechecked and the effects of an overdetermined system should be researched as well. Finally, a detailed analysis on the natural frequency and the frequency response is required. To prevent unwanted interference with the AOCS or other components of the satellite, the natural frequencies of the subsystems need to be spread over the frequency domain. Once the detailed design is finished, the stowed configuration of the deployment mechanism requires to be analyzed for launch conditions.

Analyses During the analysis with ANSYS, it was found that there is a meshing limit as a student version was used. For a conceptual design, this is not crucial, however when a detailed design is made, in which multiple components are added, the meshing limit can have crucial effects on the results. Therefore, it is recommended to use a full licensed ANSYS software package in order to provide more reliability to the results. Another important setting, was the contacts settings. If a geometry is loaded into ANSYS, the contacts between the components are automatically generated and set to 'bonded'. First it has to be decided whether the connection is indeed bonded or has to be set-up as, for example, 'frictionless'. Also other parameters in the contacts settings can have influence on the results. Most importantly, is that the automatically generated contacts are checked and corrected if needed. During the analysis of both booms, wrong automatically generated contacts caused the booms to have completely wrong results in comparison with the analytical values. Once these contacts were manually adjusted, correct values were found. Therefore it is also always recommended to use analytical values to validate the results of ANSYS, if possible, before continuing with the full analysis.

Thermal Instabilities During the thermal analyses, it was found that the alignment budget was exceeded with a significant amount caused by the temperature distributions along the boom. As shown, aluminum coating or using a baffle could be an option of solving this problem. Also, as already earlier mentioned, a proper analysis of the CFRP fiber lay-up is required, in order to reduce the CTE which was currently used in this design. In conclusion, a detailed thermal analysis is required in order to adjust the design to meet the required alignment budget.

Verification The analyses made in this report were verified with analytical results, where possible. However, experimental results are essential in order to validate these results. A prototype is therefore required. Once the prototype is built, the design can be verified by performing experiments. During the literature research of deployable booms, interesting experiments were found in order to measure the positioning accuracy and to verify that these accuracies stay within the given optical tolerances. The first experiment proposal was based on the measurement set-up which was used for the Deployable Petal Telescope (DPT) [76]. This experiment consisted of an electronic autocollimator, which was used to measure the tilt of the secondary mirror, and precision micrometers, which were used to measure the despace and decenter of the secondary mirror. The interesting part of this experiment is the use of an autocollimator. An autocollimator is an optical instrument whit a very high sensitivity and can therefore measure small angular displacements [77]. The autocollimator used in this experiment is a digital autocollimator. This type of autocollimator makes use of a photo-detector in order to detect the reflected beam. It has the advantage that very small angular displacements can be measured and directly translated to digital signals. The other experiment was developed by Feng *et al.* [78]. The experiment makes use of three laser diodes, three 2-D PSDs, and three mirrors. The basic idea of this experiment is to measure the position of secondary mirror before stowing and then compare it to the position after the mirror has been stowed and deployed. To measure the position, the lasers are pointed to the mirrors which are attached to the secondary mirror. These mirrors reflect the light of the lasers back to the PSDs, which will give a value for the position of the laser. Once both measurements have been performed, the values of the initial measurements will be subtracted from the post-deployment measurements and will result in the displacements in each axis. In the same manner, the angular displacements are calculated. This experiment is simple and accurate, and should therefore also be considered as an experiment for the DST project.

On-Ground Testing Unfortunately, the problem with both proposed experiments is that, as it is performed on Earth, it is influenced by gravity. Gravity can have major impacts on the outcome of the positioning accuracies of the deployable structures. If no buckling occurs, one can assume that the measured alignment errors will be reduced with a factor 10^{-6} once used in space. An option could be by testing the prototype in micro-gravity environment during, for example, a parabolic flight. Nevertheless, arranging a parabolic flight for such an experiment is very expensive. A less expensive solution to experience micro-gravity is developed by DLR, Institute of Structural Mechanics [68]. The tips of deployable booms can be attached to helium filled balloons, in order to simulate the micro-gravity conditions. As for certain types of deployable booms, the mass changes over the deployment time, the balloons are designed to adjust the lift. This is done by attaching remotely controlled pumps to the balloons which drain water from small tanks.

VI

Bibliography & Appendices

Bibliography

[1] Space Foundation, *The Space Report: The Authoritative Guide to Global Space Activity,* (2014).

[2] L. Puig, A. Barton, and N. Rando, *A review on large deployable structures for astrophysics missions,* Acta Astronautica **67**, 12 (2010).

[3] T. Segert, B. Danziger, D. Gork, and M. Lieder, *Dobson Space Telescope - Development of an Optical Payload of the Next Generation,* in *Proceedings of the 6th International Conference on Space Optics* (ESA ESTEC, 2006).

[4] D. Dolkens, *A Deployable Telescope for Sub-Meter Resolutions from MicroSatellite Platforms*, Master's thesis, Delft University of Technology (2015).

[5] D. Dolkens and H. Kuiper, *A Deployable Telescope for Sub-Meter Resolutions from MicroSatellite Platforms,* in *Proceedings of the International Conference on Space Optics* (2014).

[6] D. Robinson and R. McClelland, *Mechanical Overview of the International X-Ray Observatory,* in *Proceedings of the Aerospace Conference, 2009 IEEE* (2009).

[7] J. van der Ploeg, H. Cruijssen, J. de Kam, and C. Hofkamp, *Concept study of Stackable Platform Structure,* Confidential Report (2014).

[8] B. van Putten, *Design of the Deployment Mechanism for the Primary Mirror Elements of a Deployable Space Telescope*, Master's thesis, Delft University of Technology (2017).

[9] J. Choi, D. Lee, K. Hwang, and B. Kim, *A Mechanism for a Deployable Optical Structure of a Small Satellite,* International Journal of Precision Engineering and Manufacturing **16** (2015).

[10] S.-Y. Lee, G. Kim, Y.-S. Lee, and G.-H. Kim, *Optical Design and Tolerance Analysis of a New Off-Axis Infrared Collimator,* International Journal of Precision Engineering and Manufacturing (2014).

[11] Tele-Optics, *Misalignment and forced surface deformations,* Available Online <http://www.telescope-optics.net/induced2.htm> (accessed 20 February 2016) (2006).

[12] A. Calvi, *Spacecraft Loads Analysis: An Overview,* Lecture Slides. University of Liege Satellite Engineering Class. Available Online <http://www.ltas-vis.ulg.ac.be/cmsms/uploads/File/CALVI_LIEGE_2013_Students.pdf> (accessed 10 February 2017) (2011).

[13] *Ariane 5 User's Manual*, Arianespace, issue 5 revision 2 ed. (2016).

[14] *Vega User's Manual*, Arianespace, issue 4 revision 0 ed. (2014).

[15] G. Vetrov and B. Raushenbakh, eds., *S. P. Korolev and His Affairs: Light and Shadow in the History of Cosmonautics: Selected Works and Documents* (Nauka, 1998).

[16] G. Tibert, *Deployable Tensegrity Structures for Space Applications*, Tech. Rep. (Royal Institute of Technology, 2002).

[17] M. Macdonald and V. Badescu, eds., *The International Handbook of Space Technology* (Springer, 2014).

[18] Z. You and N. Cole, *Self-locking bi-stable deployable booms,* in *Proceedings of the 47th AIAA/ASME/ASCE/AHS/ASC Structures, Structural Dynamics, and Materials Conference* (2006).

[19] J. Christian, S. Jayaram, and M. Swartwout, *Feasibility of a Deployable Boom aboard Picosatellites for Instrumentation and Control Purposes,* in *Proceedings of the Aerospace Conference, 2012 IEEE* (2012).

[20] C. Underwood, S. Pellegrino, V. Lappas, C. Bridges, and J. Baker, *Using CubeSat/micro-satellite technology to demonstrate the Autonomous Assembly of a Reconfigurable Space Telescope (AAReST),* Acta Astronautica **114** (2015).

[21] National Aeronautics and Space Administration (NASA), *The James Webb Space Telescope: Frequently Asked Questions (FAQ),* Available Online <http://jwst.nasa.gov/faq.html> (accessed 1 March 2016).

[22] M. Bavdaz *et al.*, *IXO system studies and technology preparation,* in *Optics for EUV, X-Ray, and Gamma-Ray Astronomy IV* (2009).

[23] Y. Nakamura *et al.*, *Vitalization of japanese small satellite community through publicity-offered piggy-back launch,* in *Proceedings of the Symposium on Small Satellite Systems and Services (4S)* (2010).

[24] M. Komatsu and S. Nakasuka, *University of Tokyo Nano Satellite Project "PRISM",* Transactions of the Japan Society for Aeronautical and Space Sciences, Space Technology Japan **7** (2009).

[25] T. Murphey, *Overview of Deployable Structures,* in *Proceedings: Prepared for AIAA Structures TC* (2008).

[26] S. Pellegrino, ed., *Deployable Structures* (Springer, 2001).

[27] D. Rohweller, *Qualification of the Inflatable Sunshield in Space (ISIS) mast,* in *Proceedings of the 36th Aerospace Mechanisms Symposium* (2002).

[28] M. Wylie, P. Duffy, D. Vather, J. Keegan, and S. Curran, *A Novel Telescopic Boom Deployment System for Use in Upper Atmosphere Research,* in *Proceedings of the International Manufacturing Conference* (2010).

[29] M. Lawton, *Oxford Space Systems AstroTube Max Boom,* Available Online <https://vimeo.com/141426125> (accessed 5 August 2016) (2015).

[30] M. Schenk, A. Viquerat, K. Seffen, and S. Guest, *Review of Inflatable Booms for Deployable Space Structures: Packing and Rigidization,* Journal of Spacecraft and Rockets (2014).

[31] D. Gross and D. Messner, *The Able Deployable Articulated Mast - Enabling Technology for the Shuttle Radar Topography Mission,* in *Proceedings of the 33rd Aerospace Mechanisms Symposium* (1999).

[32] E. Ramirez, *Shuttle Radar Topography Misson: MAST,* Available Online <http://www2.jpl.nasa.gov/srtm/mast.html> (accessed 16 April 2016) (2016).

[33] M. Bowden and M. Benton, *Design of deployable-truss masts for Space Station,* in *Proceedings of the AIAA, AHS, and ASEE, Aerospace Design Conference* (1993).

[34] N. Friendman and A. Ibrahimbegovic, *Overview of Highly Flexible, Deployable Lattice Structures Used in Architecture and Civil Engineering Undergoing Large Displacements,* YBL Journal of Built Environment **1** (2013).

[35] M. Legault, *Self-Deployable, Composite Satellite Boom,* High-Performance Composites **19** (2011).

[36] P. Fortescue, G. Swinerd, and J. Stark, eds., *Spacecraft Systems Engineering*, 4th ed. (Wiley-Blackwell, 2011).

[37] R. Romeo *et al.*, *Ultra-lightweight, Deployable 1m-Class Optical Telescope for SSA Applications ,* in *Proceedings of the Advanced Maui Optical and Space Surveillance Technologies Conference* (2007).

[38] R. Hertzberg, *Deformation and Fracture Mechanics of Engineering Materials*, 4th ed. (Wiley, 1995).

[39] J. Gere, *Mechanics of Materials*, sixth ed. (Thomson-Engineering, 2003).

[40] E. Moritz and S. Haake, eds., *The Engineering of Sport 6*, Vol. 3 (Springer, 2006).

[41] M. Weber, *Handbook of Optical Materials* (CRC Press, 2002).

[42] D. Roylance, *Material Properties,* Appendix. Department of Materials Science and Engineering. Massachusetts Institute of Technology. Available Online <http://web.mit.edu/course/3/3.11/www/modules/props.pdf> (accessed 1 February 2017) (2000).

[43] H. Mann, *Deflections and Slopes of Beams,* Available Online <http://virtual.cvut.cz/beams/> (accessed 20 September 2016) (2005).

[44] A. Thakur, *Twelve Viva Questions on Columns and Struts,* Available Online <http://engineering.myindialist.com/2015/twelve-viva-questions-on-columns-and-struts/#.V9aXRZOLTyL> (accessed 3 August 2016) (2015).

[45] R. Beardmore, *Natural Frequencies to Traverse Vibrations,* Available Online <http://www.roymech.co.uk/Useful_Tables/Vibrations/Natural_Vibrations.html> (accessed 10 January 2017) (2013).

[46] V. Sacek, *6.5. Strehl ratio,* Notes on amateur telescope optics, Available Online <http://www.telescope-optics.net/Strehl.htm> (accessed 25 November 2016) (2006).

[47] S. Stallinga, *Strehl ratio for focusing into biaxially birefringent media,* Journal of the Optical Society of America A **21** (2004).

[48] F. Fang, X. Zhang, A. Weckenmann, G. Zhang, and C. Evans, *Manufacturing and measurement of freeform optics,* CIRP Annals - Manufacturing Technology **62** (2013).

[49] T. Kubiak, *Static and Dynamic Buckling of Thin-Walled Plate Structures* (Springer, 2013).

[50] D. Roylance, *Laminated Composite Plates,* Handout. Department of Materials Science and Engineering. Massachusetts Institute of Technology. Available Online <http://ocw.raf.edu.rs/courses/materials-science-and-engineering/3-11-mechanics-of-materials-fall-1999/modules/laminates.pdf> (accessed 1 February 2017) (2000).

[51] Siemens PLM Software, *Lesson 7: 2D Laminate Theory,* Available Online <http://oss.jishulink.com/upload/201605/1463718705043_Lesson_7_Laminate_Theory.pdf> (accessed 1 February 2017) (2013).

[52] M. Choças Rosado, *Mechanical design and analysis of a deployment mechanism for low frequency dipole antenna*, Master's thesis, Instituto Superior Técnico (2015).

[53] A. Maji, M. Harris, D. Garcia, and B. deBlonk, *Feasibility Assessment of Deployable Composite Telescope,* Journal of Aerospace Engineering **24** (2011).

[54] P. Joyce, *Common Lay Common Lay-up Terms and up Terms and Conditions,* Lecture Slides. United States Naval Academy. Available Online <https://www.usna.edu/Users/mecheng/pjoyce/composites/Short_Course_2003/7_PAX_Short_Course_Laminate-Orientation-Code.pdf> (accessed 1 February 2017) (2003).

[55] P. Mohite, *Lecture 16: Introduction to Classical Plate Theory,* Online Course. Composite Materials and Structures. Department of Aerospace Engineering. Indian Institute of Technology Kanpur. Available Online <http://nptel.ac.in/courses/101104010/downloads/Lecture16.pdf> (accessed 1 February 2017) (2014).

[56] C. Sickinger, L. Herbeck, T. Strohlein, and J. Torrez-Torres, *Lightweight Deployable Booms: Design, Manufacture, Verification, and Smart Materials Application,* in *Proceedings of 55th International Astronautical Congress of the International Astronautical Federation* (2004).

[57] R. Irwin, J. Vander Veen, E. Buchner-Santos, and C. Dharan, *Low-Mass Deployable Spacecraft Booms,* in *Proceedings of the AIAA SPACE 2010 Conference & Exposition* (2010).

[58] A. Cherouat and J. Billoët, *Mechanical and numerical modelling of composite manufacturing processes deep-drawing and laying-up of thin pre-impregnated woven fabrics,* Journal of Materials Processing Technology **118** (2001).

[59] Jiangxi Lihuan Spring Co., Ltd, *Torsion Spring,* Available Online <http://sci.esa.int/ixo/45348-spacecraft/?fbodylongid=2111> (accessed 25 March 2017) (2009).

[60] A. Beek, van, *Calculator for Torsion springs,* Available Online <http://www.werktuigbouw.nl/calculators/t14_4.htm> (accessed 10 February 2017).

[61] Y. Yamada, *Materials for Springs* (Springer, 2007).

[62] M. Lake and M. Roman Hachkowski, *Mechanism design principle for optical-precision, deployable instruments,* in *Proceedings of the 41st AIAA/ASME/ASCE/AHS/ASC Structures, Structural Dynamics, and Materials Conference* (2000).

[63] M. Kroon, G. Borst, M. Grimminck, M. Robroek, and F. Geuskens, *Articulated Deployment System For Antenna Reflectors ,* in *16th European Space Mechanisms and Tribology Symposium* (2015).

[64] J. Augustijn, M. Grimminck, E. Bongers, T. Konink, and J. Koning, *Development of Non Explosive Low Shock (NELS) Hold-down and Release System,* in *Proceedings of 16th ESMATS* (2015).

[65] Glenair, Inc, *Series 06: Hold-Down Release Mechanism Technology,* Available Online <http://cdn.glenair.com/capability/pdf/l/hold_down_release_mechanism_technology.pdf> (accessed 10 February 2017 (2014).

[66] Southern Cross University, *Risk Management,* Available Online <http://scu.edu.au/risk_management/> (accessed 10 April 2017).

[67] M. Leipold, H. Runge, and C. Sickinger, *Large SAR Membrane Antennas with Lightweight Deployable Booms,* in *Proceedings of the 28th ESA Antenna Workshop on Space Antenna Systems and Technologies* (2005).

[68] L. Herbeck, M. Eiden, M. Leipold, C. Sickinger, and W. Unkenbold, *Development and Test of Deployable Ultra-Light Weight CFRP Boom for a Solar Sail,* in *Proceedings of the European Conference on Spacecraft Structures, Materials and Mechanical Testing* (2000).

[69] F. Hakkak and S. Khoddam, *On calculation of preliminary design parameters for lenticular booms,* Proceedings of the Institution of Mechanical Engineers – Part G **221** (2007).

[70] Z. Chu and Y. Lei, *Design theory and dynamic analysis of a deployable boom,* Mechanism and Machine Theory **71** (2014).

[71] S. Michael, *On-Orbit Space Shuttle Inspection System Utilizing an Extendable Boom*, Master's thesis, University of Maryland (2004).

[72] T. Schmidt, K. Seifart, F. Burger, and J. Eder, *In orbit bonding (iob) of long deployable structures,* in *Proceedings of the 10th European Space Mechanisms and Tribology Symposium* (2003).

[73] Z. Chu, Y. Lei, and D. Li, *Dynamics and robust adaptive control of a deployable boom for a space probe,* Acta Astronautica **97** (2014).

[74] S. Rickman, *Introduction to On-Orbit Thermal Environments,* Thermal and Fluids Analysis Workshop. Available Online <https://tfaws.nasa.gov/files/On-Orbit_Thermal_Environments_TFAWS_2014.pdf> (accessed 25 October 2016) (2014).

[75] I. Martinez, *Properties of solids,* Available Online <http://webserver.dmt.upm.es/~isidoro/dat1/eSol.pdf> (accessed 2 February 2017) (2017).

[76] J. Champagne, S. Hansen, and T. Newswander, *CubeSat Image Resolution Capabilities with Deployable Optics and Current Imaging Technology,* in *Proceedings of the 28th Annual AIAA/USU Conference on Small Satellites* (2014).

[77] Micro-Radian Instruments, *Principles of Operation,* Available Online <http://www.micro-radian.com/Principles.html> (accessed 20 April 2016) (2014).

[78] X. Feng, C. Li, and C. Zhao, *New measurement of the alignment of the deployable telescope,* in *Proceedings of the 6th International Symposium on Advanced Optical Manufacturing and Testing Technologies: Optical Test and Measurement Technology and Equipment* (2012).

Appendix of MATLAB Codes

A

This appendix provides the MATLAB codes used in this thesis.

A.1 Classic Laminate Theory

```
% Classic Laminate Theory (J.W. Lopes Barreto)

clear all, clc, close all

% Individual Mechanical Properties

% rho_c = rho_m*V_m + rho_f*V_f;  % [kg/m^3] Density
% E_L = E_m*E_m + E_f*E_f;        % [Pa] Longitudinal Young's Modulus
% E_T = 1/(V_f/E_f+V_m/E_m);      % [kg/m^3] Transverse Young's Modulus
% G_f = E_f/(2*(1+v_f));          % [kg/m^3] Fibre Shear Modulus
% G_m = E_m/(2*(1+v_m));          % [kg/m^3] Matrix Shear Modulus
% G_LT = 1/(V_f/G_f+V_m/G_m);     % [kg/m^3] Shear Modulus
% v_LT = V_f*v_f + V_m*v_m;       % [kg/m^3] Poission Ratio LT
% v_TL = E_T/E_L*v_LT;            % [kg/m^3] Poission Ratio TL

display('Lamina Properties')
disp('-----------------------')

E_1 = input('E_1 (Longitudinal Youngs Modulus) [GPa]: ')*1e9;        % [Pa] ...
    Longitudinal Young's Modulus
E_2 = input('E_2 (Transverse Youngs Modulus) [GPa]: ')*1e9;      % [Pa] ...
    Transverse Young's Modulus
G_12 = input('G_12 (Shear Modulus) [GPa]: ')*1e9;      % [Pa] Shear Modulus
v_12 = input('v_12 (Poission Ratio): ');       % [-] Poission Ratio LT
v_21 = E_2*v_12/E_1;            % [-] Poission Ratio TL

% Local matrix Q

Q = [   E_1/(1-v_12*v_21)          (E_1*v_21)/(1-v_12*v_21)     0;...
        (E_2*v_12)/(1-v_12*v_21)    E_2/(1-v_12*v_21)           0;...
        0                           0                           G_12];

    % Ply information
display(' ')
n = input('Enter the number of plies: ');
A = zeros(3,3);
B = zeros(3,3);
D = zeros(3,3);
z = [0];

% Store Ply Data
for i = 1:n
    display(' ')
    display(sprintf('Layer %i properties',i))
    disp('-----------------------')
    theta(i) = input('Ply angle [deg]: ');
    t_ply(i) = input('Ply thickness [mm]: ')*1e-3;
    display(' ')
end
```

```
% Calculate ply thickness
h = sum(t_ply);
z = [-h/2];

for i = 1:n

    z(i+1) = z(i)+t_ply(i);

    T_o_inv = [ cosd(theta(i))^2             sind(theta(i))^2             ...
        -2*cosd(theta(i))*sind(theta(i));...
                sind(theta(i))^2             cosd(theta(i))^2             ...
                    2*cosd(theta(i))*sind(theta(i));...
                cosd(theta(i))*sind(theta(i))  -cosd(theta(i))*sind(theta(i)) ...
                      cosd(theta(i))^2-sind(theta(i))^2];

    T_e = [ cosd(theta(i))^2                 sind(theta(i))^2             ...
        cosd(theta(i))*sind(theta(i));...
            sind(theta(i))^2                 cosd(theta(i))^2             ...
                -cosd(theta(i))*sind(theta(i));...
            -2*cosd(theta(i))*sind(theta(i))    ...
                2*cosd(theta(i))*sind(theta(i)) ...
                cosd(theta(i))^2-sind(theta(i))^2];

    Q_ = T_o_inv*Q*T_e;
    A = A + Q_*(z(i+1)-z(i));
    B = B + 1/2*Q_*(z(i+1)^2-z(i)^2);
    D = D + 1/3*Q_*(z(i+1)^3-z(i)^3);
end

ABD = [ A B ; B D ];
a = inv(A);
d = inv
E_x = 1/(a(1,1)*h);
E_y = 1/(a(2,2)*h);
G_xy = 1/(a(3,3)*h);
v_xy = -a(2,1)/a(1,1);
v_yx = -a(2,1)/a(2,2);

display(' ')
display(sprintf('Laminate thickness = %0.2f mm',h*1e3))
display(' ')

display('Global Laminate Properties')
disp('-------------------------------------')
display(sprintf('E_x  = %0.2f GPa',E_x/1e9))
display(sprintf('E_y  = %0.2f GPa',E_y/1e9))
display(sprintf('G_xy = %0.2f GPa',G_xy/1e9))
display(sprintf('v_xy = %0.3f',v_xy))
display(sprintf('v_yx = %0.3f',v_yx))
```

A.2 Articulated Boom Optimization

```
clear all, clc, close all

% Properties

l_boom = 1.3;           % [m]
l_box = 0.3;            % [m]
m_box = 3.2;              % [kg]
m_hinge = 0.5;            % [kg]
g_earth = 9.81;         % [m/s^2]
g = 1e-3*g_earth;       % [m/s^2]
n_boom = 1;

% Simplified Circular Boom

% Preliminary Circular Boom properties

d_out = 10e-3;    % [m]
t = 1e-3;      % [m]
d_in = d_out-2*t;    % [m]
I = pi/4*((d_out/2)^4-(d_in/2)^4);  % [m^4]
E = 122.98e9;       % [Pa]
rho = 1578;       % [kg/m^3]
A = pi*((d_out/2)^2-(d_in/2)^2);     % [m^2]
mdot_boom = rho*A; % [kg/m]
m_boom = rho*A*l_boom;  % [kg]

% Deflection for Circular Boom

a = l_boom-l_box;       % [m]
a_hinge1 = l_boom/3;    % [m]
a_hinge2 = 2*l_boom/3;     % [m]
q_box = (m_box*g/n_boom)/l_box; % [N/m] Distributed load by box
q_boom = mdot_boom*g; % [N/m] Distributed load by boom own mass
P_hinge = m_hinge*g;

% Deflection about x-axis
v_max_boom = (q_boom*l_boom^4/(8*E*I))*1e6; % [um]
v_max_box = (q_box/(24*E*I)*(3*l_boom^4-4*a^3*l_boom+a^4))*1e6; % [um]
v_max_hinges = ((P_hinge*a_hinge1^2/(6*E*I)*(3*l_boom-a_hinge1))+...
(P_hinge*a_hinge2^2/(6*E*I)*(3*l_boom-a_hinge2)))*1e6; % [um]
v_max = v_max_boom+v_max_box+v_max_hinges; % [um]

% Determine minimal I for leticular boom

while (v_max>15)
    d_out = d_out+1e-3;
    d_in = d_out-2*t;    % [m]
    I = pi/4*((d_out/2)^4-(d_in/2)^4);  % [m^4]
    A = pi*((d_out/2)^2-(d_in/2)^2);     % [m^2]
    mdot_boom = rho*A; % [kg/m]
    m_boom = rho*A*l_boom;  % [kg]
    m_seg = m_boom/3; % [kg]
    q_boom = mdot_boom*g; % [N/m] Distributed load by boom own mass

    v_max_boom = (q_boom*l_boom^4/(8*E*I))*1e6; % [um]
    v_max_box = (q_box/(24*E*I)*(3*l_boom^4-4*a^3*l_boom+a^4))*1e6; % [um]
    v_max_hinges = ((P_hinge*a_hinge1^2/(6*E*I)*(3*l_boom-a_hinge1))+...
    (P_hinge*a_hinge2^2/(6*E*I)*(3*l_boom-a_hinge2)))*1e6; % [um]
    v_max = v_max_boom+v_max_box+v_max_hinges; % [um]
end
```

```
I
v_max
d_out

% Make circle
r_in = (d_in/2)*100;
r_out = (d_out/2)*100;
c = [0 0];

theta = linspace(0,2*pi,1000);

x_in = c(1) + r_in*sin(theta);
y_in = c(2) + r_in*cos(theta);

x_out = c(1) + r_out*sin(theta);
y_out = c(2) + r_out*cos(theta);

%// draw line
line(x_in,y_in,'Color','k')
line(x_out,y_out,'Color','k')
grid on
ylim([-ceil(r_out) ceil(r_out)])
xlim([-ceil(r_out) ceil(r_out)])
axis equal
xlabel('Width [cm]')
ylabel('Height [cm]')
%// or draw polygon if you want to fill it with color
```

A.3 CTM Boom Optimization

```
clear all, clc, close all

% Properties

l_boom = 1.3;           % [m]
l_box = 0.3;            % [m]
m_box = 3.2;              % [kg]
g_earth = 9.81;         % [m/s^2]
g = 1e-3*g_earth;       % [m/s^2]
rho = 1.6;              % [g/cm^3]
E = 122.98e9;              % [Pa]
n_boom = 1;

% Lenticular Boom Design

% Variables
%r1 = 1.4;   % [cm]
%r2 = r1;    % [cm]
n = 0;
i = 0;
mat_m = [];
mat_v = [];
for r1 = 1:0.1:2;
    n = n+1;
    for x2 = 0.5:0.1:2*r1;
        i = i+1;
        r2 = r1;
        % Boom flange & thickness
        w0 = 0.5;   % [cm]
        t = 0.03;   % [cm]

        % Calculations
        x1 = round(x2/(1+r2/r1),5);     % [cm]
        x3 = x2+w0;                     % [cm]
        X = [-10:0.00001:10];           % [cm]
        e = 1e-6; % error for entry determination
        y01 = -sqrt(r1^2-x1.^2)-sqrt(r2^2-(x1-x2).^2)+r2;    % [cm]
        y02 = r2;                       % [cm]

        % Two parts of the Y array
        y1 = sqrt(r1^2-X.^2)+y01;       % [cm]
        y2 = -sqrt(r2^2-(X-x2).^2)+r2; % [cm]
        y = [];

        % Locate the entry of x1, x2, x3
        loc_x1 = find(X≤x1+e & X≥x1-e);
        loc_x2 = find(X≤x2+e & X≥x2-e);
        loc_x3 = find(X≤x3+e & X≥x3-e);
        n_x3 = loc_x3-loc_x2;

        % Locate the entry of x1, x2, x3 for the left part of the plot
        loc_x1_neg = find(X≤-x1+e & X≥-x1-e);
        loc_x2_neg = find(X≤-x2+e & X≥-x2-e);
        loc_x3_neg = find(X≤-x3+e & X≥-x3-e);
        len_y2_neg = length(y2(loc_x1+1:loc_x2));

        % Make Y matrix
        y = [zeros(1,n_x3) y2(loc_x2:loc_x2+len_y2_neg)...
            y1(loc_x1_neg+1:loc_x1) y2(loc_x1+1:loc_x2) zeros(1,n_x3)];
        X_plot = X(loc_x3_neg:loc_x3);
```

```
    % Plot cross-section
%     line_thick = t/0.035277; % realistic thickness plotted
%     hold on
%     plot(X_plot,y,'k','LineWidth',line_thick)
%     plot(X_plot,-y,'k','LineWidth',line_thick)
%     ylim([-x3 x3])

    % ------- Calculate properties of cross-section ------- %

    % Width of the boom when flattened
    w_flat = 2*(w0+(r1+r2)*acos((r2-y01)/(r1+r2)));     % [cm]
    w_dep = x3*2;                                       % [cm]
    h_dep = (max(y)+t)*2;                               % [cm]

    % Calculate MoI about x-axis
    int_Ixx_1 = @(x) r1*(sqrt(r1^2-x.^2)+y01).^2./sqrt(r1^2-x.^2);
    int_Ixx_2 = @(x) r2*(-sqrt(r2^2-(x-x2).^2)+y02).^2./sqrt(r2^2-(x-x2).^2);
    Ixx = 4*t*(integral(int_Ixx_1,0,x1)+integral(int_Ixx_2,x1,x2));   % ...
        [cm^4]

    % Calculate MoI about y-axis
    beta = 4;
    int_Iyy_1 = @(x) 4*t*r1*x.^2./sqrt(r1^2-x.^2);
    int_Iyy_2 = @(x) 4*t*r2*x.^2./sqrt(r2^2-(x-x2).^2);
    int_Iyy_3 = @(x) beta*t*x.^2;
    Iyy = integral(int_Iyy_1,0,x1)+...
        integral(int_Iyy_2,x1,x2)+integral(int_Iyy_3,x2,x3); % [cm^4]

    % Calculate Torsional stiffness
    int_J_1 = @(x) sqrt(r1^2-x.^2)+y01;
    int_J_2 = @(x) -sqrt(r2^2-(x-x2).^2)+y02;
    int_J_3 = @(x) r1./sqrt(r1^2-x.^2);
    int_J_4 = @(x) r2./sqrt(r2^2-(x-x2).^2);
    J = 16*t*(integral(int_J_1,0,x1)+...
        integral(int_J_2,x1,x2))^2/(integral(int_J_3,0,x1)+...
        integral(int_J_4,x1,x2)); % [cm^4]

    % Calculate mass
    V = 2*w_flat*t*l_boom*1e2;  % [cm^3]
    m_boom = rho*V; % [g]
    mdot_boom = m_boom*1e-3/l_boom; % [kg/m]

    % Calculate distributed loads
    a = l_boom-l_box;   % [m]
    q_box = (m_box*g/n_boom)/l_box; % [N/m] Distributed load by box
    q_boom = mdot_boom*g; % [N/m] Distributed load by boom own mass

    % Calculate max deflection along f-axis
    v_max_boom_xx = (q_boom*l_boom^4/(8*E*Ixx*1e-8))*1e6; % [um]
    v_max_box_xx = ...
        (q_box/(24*E*Ixx*1e-8)*(3*l_boom^4-4*a^3*l_boom+a^4))*1e6; % [um]
    v_max_xx = v_max_boom_xx+v_max_box_xx; % [um]

    % Calculate max deflection along y-axis
    v_max_boom_yy = (q_boom*l_boom^4/(8*E*Iyy*1e-8))*1e6; % [um]
    v_max_box_yy = ...
        (q_box/(24*E*Iyy*1e-8)*(3*l_boom^4-4*a^3*l_boom+a^4))*1e6; % [um]
    v_max_yy = v_max_boom_yy+v_max_box_yy; % [um]

    % Max deflection in matrix
    v_max = [v_max_xx v_max_yy];
```

```
        % Natural frequencies
        K = [3.52 22 61.7 121];
        f_boom_xx = K./(2*pi*l_boom^2)*sqrt(E*Ixx*1e-8/(m_boom*1e-3));
        f_boom_yy = K./(2*pi*l_boom^2)*sqrt(E*Iyy*1e-8/(m_boom*1e-3));
        f = [transpose(f_boom_xx) transpose(f_boom_yy)];
        % Put results in matrix

        mat_m(i,n) = m_boom;
        mat_v(i,n) = max(v_max);
        mat_f(i,n) = min(min(f));
        mat_ixx(i,n) = Ixx;
        mat_iyy(i,n) = Iyy;
        clc
    end
    i = 0;
end
mat_m(imag(mat_m)≠0) = NaN;
mat_v(imag(mat_v)≠0) = NaN;
mat_f(imag(mat_f)≠0) = NaN;
mat_ixx(imag(mat_ixx)≠0) = NaN;
mat_iyy(imag(mat_iyy)≠0) = NaN;
%%
close all, clc

mat_r1 = [1:0.1:2];
mat_x2 = [0.5:0.1:4];
[row col] =  find(mat_v<45 & mat_v>0);
entries = [row col];

mat_final = [];
for k = 1:length(entries)
mat_final(k,1) = mat_v(entries(k,1),entries(k,2));
mat_final(k,2) = mat_m(entries(k,1),entries(k,2));
mat_final(k,3) = mat_f(entries(k,1),entries(k,2));
mat_final(k,4) = mat_ixx(entries(k,1),entries(k,2));
mat_final(k,5) = mat_iyy(entries(k,1),entries(k,2));
mat_final(k,6) = mat_r1(entries(k,02));
mat_final(k,7) = mat_x2(entries(k,1));
mat_final(k,8) = mat_final(k,7)/mat_final(k,6);
mat_final(k,9) = mat_final(k,5)/mat_final(k,4);
mat_final(k,10) = mat_final(k,2)/mat_final(k,1);
end

reduce = find(mat_final(:,9)<2);

result = sortrows(mat_final(reduce,:),1);
mass_rat = result(:,2)./result(:,1);
[min_mass_rat entry_mass_rat] = min(mass_rat);

figure(1)
hold on
grid on
plot(result(:,1),result(:,2),'-o')
xlabel('Deflection [\mum]')
ylabel('Mass [g]')
%title('Deflection vs mass @ 1 mili-g')

best_option = [result(entry_mass_rat,6) result(entry_mass_rat,7)]


%% Final design of boom
clearvars -Except I l_boom g_earth g n_boom t E E rho best_option l_box m_box
```

```
% Variables
m_box = 3.2005;
g = 9.8066e-3;
r1 = best_option(1);
r2 = r1;
x2 = best_option(2);
w0 = 0.5;

% Calculations
x1 = round(x2/(1+r2/r1),5)
x3 = x2+w0
X = [-30:0.00001:30];
e = 1e-6; % error for entry determination
y01 = -sqrt(r1^2-x1.^2)-sqrt(r2^2-(x1-x2).^2)+r2
y02 = r2

% Two parts of the Y array
y1 = sqrt(r1^2-X.^2)+y01;
y2 = -sqrt(r2^2-(X-x2).^2)+r2;
y = [];

% Locate the entry of x1, x2, x3
loc_x1 = find(X≤x1+e & X≥x1-e);
loc_x2 = find(X≤x2+e & X≥x2-e);
loc_x3 = find(X≤x3+e & X≥x3-e);
n_x3 = loc_x3-loc_x2;

% Locate the entry of x1, x2, x3 for the left part of the plot
loc_x1_neg = find(X≤-x1+e & X≥-x1-e);
loc_x2_neg = find(X≤-x2+e & X≥-x2-e);
loc_x3_neg = find(X≤-x3+e & X≥-x3-e);
len_y2_neg = length(y2(loc_x1+1:loc_x2));

% Make Y matrix
y = [zeros(1,n_x3) y2(loc_x2:loc_x2+len_y2_neg) y1(loc_x1_neg+1:loc_x1) ...
    y2(loc_x1+1:loc_x2) zeros(1,n_x3)];
X_plot = X(loc_x3_neg:loc_x3);

% Plot cross-section
line_thick = t/0.035277; % realistic thickness plotted
figure(3)
hold on
grid on
plot(X_plot,y,'k','LineWidth',line_thick)
plot(X_plot,-y,'k','LineWidth',line_thick)
ylim([-x3 x3])
xlabel('Width [cm]')
ylabel('Height [cm]')

% ------- Calculate properties of cross-section ------- %

% Width of the boom when flattened
w_flat = 2*(w0+(r1+r2)*acos((r2-y01)/(r1+r2)))
w_dep = x3*2
h_dep = (max(y)+t)*2

% Calculate MoI about x-axis
int_Ixx_1 = @(x) r1*(sqrt(r1^2-x.^2)+y01).^2./sqrt(r1^2-x.^2);
int_Ixx_2 = @(x) r2*(-sqrt(r2^2-(x-x2).^2)+y02).^2./sqrt(r2^2-(x-x2).^2);
Ixx = 4*t*(integral(int_Ixx_1,0,x1)+integral(int_Ixx_2,x1,x2))

% Calculate MoI about y-axis
beta = 4;
```

```
int_Iyy_1 = @(x) 4*t*r1*x.^2./sqrt(r1^2-x.^2);
int_Iyy_2 = @(x) 4*t*r2*x.^2./sqrt(r2^2-(x-x2).^2);
int_Iyy_3 = @(x) beta*t*x.^2;
Iyy = ...
    integral(int_Iyy_1,0,x1)+integral(int_Iyy_2,x1,x2)+integral(int_Iyy_3,x2,x3)


% Calculate Torsional stiffness
int_J_1 = @(x) sqrt(r1^2-x.^2)+y01;
int_J_2 = @(x) -sqrt(r2^2-(x-x2).^2)+y02;
int_J_3 = @(x) r1./sqrt(r1^2-x.^2);
int_J_4 = @(x) r2./sqrt(r2^2-(x-x2).^2);
J = 16*t*(integral(int_J_1,0,x1)+integral(int_J_2,x1,x2))^2...
/(integral(int_J_3,0,x1)+integral(int_J_4,x1,x2))

% Calculate mass
V = 2*w_flat*t*l_boom*1e2;  % [cm^3]
m_boom = rho*V; % [g]
mdot_boom = m_boom*1e-3/l_boom; % [kg/m]

% Calculate distributed loads
a = l_boom-l_box;   % [m]
q_box = (m_box*g/n_boom)/l_box; % [N/m] Distributed load by box
q_boom = mdot_boom*g; % [N/m] Distributed load by boom own mass

% Calculate max deflection along x-axis
v_max_boom_xx = (q_boom*l_boom^4/(8*E*Ixx*1e-8))*1e6; % [um]
v_max_box_xx = (q_box/(24*E*Ixx*1e-8)*(3*l_boom^4-4*a^3*l_boom+a^4))*1e6; % [um]
v_max_xx = v_max_boom_xx+v_max_box_xx; % [um]

% Calculate max deflection along y-axis
v_max_boom_yy = (q_boom*l_boom^4/(8*E*Iyy*1e-8))*1e6; % [um]
v_max_box_yy = (q_box/(24*E*Iyy*1e-8)*(3*l_boom^4-4*a^3*l_boom+a^4))*1e6; % [um]
v_max_yy = v_max_boom_yy+v_max_box_yy; % [um]

% Max deflection in matrix
v_max = [v_max_xx v_max_yy]

% Natural frequencies
K = [3.52 22 61.7 121];
f_boom_xx = K./(2*pi*l_boom^2)*sqrt(E*Ixx*1e-8/(m_boom*1e-3));
f_boom_yy = K./(2*pi*l_boom^2)*sqrt(E*Iyy*1e-8/(m_boom*1e-3));
f = [transpose(f_boom_xx); transpose(f_boom_yy)];
f = sortrows(f,1);
f = f(1:6);
f_mass_xx = 1/(2*pi)*sqrt(3*E*Ixx*1e-8/(m_box*l_boom^3));
f_mass_yy = 1/(2*pi)*sqrt(3*E*Iyy*1e-8/(m_box*l_boom^3));
```

A.4 Thermal Environment

```
% Thermal Analysis of Boom (J.W. Lopes Barreto)

close all, clc, clear

disp('Thermal Analysis of Box-like Satellite  (J.W. Lopes Barreto)')
disp('-----------------------------------------------------------------')
disp(' ')

% Constants

h = input('Input orbit altitude in [km]: ')*1e3;           % [m] Orbital height
sc = 1367;           % [W/m^2] Solar constant
rho = 0.3;
q_pla = 236;         % [W/m^2] Planetary flux
r_e = 6378.14e3;     % [m] Earth radius
a_e = 0.3;           % [-] Albedo Earth
mu = 3.986004418e14; % [m^3/s^2] Standard gravitational parameter

% Defining position of the Earth and Solar Flux at Earth

v = 1.494*pi; % [rad] True anomaly, CHANGE THIS FOR POSITION EARTH
e_e = 0.0167;
au = 149597870700;                      % [m] 1 AU
r_es = (au*(1-e_e^2))./(1+e_e*cos(v));  % [m] Distance Earth-Sun
q_sol_e = sc/(r_es/au)^2;               % [W/m^2] Solar Flux at Earth
q_sol = sc/((r_es-(h+r_e))/au)^2;       % [W/m^2] Solar Flux at Satellite
FF_ll = r_e/(r_e+h);                       % [-] Form Factor (parallel)
FF_T = (1/(2*pi))*(pi-2*asin(...
    sqrt(1-(r_e/(r_e+h))^2))-...
    sin(2*asin(sqrt(1-(r_e/(r_e+h))^2)))); % [-] Form Factor (perpendicular)
T = 2*pi*sqrt((r_e+h)^3/mu);            % [s] Orbital period

% Beta angle (Simplified as this changes per day)

L = 0;              % [rad] Ecliptic True Solar Longitude
o = deg2rad(23.45); % [rad] Obliquity of the Ecliptic
i = deg2rad(90);    % [rad] Inclination (polar orbit)
w = deg2rad(0);    % [rad] Right Ascension of the Ascending Node


b = input('Input Beta angle in [deg]: ');
B = deg2rad(b);

% Shadow calculation

theta_s = asin(sqrt(1/cos(B)^2*(FF_ll^2-sin(B)^2))); % [rad] Shadow angle
theta_s_deg = rad2deg(theta_s);

% Define angles + eclipse angles

theta = [0:0.01:2*pi];
theta_deg = rad2deg(theta);
I = find(theta_deg < 180+theta_s_deg & theta_deg > 180-theta_s_deg); % ...
    eclipse angles
ep = acos(cos(theta).*cos(B)); % [rad] Solar Zenith Angle between -90 +90

% Calculate orbit time per angle

dt = T/length(theta);
t = [0:dt:T];
```

```
% Perform calculations for the sides
% Side 1 - faces away from the planet (zenith-facing)

q_sol_1 = q_sol.*cos(theta).*cos(B);
q_sol_1(q_sol_1<0) = [0];
q_sol_1(I) = [0];
q_pla_1 = zeros(1,length(theta));
q_alb_1 = zeros(1,length(theta));
q_alb_1(q_alb_1<0) = [0];
q_tot_1 = q_sol_1+q_alb_1+q_pla_1;
q_der_1 = [0 diff(q_tot_1)];

% Side 2 - faces the planet (nadir-facing)

q_sol_2 = -q_sol.*cos(theta).*cos(B);
q_sol_2(q_sol_2<0) = [0];
q_sol_2(I) = [0];
q_pla_2 = (q_sol_e*(1-a_e)/4*FF_ll^2)*ones(1,length(theta));
q_alb_2 = q_sol_e*a_e*FF_ll^2.*cos(ep);
q_alb_2(q_alb_2<0) = [0];
q_tot_2 = q_sol_2+q_alb_2+q_pla_2;
q_der_2 = [0 diff(q_tot_2)];

% Side 3 - faces forward (velocity vector-facing)

q_sol_3 = -q_sol.*sin(theta).*cos(B);
q_sol_3(q_sol_3<0) = [0];
q_sol_3(I) = [0];
q_pla_3 = (q_sol_e*(1-a_e)/4*FF_T)*ones(1,length(theta));
q_alb_3 = q_sol_e*a_e*FF_T.*cos(ep);
q_alb_3(q_alb_3<0) = [0];
q_tot_3 = q_sol_3+q_alb_3+q_pla_3;
q_der_3 = [0 diff(q_tot_3)];

% Side 4 - faces aft (anti-velocity vector-facing)

q_sol_4 = q_sol.*sin(theta).*cos(B);
q_sol_4(q_sol_4<0) = [0];
q_sol_4(I) = [0];
q_pla_4 = (q_sol_e*(1-a_e)/4*FF_ll^2)*ones(1,length(theta));
q_alb_4 = q_sol_e*a_e*FF_ll^2.*cos(ep);
q_alb_4(q_alb_4<0) = [0];
q_tot_4 = q_sol_4+q_alb_4+q_pla_4;
q_der_4 = [0 diff(q_tot_4)];

% Side 5 - faces north

q_sol_5 = q_sol*sin(B).*ones(1,length(theta));
q_sol_5(q_sol_5<0) = [0];
q_sol_5(I) = [0];
q_pla_5 = (q_sol_e*(1-a_e)/4*FF_ll^2)*ones(1,length(theta));
q_alb_5 = q_sol_e*a_e*FF_ll^2.*cos(ep);
q_alb_5(q_alb_5<0) = [0];
q_tot_5 = q_sol_5+q_alb_5+q_pla_5;
q_der_5 = [0 diff(q_tot_5)];

% Side 6 - faces south

q_sol_6 = -q_sol*sin(B).*ones(1,length(theta));
q_sol_6(q_sol_6<0) = [0];
q_sol_6(I) = [0];
q_pla_6 = (q_sol_e*(1-a_e)/4*FF_T)*ones(1,length(theta));
```

```
q_alb_6 = q_sol_e*a_e*FF_T.*cos(ep);
q_alb_6(q_alb_6<0) = [0];
q_tot_6 = q_sol_6+q_alb_6+q_pla_6;
q_der_6 = [0 diff(q_tot_6)];

% Ask for user input

display(' ')
display('Consider a box-like spacecraft orbiting Earth:')
display('* Side 1 - faces away from the planet (zenith-facing)')
display('* Side 2 - faces the planet (nadir-facing)')
display('* Side 3 - faces forward (velocity vector-facing)')
display('* Side 4 - faces aft (anti-velocity vector-facing)')
display('* Side 5 - faces north')
display('* Side 6 - faces south')
display(' ')
side = input('Which side do you want to plot?: ');

while (side > 6 || side < 1)
    side = input('Please enter a correct value. Which side do you want to ...
        plot?: ');
end

% Plot

figure(1)
hold on
grid on
grid minor
plot(theta_deg,eval(sprintf('q_sol_%d', side)),'b','LineWidth',1)
plot(theta_deg,eval(sprintf('q_alb_%d', side)),'r','LineWidth',1)
plot(theta_deg,eval(sprintf('q_pla_%d', side)),'g','LineWidth',1)
plot(theta_deg,eval(sprintf('q_tot_%d', side)),'k','LineWidth',1)
xlabel('Orbit angle (\circ)')
ylabel('Incident Heating Flux (W/m^2)')
legend('Solar','Albedo','Planetary','Total')
title(sprintf('Radiation Flux (Side %i), \\beta-angle = %i\\circ',side,b))
axis([0 360 0 inf])

figure(2)
hold on
grid on
grid minor
plot(theta_deg,eval(sprintf('q_der_%d', side)),'k','LineWidth',1)
title(sprintf('Radiation Flux Change (Side %i), \\beta-angle = %i\\circ',side,b))
xlabel('Orbit angle (\circ)')
ylabel('Incident Heating Flux Change (W/m^2/\circ)')
axis([0 360 -inf inf])

disp(' ')
plotagain = input('Would you like to plot another side? (y/n): ','s');

while plotagain == 'y'
    side = input('Which side do you want to plot?: ');

    while side > 6 || side < 1
        disp(' ')
        side = input('Please enter a correct value. Which side do you want to ...
            plot?: ');
    end
    close all
    figure(1)
    hold on
```

```
        grid on
        grid minor
        plot(theta_deg,eval(sprintf('q_sol_%d', side)),'b','LineWidth',1)
        plot(theta_deg,eval(sprintf('q_alb_%d', side)),'r','LineWidth',1)
        plot(theta_deg,eval(sprintf('q_pla_%d', side)),'g','LineWidth',1)
        plot(theta_deg,eval(sprintf('q_tot_%d', side)),'k','LineWidth',1)
        xlabel('Orbit angle (\circ)')
        ylabel('Incident Heating Flux (W/m^2)')
        legend('Solar','Albedo','Planetary','Total')
        title(sprintf('Radiation Flux (Side %i), \\beta-angle = %i\\circ',side,b))
        axis([0 360 0 inf])

        figure(2)
        hold on
        grid on
        grid minor
        plot(theta_deg,eval(sprintf('q_der_%d', side)),'k','LineWidth',1)
        title(sprintf('Radiation Flux Change (Side %i), \\beta-angle = ...
            %i\\circ',side,b))
        xlabel('Orbit angle (\circ)')
        ylabel('Incident Heating Flux Change (W/m^2/\circ)')
        axis([0 360 -inf inf])

        disp(' ')
        plotagain = input('Would you like to plot another side? (y/n): ','s');
    end
```